Hierarchical nanostructures for light management in thin-film optoelectronic devices

by

Seyed Milad Mahpeykar

A thesis submitted in partial fulfillment of the requirements for the degree of

Doctor of Philosophy

in

Microsystems and Nanodevices

Department of Electrical and Computer Engineering
University of Alberta

Abstract

Despite offering advantages such as physical flexibility and cost-effectiveness, thin-film optoelectronic devices are held back by their lackluster efficiency in competition with their traditional counterparts. Since one major factor in low performance of these devices is known to be their deficiency in light absorption or extraction which is the result of their thin-film materials' properties, seeking for better light management is an intuitive approach to boost their performance. This thesis is focused on leveraging nanotechnology to develop simple and low-cost solutions for addressing light management deficiencies in thin-film photovoltaic devices and light emitting diodes using hierarchical nanostructures by taking advantage of theory, simulation and experimental design, fabrication and characterization.

First, the application of nanostructured indium-doped tin oxide (ITO) electrodes as diffraction gratings for light absorption enhancement in thin-film solar cells is studied using finite-difference time-domain (FDTD) simulation. Resonant coupling of the incident diffracted light with supported waveguide modes in light absorbing layer is shown to provide superior light trapping for nanostructured devices as compared to a planar structure. Among various technologically feasible nanostructures, a two-dimensional nano-branch array is demonstrated as the most promising structure and proven to be able to maintain its performance despite structural imperfections common in fabrication.

Additionally, a stretchable hexagonal diffraction grating, which has the potential to act as an optical diffuser, is proposed. Leveraging the simplicity of self-assembly, the photon manipulation capability of polystyrene nanospheres, and elastomeric properties of polydimethylsiloxane (PDMS), the proposed device is capable of in-situ tuning of both diffraction efficiency and spectral range and displays highly efficient and broadband light diffusion independent of incident light polarization and angle of incidence which enables integration of cheap and widely used materials with simple cost-effective fabrication for light management in optoelectronic devices.

Furthermore, I will leverage a modeling approach for optoelectronic engineering of colloidal quantum-dot (CQD) thin-film solar cells. The presence of a strong efficiency loss mechanism, called the “efficiency black hole”, that can hold back the improvements achieved by any efficiency enhancement strategy is demonstrated. The results suggest that for CQD solar cells to come out of the mentioned black hole, incorporation of an effective light trapping strategy and a high quality CQD film at the same time is an essential necessity. Using the developed optoelectronic model, the requirements for this incorporation approach and the expected efficiencies after its implementation are predicted as a roadmap for solar cell community.

Ultimately, a novel volumetric optical diffuser based on cellulose nano-crystals (CNCs) embedded in PDMS is reported. By offering a very simple and low-cost fabrication process as well as compatibility with large-scale production using an earth-abundant material, the proposed optical diffuser is an ideal choice for integration into optoelectronic devices due to the lack of requirement for an index-matching layer. It is demonstrated that CNCs can provide broadband and highly efficient light diffusion at very low concentrations while maintaining a high degree of transparency. Finally, light management capabilities of CNP hybrid optical diffusers are leveraged to show their potential for light absorption enhancement in thin-film solar cells and light extraction improvement in thin-film LEDs.

Preface

This thesis is an original work by Seyed Milad Mahpeykar. Some of the research conducted for this thesis forms part of a research collaboration, led by Professor Edward H. Sargent at the University of Toronto, with Dr. Xihua Wang being the lead collaborator at the University of Alberta.

Chapter 2 of this thesis has been published as S. M. Mahpeykar, Q. Xiong and X. Wang, "Resonance-induced Absorption Enhancement in Colloidal Quantum Dot Solar Cells Using Nanostructured Electrodes," *Optics Express* 22, A1576-A1588, 2014. I was responsible for performing simulations, data analysis and drafting the manuscript. Q. Xiong assisted in simulations and X. Wang was the supervisory author and was involved in the design of the study and manuscript editing.

Chapter 3 of this thesis has been published as S. M. Mahpeykar, Q. Xiong, J. Wei, L. Meng, B. K. Russell, P. Hermansen, A. V. Singhal and X. Wang, "Stretchable Hexagonal Diffraction Gratings as Optical Diffusers for In Situ Tunable Broadband Photon Management," *Advanced Optical Materials* 4(7), 1106, 2016. X. Wang and I designed the study. I conducted the PDMS substrate fabrication, the measurement experiments, and FDTD simulations. Q. Xiong and J. Wei performed the nanosphere self-assembly. Q. Xiong and I executed the diffraction pattern projections. L. Meng and I carried out the CQD synthesis. B. K. Russell and I designed the stretch mechanism fixture and fabricated CQD film samples. P. Hermansen and A.V. Singhal assisted in nanosphere self-assembly process optimization. X. Wang and I analyzed the data and prepared the manuscript.

Chapter 4 of this thesis has been published as S. M. Mahpeykar and X. Wang, "Optoelectronic engineering of colloidal quantum-dot solar cells beyond the efficiency black hole: a modeling approach," *Proc. of SPIE* Vol. 10099, 1009910-1, 2017. I was in charge of designing the study and

performing optoelectronic modeling and simulations as well as manuscript preparation. X. Wang was the supervisory author and assisted in editing the manuscript.

Chapter 5 of this thesis is published as S. M. Mahpeykar, Y. Zhao, X. Li., Z. Yang, Q. Xu, Z. Lu, E. H. Sargent and X. Wang "Cellulose nanocrystal:polymer hybrid optical diffusers for index-matching-free light management in optoelectronic devices," *Advanced Optical Materials* 1700430, 2017. I was responsible for the design of the study, fabrication and characterization of diffuser samples, and manuscript preparation. Q. Xu assisted in characterization of CNCs. X. Li, Y. Zhao, Z. Yang and Z. Lu collaborated in fabrication and characterization of LED devices. E. H. Sargent and X. Wang were the supervisory authors and assisted in study design and manuscript editing.

Dedicated to my family for always believing in me and pushing me to pursue my dreams

Acknowledgements

I would like to start by expressing my greatest appreciation to my supervisor Dr. Xihua Wang who has not only been a caring mentor but also a great friend since the first day of my studies. None of the works presented in this thesis would have been possible without his great deal of help, encouragements and extensive knowledge. Four years ago, he trusted me with my knowledge and capabilities and I hope that I have been able to pay back for a very small part of what he has done for me to date and I could not have asked for more. I am greatly thankful for the opportunities that he provided me to pursue my ambition and dreams and am sure that my time as a doctorate student would have been very difficult if I was deprived of his great care, kindness and impacts on my personal development which go far beyond just the grad school life.

I would also like to thank the members of my supervisory committee, Dr. Sandipan Pramanik and Dr. Ray DeCorby, whom their constructive comments and thoughtful remarks during the course of my program helped me to polish my research. Additionally, I have been fortunate to develop great friendship with kind and knowledgeable labmates Qiuyang Xiong, Lingju Meng, Shicheng Fan, Dr. Jue Wei, Peter Hermansen, Akshay Singhal, Brandon Russell, Farsad Imtiaz Chowdhury and Qiwei Xu who contributed to my research in many ways and made my school life more fun and enjoyable. I also owe special gratitude to Dr. Sjoerd Hoogland, Dr. Zhenyu Yang, Dr. Xiyan Li, Mengxia Liu, and Dr. Yongbiao Zhao from University of Toronto for their contributions and valuable advice.

It is an undeniable fact that carrying out cutting-edge research and pushing the envelope is impossible without having access to state-of-the-art equipment and years of valuable experience. I have been blessed to have the opportunity to perform my research at the University of Alberta nanoFAB and benefit from the extremely precious knowledge and experience of its staff including Dr. Eric Flaim, Keith Franklin, Michael Hume, Dr. Aaron Hryciw, Peng Li, Stephanie Bozic, Bob Brebber, Glenn Elaschuk, Melissa Hawrelechko, Scott Munro and Les Schowalter. I would also

like to thank Mike Xia of the National Institute for Nanotechnology for providing access and technical support for spectrophotometry.

None of the accomplishments of life would have had any meaning to me without the never-ending love and support from my family. My acknowledgement here does not do justice to my parents, Abbas and Zahra, who have always been an inspiration to me and never stopped believing in me. Even though we were thousands of miles away, their love and encouragement always lifted my spirit whenever I felt down. Special kudos to my brother, Mehrdad, my sister-in-law, Samira, and my lovely nephew, Arsham whom their kindness and support made studying abroad much easier.

The work presented in this thesis was financially supported by the Natural Sciences and Engineering Research Council of Canada (NSERC) Discovery Grant, the Canadian School of Energy and Environment (SEE) PoC Grant, the IC-IMPACTS Centres of Excellence and the University of Alberta Start-up Fund. I would like to thank Canadian Microelectronics Corporation (CMC Microsystems) for the provision of CAD products and services through Canada's National Design Network and their Micro-Nano-Technology Financial Assistance Award which significantly helped in advancing my research. I would also like to acknowledge Alberta Innovates-Technology Futures (AITF) for their support of my studies through the AITF Graduate Student Scholarship.

Table of contents

1 Introduction 1

1.1. Thin-film optoelectronic devices 1

1.1.1. Photovoltaic devices 2

1.1.2. Light emitting diodes 8

1.2. The need for light management in thin-film optoelectronic devices 12

1.3. Light management strategies in thin-film optoelectronic devices 16

1.3.1. Photovoltaic devices 16

1.3.2. Light emitting devices 23

1.4. Thesis objective 29

1.5. Thesis outline 30

2 Resonance-induced absorption enhancement in colloidal quantum dot solar cells using nanostructured electrodes 33

2.1. Background 33

2.2. FDTD simulation: A modeling approach 37

2.3. Light trapping by one-dimensional nanostructured ITO diffraction gratings 40

2.4. Polarization-independent two-dimensional nanostructured ITO diffraction gratings .. 46

2.5. Effect of fabrication flaws on performance of two-dimensional ITO nano-branch diffraction gratings 49

2.6. Conclusions 50

3 Stretchable hexagonal diffraction gratings as optical diffusers for in-situ tunable broadband photon management 52

3.1. Introduction 52

3.2. Experimental and modeling details 54

3.2.1. Optical diffuser fabrication 54

3.2.2. FDTD simulations 55

3.2.3. Diffraction efficiency measurement 56

3.2.4. Diffraction pattern projections 56

3.2.5. CQD film synthesis and absorption measurement 56

3.3. The proposed device structure and properties 57

3.4. Tunable diffraction efficiency 59

3.5. Diffraction Pattern Analysis 65
3.5.1. Experimental analysis 65
3.5.2. Theoretical analysis 69
3.6. Photon Management for Absorption Enhancement in Colloidal Quantum Dot (CQD) Thin-films 72
3.7. Conclusion 75

4 Optoelectronic engineering of colloidal quantum-dot solar cells beyond the efficiency black hole: a modeling approach ***77***
4.1. Introduction 77
4.2. Modeling and simulation methods 79
4.2.1. Device structure 79
4.2.2. Optoelectronic modeling and simulation 80
4.3. Simulation results and performance analysis 82
4.3.1. Optical simulation results 82
4.3.2. Electrical simulation results 84
4.4. Efficiency black hole 85
4.4.1. The origin 85
4.4.2. Performance projections beyond the efficiency black hole 87
4.5. Conclusions 90

5 Cellulose nanocrystal:polymer hybrid optical diffusers for index-matching-free light management in optoelectronic devices ***92***
5.1. Introduction 92
5.2. Experimental details 94
5.2.1. Cellulose nano-crystal synthesis 94
5.2.2. CNP hybrid optical diffuser fabrication 95
5.2.3. Characterization 95
5.3. Optical diffusion, transmission and haze analysis 97
5.4. Index-matching-free light management in optoelectronic devices 103
5.5. Conclusions 109

6 Conclusion ***110***
6.1. Summary of accomplishments and contributions 110
6.2. Future outlook 112

6.2.1. ITO nano-branch electrodes for organic solar cells 112

6.2.2. Tuning the structure of PS/PDMS hexagonal diffraction gratings for better tailored light management 113

6.2.3. Stretchable hexagonal diffraction grating for efficiency enhancement in vertical multi-junction solar cells 113

6.2.4. Improving the quality of quantum dot thin-films 114

6.2.5. Application of CNP hybrid optical diffuser for other types of thin-film LEDs 115

References 116

Appendix A: Finite-difference time-domain (FDTD) basic theory 131

Appendix B: Summary of input data for simulations 134

List of Tables

Table 4-1: Materials parameters used for a typical optoelectronic simulation of a depleted heterojunction CQD solar cell. Superscripts indicate the references from which the parameter values are taken 82

Table 4-2: Summary of the effects of light management on performance merits of a typical CQD solar cell with 300nm CQD film thickness and 100nm diffusion length..... 85

List of figures

Figure 1-1: The band diagram of a p-n junction and its charge distribution regions 3

Figure 1-2: The structure of a basic photovoltaic device 5

Figure 1-3: Current-voltage characteristics of a typical solar cell..... 6

Figure 1-4: Absorbance spectra of PbS colloidal quantum dots for different diameter sizes from 3 to 10 nm. 8

Figure 1-5: A typical thin-film LED structure with a monolayer of quantum dots as the emissive layer. 9

Figure 1-6: Working principle of a typical thin-film LED with a monolayer of quantum dots as the emissive layer. 10

Figure 1-7: Light absorption/charge extraction trade-off in thin-film photovoltaic devices. 14

Figure 1-8: Light management in thin-film photovoltaic devices through light path length increment inside the active layer (red) by (a) back reflector (b) textured back reflector (c) textured front electrode 14

Figure 1-9: Schematic of the structure of a thin-film organic LED (OLED) and light propagation inside its layers after emission. 15

Figure 1-10: Absorption enhancement caused by the excitation of supported optical modes in a thin-film solar cell. 18

Figure 1-11: Light management architectures used in thin-film solar cells by accommodating nanostructures at front (a), middle (b), or back (c) of the device. 18

Figure 1-12: Demonstration of the leaky optical modes supported by basic high refractive index nanostructures 20

Figure 1-13: Light management techniques recently developed for CQD solar cells..... 23

Figure 1-14: Extraction of waveguided modes in thin-film LEDs by using substrate modification techniques 25

Figure 1-15: Extraction of waveguided modes in thin-film LEDs by using scattering media ... 25

Figure 1-16: Extraction of waveguided modes in thin-film LEDs by using (a) photonic crystals (b) surface plasmons 27

Figure 2-1: Structure of a depleted heterojunction CQD solar cell (left) and its energy band diagram (right) 35

Figure 2-2: Schematic diagram of a basic diffraction grating structure and transmitted and reflected orders caused by normal light incidence on grating interface..... 36

Figure 2-3: Schematic diagram of a PbS colloidal quantum dot solar cell with nanostructured ITO diffraction gratings used for simulation *37*

Figure 2-4: (a) Reflection and (b) Transmission diffraction efficiency of triangular ITO gratings as a function of wavelength for TE (left) and TM (right) light polarizations *41*

Figure 2-5: Relative transmission efficiency as a function of direction of diffracted orders for triangular ITO gratings at select (a) on-resonance (947 nm) and (b) off-resonance (1150 nm) wavelengths for TE polarization of light. *42*

Figure 2-6: Light absorption profile for (a,b) triangular (c,d) nano-pillar (e,f) nano-well (g,h) nano-branch ITO gratings at select on-resonance (a,c,e,g) and off-resonance (b,d,f,h) wavelengths for TE polarization of light *44*

Figure 2-7: Simulated absorption spectra of CQD solar cells with different 1D ITO diffraction gratings for (a) TE and (b) TM light polarizations. *45*

Figure 2-8: Simulated absorption spectra of CQD solar cells with 2D pyramid and nano-branch ITO diffraction gratings for TE and TM light polarizations *47*

Figure 2-9: Top-view light absorption profile for 2D nano-branch ITO gratings at select resonance wavelengths for TE (a-d) and TM (e-h) polarizations of light *49*

Figure 2-10: Simulated absorption spectra of CQD solar cells with perfect and imperfect 2D nano-branch ITO diffraction gratings *50*

Figure 3-1: Tunable optical diffuser structure and properties *58*

Figure 3-2: Cross-sectional SEM image of a sample fabricated optical diffuser under (a) unstretched and (b) stretched condition *59*

Figure 3-3: Specular and total transmission of the optical diffuser *61*

Figure 3-4: Specular transmission spectra of a bare PDMS substrate for different levels of stretch *62*

Figure 3-5: Experimentally measured specular transmission from a PS nanosphere-coated glass substrate *63*

Figure 3-6: The dependence of the optical diffuser's performance on incident light polarization and angle *64*

Figure 3-7: Specular transmission measured from a fabricated optical diffuser at various levels of stretch after certain numbers of stretch repetition *65*

Figure 3-8: Diffraction pattern analysis of the optical diffuser. (a) Schematic of the experimental setup utilized for diffraction pattern analysis *67*

Figure 3-9: Simulated diffraction pattern intensities from the unstretched optical diffuser at the light wavelength of 633 nm *68*

Figure 3-10: Generalization of the analysis of the structure of a hexagonal grating *70*

Figure 3-11: Analytical projection of the diffraction pattern of a hexagonal grating 71

Figure 3-12: Absorption enhancement in CQD films using optical diffuser 73

Figure 3-13: Absorption spectra of a 500 μm thick Silicon slab with and without an optical diffuser 75

Figure 4-1: Schematic of the device structure used for optoelectronic simulation of PbS CQD solar cells 79

Figure 4-2: The measured absorption coefficient of PbS colloidal quantum dots used for optoelectronic modeling and simulation 81

Figure 4-3: Sample output from a transfer matrix optical simulation for a typical PbS CQD solar cell 83

Figure 4-4: Simulation of the performance of a depleted heterojunction CQD solar cell under the influence of light management 85

Figure 4-5: Numerical study of electrical performance of a depleted heterojunction CQD solar cell under the influence of light management 87

Figure 4-6: Simulated optoelectronic performance projections for a PbS CQD solar cell at various levels of optical, structural and electrical enhancement 89

Figure 5-1: (a) Photograph of CNP hybrid optical diffusers with different CNC concentrations (from left to right: 0.5, 1, 2, and 4 wt.%). The change in transparency and light diffusion behavior of the samples with an increase in CNC concentration is obvious from the picture. (The scale bar is 1 cm) (b) Physical durability of the diffusers allows application of stretch, twisting and bending without any effect on their optical properties. 99

Figure 5-2: Transmittance and haze of CNP hybrid optical diffusers with different concentrations (wt.%) of CNC as a function of wavelength 100

Figure 5-3: Optical diffusion of a 635 nm laser beam by CNP hybrid optical diffusers with different concentrations (wt.%) of CNC and comparison with a market diffuser 101

Figure 5-4: Angular intensity distribution of a 635 nm laser beam after passing through a CNP hybrid optical diffuser with different concentrations (wt.%) of CNC 102

Figure 5-5: Dependency of specular transmission of CNP hybrid optical diffusers on the incident light angle for different concentrations of CNC 102

Figure 5-6: Transmittance and haze of 1 wt.% CNP hybrid optical diffusers with different thicknesses as a function of wavelength 103

Figure 5-7: Demonstration of the potential application of CNP hybrid optical diffusers for light management in silicon solar cells 105

Figure 5-8: Light extraction enhancement in OLEDs using CNP hybrid optical diffusers. (a) Schematic of the OLED structure with attached CNP hybrid optical diffuser 107

Figure 5-9: (a) Power efficiency and (b) External quantum efficiency of the OLED device without diffuser and with diffusers having different concentrations of CNC 109

Figure 6-1: The schematic of a vertical multi-junction solar cell 114

1

Introduction

1.1. Thin-film optoelectronic devices

Optoelectronic devices have become an indisputable part of modern life when it comes to applications such as lighting, sensing, and energy harvesting. Generally, optoelectronic devices can be divided into two comprehensive categories based on their way of interaction with light. The first category involves light harvesting devices including photovoltaic devices (solar cells) and photodetectors which take advantage of the photoelectric effect [1] as an optical-to-electrical transducer for energy production or sensing applications. Both photovoltaic and photodetector devices operate based on the emission of charge carriers when illuminated with light with the only difference being that photodetectors require a bias or input power for operation while photovoltaic devices do not need a bias to generate electricity. The second category, which can be considered as an electrical-to-optical transducer, is called light emitting devices and comprises semiconductor lasers and light emitting diodes (LEDs), leveraging stimulated emission [2] and radiative recombination [3] to emit light as a source, respectively. In the case of LEDs, a semiconductor junction is forward biased leading to photon emission from charge carriers

recombination inside the junction. On the other hand, the high intensity narrow band beam of photons from laser diodes is generated by phase-matched emission from the semiconductor junction due to multiple back and forth reflections of previously emitted photons which enables amplified radiative recombination inside the junction.

While traditional optoelectronic devices have been imposing their dominance on the market for a few decades, the motivation to drive down the production cost and boost the market penetration of optoelectronic devices has led to the formation of an emerging technology referred to as thin-film optoelectronics [4]-[7]. Thin-film optoelectronic devices are considered as a more modern sub-division of optoelectronic devices in which the active layer in charge of light absorption or emission is composed of one or more films of usually semiconductor materials which are very thin in thickness (in the order of a few hundreds of nanometers to a few micrometers). Furthermore, the whole device is normally made of a stack of thin layers of different materials. This has led to the application of new low-cost emerging materials in optoelectronics devices including but not limited to organic semiconductors [8]-[12], quantum dots [13]-[17] and perovskites [18]-[22]. In addition to lowering the ultimate fabrication price of optoelectronic devices due to less requirement for high quality semiconductor materials, thin-film technologies have enabled light emitting devices to be fabricated at larger chip sizes (in the order of several millimeters as opposed to several hundreds of microns for traditional devices) with better heat dissipation, thereby providing higher light output from a single chip thanks to the simple architecture provided by thin-film technology. More importantly, the possibility of using thin films of materials in the structure of these devices has provided compatibility with flexible substrates. Light harvesting devices have also benefitted from the cost reduction and physical flexibility potential of thin-films.

1.1.1. Photovoltaic devices

A photovoltaic device, or a solar cell, is defined as a device capable of converting light into electricity. Such device is typically made of light absorbing semiconductors forming a p-n junction. The junction itself can be formed by one material with different doping levels (a homojunction) or the materials on the either side of the junction could be different (a heterojunction). As illustrated in figure 1-1, upon the formation of the junction, due to the establishment of a depletion region free of charge carriers at the junction's interface, a built-in potential will be established, the amount of which is equal to the difference between fermi levels of the materials forming the junction. This built-in potential will in turn lead to formation of an electric field across the depletion region which contributes to separating photo-generated charges.

In devices with high diffusion lengths such as silicon-based, Cadmium Telluride (CdTe) and compound semiconductor solar cells, most of the charge transport is done by diffusion inside regions without any built-in field (quasi-neutral regions), where as in the case of some other technologies (emerging thin-film solar cells, for example), drift driven transport due to the built-in field significantly contributes to charge transport since materials used in these types of devices suffer from low diffusion lengths and high trap states density.

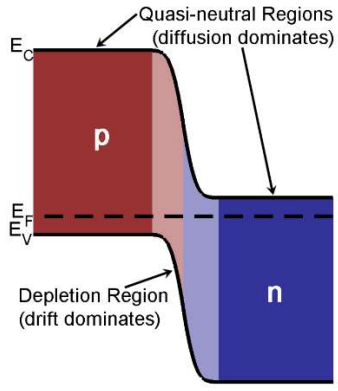

Figure 1-1: The band diagram of a p-n junction and its charge distribution regions. ***Reprinted by permission from Macmillan Publishers Ltd: Nature [23], copyright (2012).***

A solar cell cannot be made of a sole p-n junction. The most basic photovoltaic device requires at least three main components including a light absorbing layer, a charge separator and/or transporter, and electrical contacts. In some cases, a material might play the role for more than one of these components at the same time. For instance, a light absorbing layer, also called active layer, can also act as a charge transport component for electrons or holes or even both. Figure 1-2 depicts the structure of a basic photovoltaic device. The light penetrates through the front contact and is absorbed by the active material. The junction is located inside the active area and photo-generated charge carriers are collected at the contacts. In most cases, the front contact is made of an optically transparent material to facilitate light absorption inside the active material. The back contact is often chosen from an optically reflective material which can recycle photons not absorbed by active material when they pass through the device for the first time.

The amount of light absorbed by the device relies heavily on the bandgap of the light absorbing material. All the photons whose energy is lower than the bandgap will not be absorbed and in the case of photons with energy greater than the bandgap, although at first the generated exciton (electron-hole pair firmly bound together) possesses an energy equal to the energy of the absorbed photon, its energy quickly relaxes to the bandgap of the active material and the extra energy will be wasted. Therefore, a single-junction photovoltaic device cannot utilize all the energy available in the sun's broad spectrum.

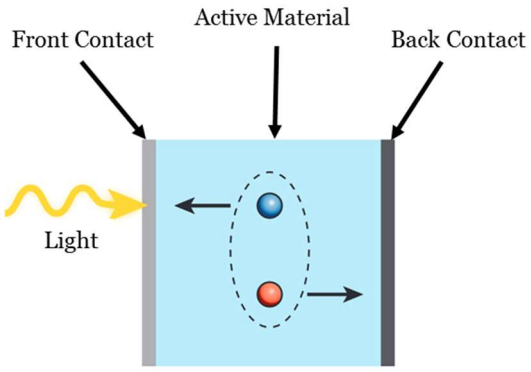

Figure 1-2: The structure of a basic photovoltaic device. ***Reprinted by permission from Macmillan Publishers Ltd: Nature [23], copyright (2012).***

Upon the generation of an exciton, it must be separated into a free electron and a free hole by some mechanism. This is typically accomplished by the existence of band offsets at the junction's interface, the presence of an electric field or thermionic emission. If this charge separation mechanism does not happen quick enough, charge recombination will greatly hurt the output current of the device. After separation, the carriers will be transported to their respective contacts through a combination of drift and diffusion transport mechanisms.

The maximum current a device can deliver under solar illumination can be obtained when the p-n junction is at zero-volt bias. This value, which relies on the number absorbed photons and the efficiency of charge extraction, is called short-circuit current and is usually reported in the form of short-circuit current density or current per device unit area (J_{SC}) to eliminate the variations in device surface area. Upon the application of a bias to the device, majority carriers start to diffuse across the junction. As the bias voltage gets close to the built-in potential of the junction, this bias driven current (alongside the other recombination currents existent in the device layers) is balanced with the photo-generated current. As a result, no net current flow exists across the device. This condition is called the open-circuit condition and the voltage at which it happens is known as the open-circuit voltage (V_{OC}). Any point between the open-circuit and the short-circuit conditions will lie on the J-V curve of the solar cell, as illustrated in figure 1-3. The point at which the device can deliver maximum possible output power is called the maximum power point (MPP) and is considered the optimal operating point for a solar cell. The corresponding current and voltage of this point are shown as J_{MPP} and V_{MPP}, respectively.

One important performance metric for a solar cell is known as the fill factor (FF) and can be considered as a measure of proximity of the J-V curve to a curve from an ideal solar cell. The fill factor can be defined using the following equation:

$$FF = \frac{J_{MPP}V_{MPP}}{J_{SC}V_{OC}} \tag{1-1}$$

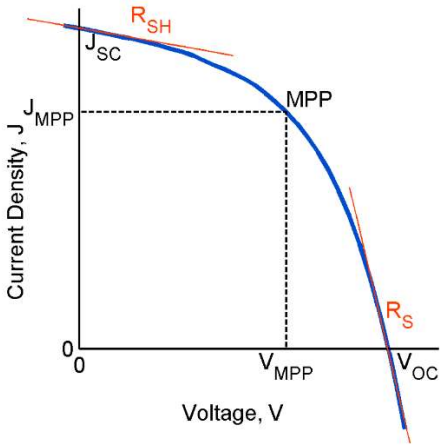

Figure 1-3: Current-voltage characteristics of a typical solar cell. ***Reprinted by permission from Macmillan Publishers Ltd: Nature [23], copyright (2012).***

The ultimate figure of merit for a photovoltaic device is its power conversion efficiency (η) which can depict the percentage of solar power input (P_{in}) that is successfully converted into electrical energy by the device and can be calculated using the following relation:

$$\eta = \frac{J_{MPP}V_{MPP}}{P_{in}} = \frac{FFJ_{SC}V_{OC}}{P_{in}} \tag{1-2}$$

Another performance metric of a solar cell is an evaluation of the device's internal resistance to the generated photocurrent and is called the series resistance (R_S). This resistance usually arises from non-ideal contacts established to the p-n junction or transport barriers present for carriers and can roughly be estimated from the inverse of the slope of the J-V curve close to the open-circuit point as illustrated in figure 1-3. Similarly, the shunt resistance (R_{SH}) which is a measure of the device's resistance to leakage current can be roughly calculated from the inverse of the slope around the short-circuit point. The mentioned leakage current, which may be due to the conducting channels formed between the n- and the p- side as a result of the film's morphology imperfections, can annihilate the carriers before they get a chance to contribute to the output

power generation. Ultimately, for a best performing cell, it is desired to have the minimum series resistance and maximum shunt resistance possible.

While the power conversion efficiency is the ultimate performance metric for a photovoltaic device, it does not provide detailed information about the regions of solar spectrum at which the device is performing well and how those regions contribute to the overall efficiency. For this purpose, another figure of merit known as external quantum efficiency (also called incident photon conversion efficiency or IPCE) is defined as the ratio of the number of extracted electrons to the number of incident photons at each wavelength described as a percentage:

$$EQE(\%) = \frac{Jsc}{P_{in}/h\nu} \times 100 = \frac{Jsc\, hc}{P_{in}\, \lambda} \times 100 \qquad (1\text{-}3)$$

In summary, for the best performance, a photovoltaic device should optimally capture the incident light, convert the incident photons to free charge carriers and extract the generated carriers as useful electrical power. As will be discussed in the following sections, this thesis is focused on the first requirement to optimize light capturing performance of photovoltaic devices, specifically in colloidal quantum dot (CQD) solar cells.

Colloidal quantum dots (CQDs) are semiconducting nanoparticles with diameters ranged at around a few nanometers. One main advantage of CQDs over other traditional semiconductors such as silicon is their facile fabrication through solution processing which eliminates the need for costly fabrication processes under high vacuum. The other significant advantage of CQDs is a phenomenon known as the quantum size effect [24]. As soon as a quantum dot size becomes lower than its Bohr exciton radius (the average distance between an electron-hole pair generated by photon absorption) the material undergoes a quantum confinement which means in contrast with a bulk material, its density of states is not continuous anymore. Thus, by changing the size of the nanoparticle, its electronic bandgap can be tuned. The smaller the quantum dot size is, the greater is the bandgap. Figure 1-4 shows the absorbance spectra for different sizes of PbS CQDs

resulting from different bandgap sizes. Because of the above-mentioned properties, CQDs have found their way to emerging optoelectronic devices including solar cells [25], [26], photodetectors [17], [27], and light emitting diodes [15], [28]. Because of their low-cost fabrication by solution processing which enables commercialization through roll-to-roll fabrication and the compatibility with flexible photovoltaic technologies, CQD materials have attracted great attention for solar cell application.

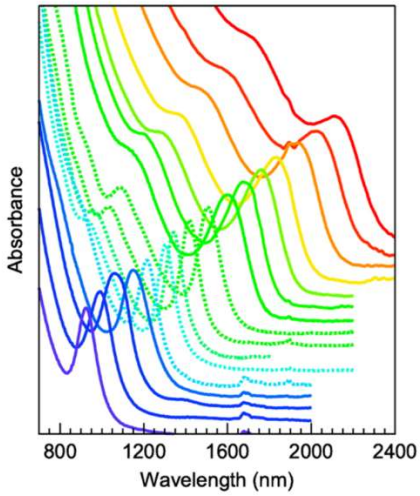

Figure 1-4: Absorbance spectra of PbS colloidal quantum dots for different diameter sizes from 3 to 10 nm. ***Reprinted with permission from [29]. Copyright (2011) American Chemical Society.***

1.1.2. Light emitting diodes

Figure 1-5 illustrates the schematic of the basic structure of a thin-film light emitting diode. The device is usually fabricated on a transparent substrate such as glass which is coated with a transparent anode layer (normally made of indium-doped tin oxide) which supplies positive charge carriers (holes) to the device. On the other side of the device, a usually metallic cathode electrode is in charge of providing negative charge carriers (electrons). As shown in the figure, the structure also includes an electron transport layer and a hole transport layer which as their names suggest are responsible for transporting charges from the electrodes on the either sides of the device to the emissive layer. The emissive layer is made of materials capable of photon emission

upon charge injection which includes organic polymers, semiconductor quantum dots, perovskites and so on. The presented figure illustrates a monolayer of quantum dots (QDs) as the forming material of the emissive layer. After photon emission, the emitted light with get extracted from the transparent anode side of the device.

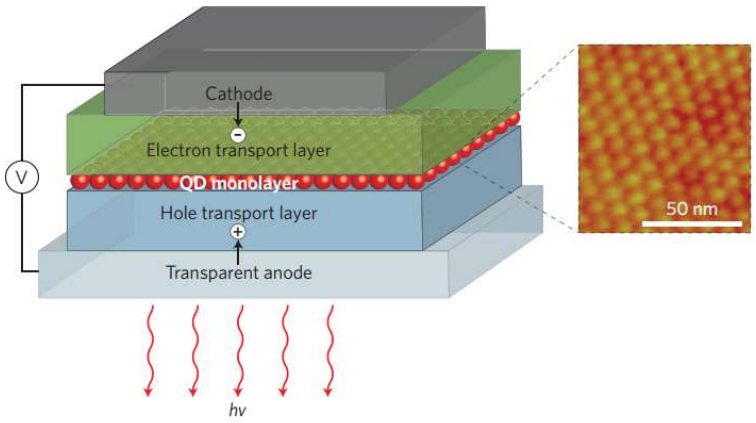

Figure 1-5: A typical thin-film LED structure with a monolayer of quantum dots as the emissive layer. ***Reprinted by permission from Macmillan Publishers Ltd: Nature photonics [15], copyright (2013).***

The working principle of a typical thin-film LED with a monolayer of quantum dots as the emissive layer is depicted in figure 1-6. As is illustrated in the figure, the electrons provided by the cathode electrode will be transferred to the emissive layer (here made of QDs) through the electron transport layer (ETL) and the holes supplied by the anode electrode will be transported to the emissive layer through the hole transport layer (HTL). In order for the photon emission to happen, an electron-hole pair should be recombined inside the emissive layer through a radiative recombination process. The energy band alignments for all layers should be designed such that the electrons could be easily transferred from the cathode to the emissive layer and the holes could be simply transported from the anode to the emissive layer. In addition, the conduction band energy level for the hole transport layer and valence band energy level for the electron transport layer would be such that both the electrons and holes will be most likely trapped inside the emissive layer after reaching it thereby increasing the chance of electron-hole recombination.

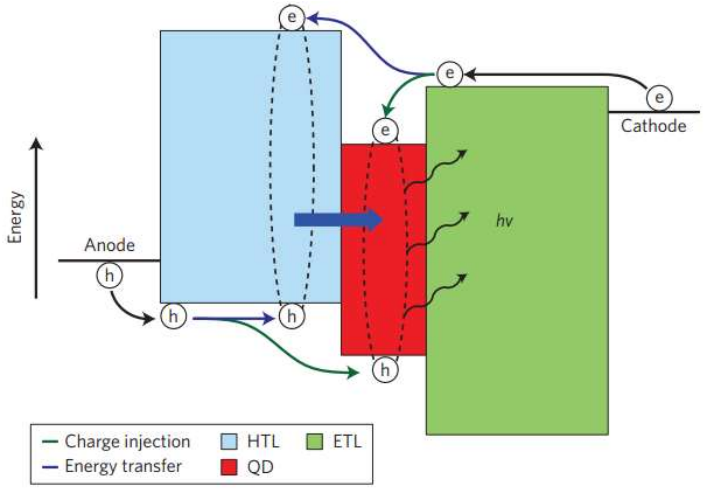

Figure 1-6: Working principle of a typical thin-film LED with a monolayer of quantum dots as the emissive layer. ***Reprinted by permission from Macmillan Publishers Ltd: Nature photonics [15], copyright (2013).***

The most important figure of merit for measurement of the performance of a light emitting diode is its external quantum efficiency (EQE) which is defined in the exact opposite of way its definition for a photovoltaic device. For a light emitting diode. the external quantum efficiency is defined as the ratio of the total number of photons emitted by the device into the viewing direction to the total number of electrons injected into the device. Similarly, the internal quantum efficiency (IQE) of the device is defined as the ratio of the total number of photons emitted by the emissive layer to the total number of electrons injected into the device. The EQE of a light emitting diode is related to its IQE through the following equation:

$$\eta_{ext} = \eta_{int}\eta_{coupling} \tag{1-4}$$

Where η_{ext} is the external quantum efficiency, η_{int} depicts the internal quantum efficiency and $\eta_{coupling}$ represents the light coupling efficiency of the device which is defined as the ratio of the total number of photons emitted by the device in forward direction to the total number of photons emitted by the emissive layer.

The internal quantum efficiency of thin-film LED devices is mainly affected by the non-radiative electron-hole recombination loss which is not highly likely to happen for most of the emissive layer materials. In fact, a variety of thin-film LED devices have been able to achieve IQE values of close to 100% [30]. However, the measured external quantum efficiency from all the thin-film LED devices remains very low which denotes that light coupling efficiency of thin-film LED devices is the major bottleneck for their external quantum efficiency values. It has been argued that by assuming an isotropic emission from the emissive material and a perfectly reflective cathode electrode, the light coupling efficiency of a thin-film LED device can be estimated using the following relation [31]:

$$\eta_{coupling} = \frac{1}{\xi n^2} \tag{1-5}$$

Where n is the refractive index of the emissive material and ξ is a constant that is dependent on the emissive molecules alignment and the geometry of the device. Given the high refractive index values of the emissive materials in most thin-film LEDs (about 2~3), the light coupling efficiency of the thin-film LEDs could be very low.

Based on the definition of external quantum efficiency for LED devices, one can measure the value of EQE for a device using the following equation [31]:

$$\eta_{ext} = \frac{q \int \lambda I_{det}(\lambda) d\lambda}{hcI_{LED} \int R(\lambda) d\lambda} \tag{1-6}$$

Where q is the charge of an electron, λ depicts the wavelength of light at which the measurement is being done, I_{det} represents the photocurrent from the photo-detector used for measurement, h describes the Planck's constant, c is the speed of light, I_{LED} depicts the current drawn by the LED device and R represents the responsivity of the photodetector.

A secondary criterion for evaluating the performance of LED devices is known as the power efficiency which is defined as the ratio of the power of light output from the device to the electrical power consumed by the device. The power efficiency of an LED device can be determined using the following equation:

$$\eta_{power} = \frac{P_{LED}}{I_{LED}V} \tag{1-7}$$

Where P_{LED} is the measured output power by a power detector, I_{LED} depicts the current drawn by the device and V represents the bias voltage.

1.2. The need for light management in thin-film optoelectronic devices

Despite their massive success in realization of cost-effective and flexible optoelectronic devices fabrication, thin-film optoelectronics have not been exploited to their full potential in the market so far. The main reason behind their lackluster existence in the market is believed to be their lower efficiencies when compared to their traditional counterparts. Although a variety of factors such as low quality of emerging thin-film materials for charge carrier transport and extraction have been identified as the reasons behind their unimpressive performance, a major bottleneck for the efficiency of thin-film optoelectronic devices is considered to be their deficiency in light absorption or extraction, especially in the case of thin-film photovoltaic devices and LEDs.

In the case of thin-film solar cells, non-silicon based materials have been of great interest for research in recent years, mainly due to the desire to lower the production cost of solar energy and to make it economically competitive with other energy resources. Extensive efforts for this objective included research and development of organic [32], dye-sensitized [33], perovskite [34] and colloidal quantum dot solar cells [24]. Recent progress in development of thin-film solar cells

has demonstrated that this type of solar cells can be considered as a promising candidate for photovoltaic application.

Despite all the efforts put into the development of thin-film solar cells, the best power conversion efficiencies obtained are still way inferior to that of traditional silicon solar cells. The main reason behind this limitation in efficiency is the existence of a big mismatch between photo-generated carriers diffusion length and light absorption depth for light absorbing layer in this type of solar cells. The direct consequence of this mismatch, as shown in figure 1-7, would be that choosing a large thickness for the active layer (figure 1-7-a) will contribute to absorption of all the incident light to a great extent but at the same time will prevent the photo-generated charges to be extracted efficiently due to their limited diffusion length. On the contrary, a thin active layer would allow efficient charge extraction towards the electrodes (figure 1-7-b) while not being able to absorb all the available light because of its limited thickness. For instance, in the case of quantum dot solar cells, the best solar cells reported so far still have low carrier mobility (~10^{-4}-10^{-3} $cm^2/V.s$) in quantum dot layer [35]. This imposes a limit of 200-300 nm for the thickness of active layer in quantum dot solar cells for optimum carrier collection efficiency which is far away from the optimum thickness for complete light absorption and leaves many of the incident photons uncollected.

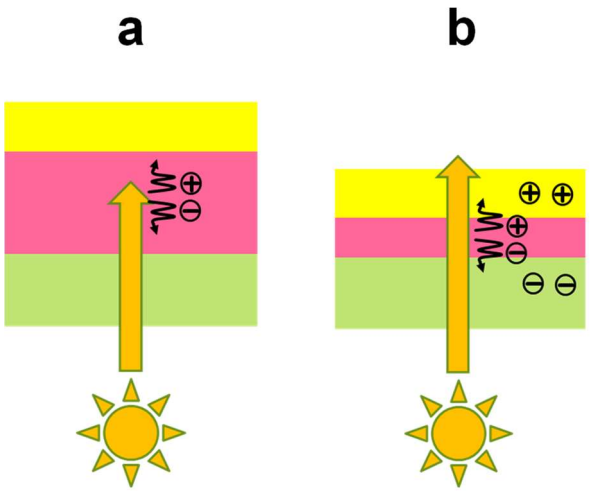

Figure 1-7: Light absorption/charge extraction trade-off in thin-film photovoltaic devices. (a) The large thickness for the active layer (red) will contribute to absorption of all the incident light to a great extent but at the same time will prevent the photo-generated charges to be extracted efficiently due to their limited diffusion length. (b) A thin active layer would allow efficient charge extraction towards the electrodes (green and yellow) while not being able to absorb all the available light because of its limited thickness.

One way to overcome the above-mentioned limitation is to increase the chance of light absorption inside the active layer by increasing the optical path length of incident light inside solar cell without increasing the thickness of the light absorbing layer. This concept, as illustrated in figure 1-8, is usually referred to as light trapping or light management technique for photovoltaic devices [36] and is possible through manipulation of the structure of the device by exploiting engineered materials and structures.

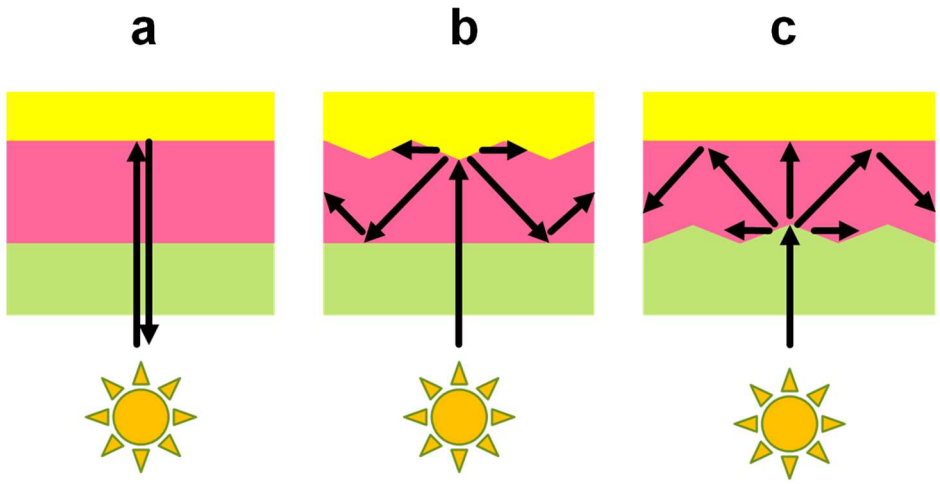

Figure 1-8: Light management in thin-film photovoltaic devices through light path length increment inside the active layer (red) by (a) back reflector (b) textured back reflector (c) textured front electrode

As for thin-film LEDs, the problem of light management applies in the exact opposite way. The basic structure of a thin-film LED is composed of a glass substrate coated with a transparent conductive oxide and a light emitting layer which is sandwiched between two charge transport layers topped by a usually metallic back electrode. As is illustrated in figure 1-9 for an organic LED (OLED) as an example, due to the contrast in refractive indices for different layers that form the

device, total internal reflection can easily occur which in turn will lead to light trapping or undesirable emission from the edge and can cause difficulties in extracting the emitted light from the device's front side [30]. Each layer can have its own contribution to the light trapping and only the portion of light that is emitted within a certain angle with the normal to the device's surface at each interface can escape towards the front of the device. The higher the refractive index contrast between two layers, the smaller the amount of the escape angle will be.

The problem is even more intense in the case of quantum dot and perovskite based LEDs due to the high refractive index (~2-3) of their light emitting material [15], [19]. The remedy for light trapping problem in thin-film LEDs is of course light management through which the escape angle for light extraction can be extended and higher portion of light can be guided toward the front of the device. Just like thin-film photovoltaic devices, light management in thin-film LEDs is feasible by modifications in the structure of the device using specifically engineered materials and structures which will be briefly discussed in the following section.

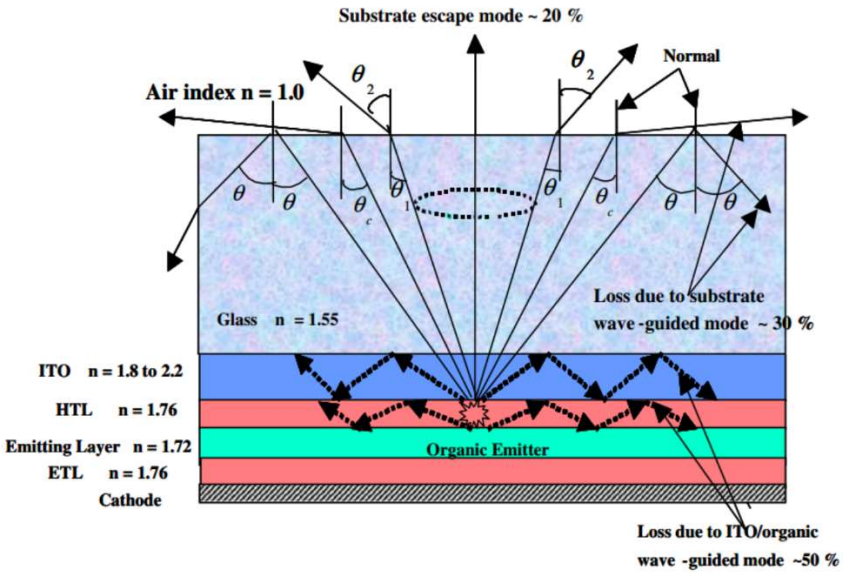

Figure 1-9: Schematic of the structure of a thin-film organic LED (OLED) and light propagation inside its layers after emission. A high portion of the emitted light will be trapped into different guided modes supported by various layers of the device. ***Reprinted from [30], Copyright (2009), with permission from Elsevier.***

The problem of inefficient light absorption/extraction (or light management in general) is of less concern for thin-film photodetectors and lasers mainly due to the fact that the reverse bias applied to photodetectors enables efficient extraction of charge carriers generated by light absorption thereby providing the possibility for the thickness of light absorbing material to be optimized for maximum light absorption. As for thin-film lasers, due to their well-controlled light propagation which is an essential necessity for stimulated emission, further light management will not be the most effective way to improve the efficiency. As such, the efforts in this thesis have been focused on solutions for light management in photovoltaic devices and LEDs.

1.3. Light management strategies in thin-film optoelectronic devices

1.3.1. Photovoltaic devices

To be able to take the best strategy for light management in photovoltaic devices, one must truly understand the optical modes supported by these devices. A solar cell can support a variety of optical modes that can be utilized for enhancing light absorption inside the cell's active material. Figure 1-10-a illustrates the schematic of a sample thin-film solar cell structure with built-in light trapping nanostructures. Four of the most commonly occurring optical modes supported by a nanostructured solar cell are labeled as 1-4 in this figure. Resonant coupling of the incident sunlight with one or a multitude of these modes is believed to be responsible for light absorption enhancement in the light absorbing layer of the cell (semiconductor) [36] and is usually called resonance. Due to the different ways that these resonant modes manipulate the light propagation, each will cause different field distributions inside the cell's structure which can help in identification of these modes. These field distributions are shown in figures 1-10-b through 1-10-e.

The first mode is known as Mie resonance, which describes the scattering of electromagnetic waves by wavelength-scale spherical particles. The waves get scattered due to the electric charges in the particle being oscillated by the electric field of the incident wave. Accelerated charges radiate electromagnetic energy in all directions. This charge excitation and redirection of the energy constitutes scattering. In addition, the excited charges may absorb part of the energy and transform it into other forms. As is clear from the field distributions of this mode (figure 1-10-b), concentration of light inside the spherical particles denotes the existence of Mie resonance. The second mode, which its resulting field distribution is illustrated in figure 1-10-c, is known as Fabry-Perot resonance. This mode stems from the standing waves forming by confinement of light between the reflecting top surface of the semiconductor film and the metallic back-reflector. Periodic changes in field intensity between the semiconductor's top surface and the back-reflector caused by constructive and destructive interferences are a clear sign of the existence of this mode of resonance.

The third mode is referred to as guided mode resonance and it is supported when a periodic structure on top of the light absorbing film acts as a diffraction grating and can induce phase-matched coupling of normally incident plane wave into a waveguide mode supported by the film. Periodic field intensity variations obvious in figure 1-10-d denote the occurrence of this type of resonance. The last type of supported optical mode by a solar cell is called the diffracted mode. Such mode can be excited when the incident light is redirected into the plane of the light-trapping nanostructure where, as shown in figure 1-10-e, most of the field is concentrated. This mode usually can extend into the underlying semiconductor layer where useful absorption can occur. Optimal broadband absorption enhancement can be reached by exciting as many of the above-mentioned modes in each frequency.

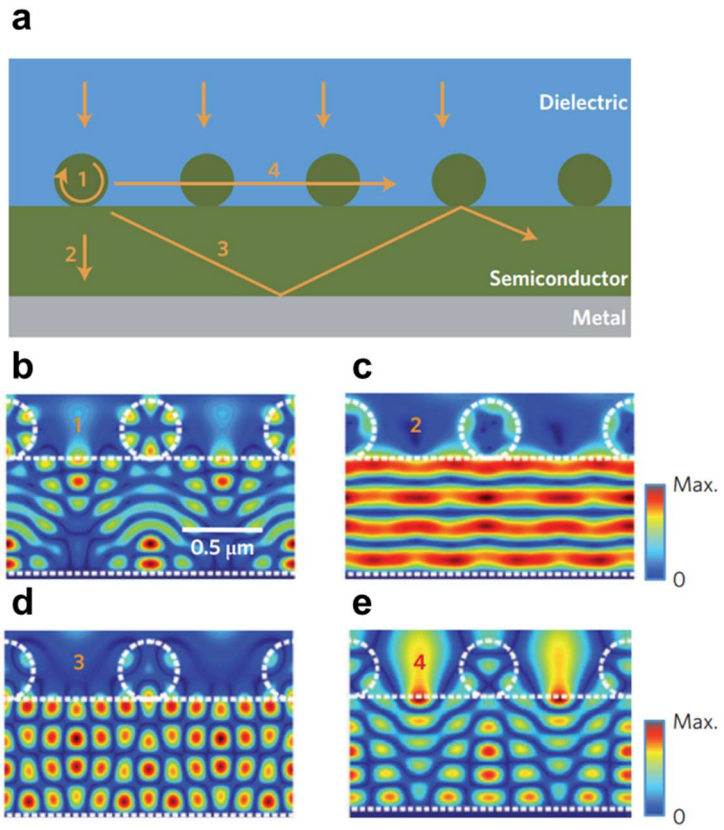

Figure 1-10: Absorption enhancement caused by the excitation of supported optical modes in a thin-film solar cell. (a) Schematic of a model cell structure with definition of supported optical modes (1) Mie (2) Fabry-Perot (3) guided (4) lateral (b-e) Electric field intensity distribution inside the cell for different supported optical modes (b) Mie (c) Fabry-Perot (d) guided (e) lateral. ***Reprinted by permission from Macmillan Publishers Ltd: Nature materials [36], copyright (2014)****.*

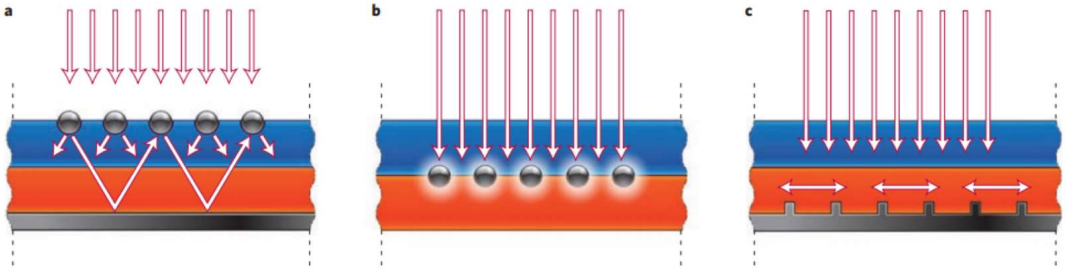

Figure 1-11: Light management architectures used in thin-film solar cells by accommodating nanostructures at front (a), middle (b), or back (c) of the device. ***Reprinted by permission from Macmillan Publishers Ltd: Nature materials [37], copyright (2010)****.*

Nanostructures designed for light management in solar cells can be categorized into three different types in terms of the location inside the cell's structure at which they are accommodated. As is illustrated in figure 1-11, nanostructures can be placed in front of, inside of, or back surface of the solar cells. When the nanostructures are located on the front face (figure 1-11-a), they can increase the effective path-way of light inside the light absorbing layer by coupling the incident light into the semiconductor layer and also they can reduce the reflection from the front surface. If the nanostructures are inside the cell's light absorbing layer (figure 1-11-b), or in other words, the light absorbing layer is nanostructured, both electronic and optical properties of the cell can benefit from it. This is because these nanostructures can be designed such that both light absorption and charge extraction of this layer are improved. This enables the usage of cost-effective materials with shorter carrier diffusion lengths inside the cell's structure. Finally, in case the nanostructures are implemented at the back surface of the cell (figure 1-11-c), they are usually designed such that the performance of the back reflector is increased by redistributing light into guided or diffracted modes without any parasitic absorption of commonly used metallic back reflectors.

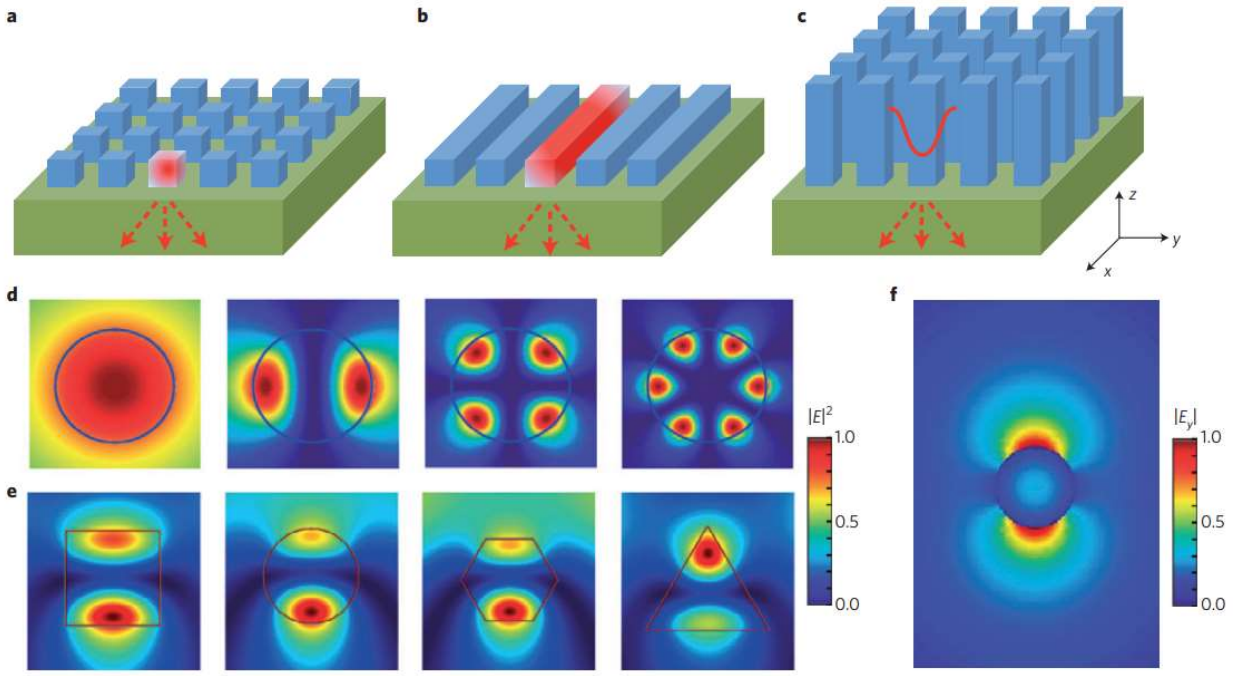

Figure 1-12: Demonstration of the leaky optical modes supported by basic high refractive index nanostructures: (a-c) Basic arrays of nanostructures suitable for light management in thin-film photovoltaic devices (a) zero-dimensional nanoparticle (b) one-dimensional horizontal nanowire (c) one-dimensional vertical nanowire. Under suitable conditions, all these structures can cause light scattering inside the layer underneath. (d) Lowest order transverse magnetic optical modes (m=0,1,2,3 from left to right) supported by a one-dimensional nanowire with circular cross-section. (e) Electric-field distribution for first order (m=1) transverse magnetic optical mode supported by nanowires with different cross-sectional shapes. (f) E-field distribution of fundamental optical mode supported by a sub-wavelength (45 nm radius) for a 547 nm illumination wavelength. ***Reprinted by permission from Macmillan Publishers Ltd: Nature materials [36], copyright (2014).***

For the purpose of light manipulation at nanoscale, dielectric or semiconductor nanostructures with high values of refractive index provide a better opportunity [36]. This is because their high refractive index can lead to stronger interaction with incident light. When having a specific size and shape, they can support the above-mentioned optical modes which can further boost their light management capability. Excitation of these modes can directly enhance light absorption in a solar cell if the nanostructure is an integral part of the cell's active layer. If not, they can indirectly improve the light absorption by excitation of another mode inside the active layer.

Figure 1-12-a-c show the basic types of nanostructures that are suitable for light management in thin-film solar cells. These include nanostructures that zero-dimensional like a nanoparticle (figure 1-12-a) or one-dimensional similar to a nanowire (figure 1-12-b,c). Assuming that the structures are illuminated from the top, in the case of nanoparticles and horizontally oriented nanowires, localized optical resonances can be excited inside the structure itself. As for vertically oriented nanowires, light can couple into the supported waveguide modes from the top. Naturally, these structures can confine light in its propagation direction (normal to the device's surface) and also one lateral direction.

As an example, in the case of one-dimensional nanostructures, assuming a top side illumination, the potentially supported resonances can be purely transverse electric (electric field perpendicular to the axis of one-dimensional structure) or transverse magnetic (electric field parallel to the axis) [36]. Each mode can be assigned an integer number (m) which describes the azimuthal phase

dependence ($e^{im\varphi}$) of the fields. For instance, figure 1-12-d shows the field distribution for lowest order transverse magnetic optical resonances supported by nanowires with circular cross-sections. Light trapping in this case is possible due to multiple total internal reflections happening at the periphery of the structure. This particular optical mode is called a whispering gallery mode. So, in this case, the resonance occurs when an integer (m) of number of wavelengths can be fit around the circumference of the wire.

The aforementioned resonances are a general feature of high refractive index structures and thus their observation is not confined to structures with perfectly circular cross-sections or spherical shapes. As is illustrated in figure 1-12-e, such resonances can be excited in structures with different shapes in cross-section. Even for sub-wavelength structures with dimensions smaller than the incident light's wavelength, as demonstrated in figure 1-12-f, there are fundamental modes that can be excited. Generally, the mentioned modes can be supported by any semiconductor material and transparent oxide with medium to high refractive index. It is even possible to exploit nanoscale cavities in a high refractive index structure for light trapping purposes in photovoltaic devices. The generality of the conditions under which these optical modes can be excited gives a great deal of freedom to the community in terms of the material of choice, shape, size and fabrication methods used for realization of light management in thin-film photovoltaic devices, providing a highly flexible platform for light trapping.

Although they are applicable to almost all the available thin-film solar cell technologies, all the light management efforts pursued in this thesis for photovoltaic devices are focused on colloidal quantum dot (CQD) solar cells which will be discussed in detail in the following sections. As such, a brief review of light management techniques explored recently for CQD solar cells will be presented in the following.

CQDs have strong absorption in visible wavelengths of light due to their high absorption coefficients in this region. However, when it comes to infrared wavelengths near their bandgap energy, the aforementioned absorption-extraction trade-off comes into play since the absorption lengths exceed the charge transport lengths inside CQD films. Light management by increasing the optical path lengths in the CQD film through nanostructures is considered one approach to overcome this trade-off.

Most of the light management techniques adopted for CQD solar cells rely on increasing the number of effective passes that a photon takes through the light absorbing material. The conventional planar CQD cell is referred to as a double-pass design, which means when a photon enters the cell, it passes through the CQD film, gets reflected at the back contact and passes through the CQD film once again before leaving the cell. As is illustrated in figure 1-13-a, it has been shown that by tilting the cell and using a folded light path design, the double-pass structure can be transformed into a multi-pass design [38].

Another approach taken for light absorption enhancement in CQD cells involves nanostructures of pyramid-shaped in the bottom electrode [39]. This technique is demonstrated in figure 1-13-b. The pyramids are shown to increase the external quantum efficiency of the device at absorption-limited wavelengths near the absorber band edge. Again, this is possible because of the increase light path length inside the absorbing film.

Taking advantage of fabrication methods such as nanoimprint lithography [40] and nanosphere lithography [41] to fabricate periodic photonic structures which can induce absorption enhancement through light localization and waveguiding has also been demonstrated to be an effective light management method for CQD solar cells. As depicted in figure 1-13-c, nanoimprint lithography-fabricated ZnO trenches have been proved to be able to manipulate light path inside the CQD layer [40]. In addition, periodic nanostructuring of the CQD layer itself, as illustrated in

figure 1-13-d, has been successfully attempted and shown to enhance broadband absorption compared to a planar device without compromising charge extraction efficiency of the device since the CQD film thickness has not been changed in this new design.

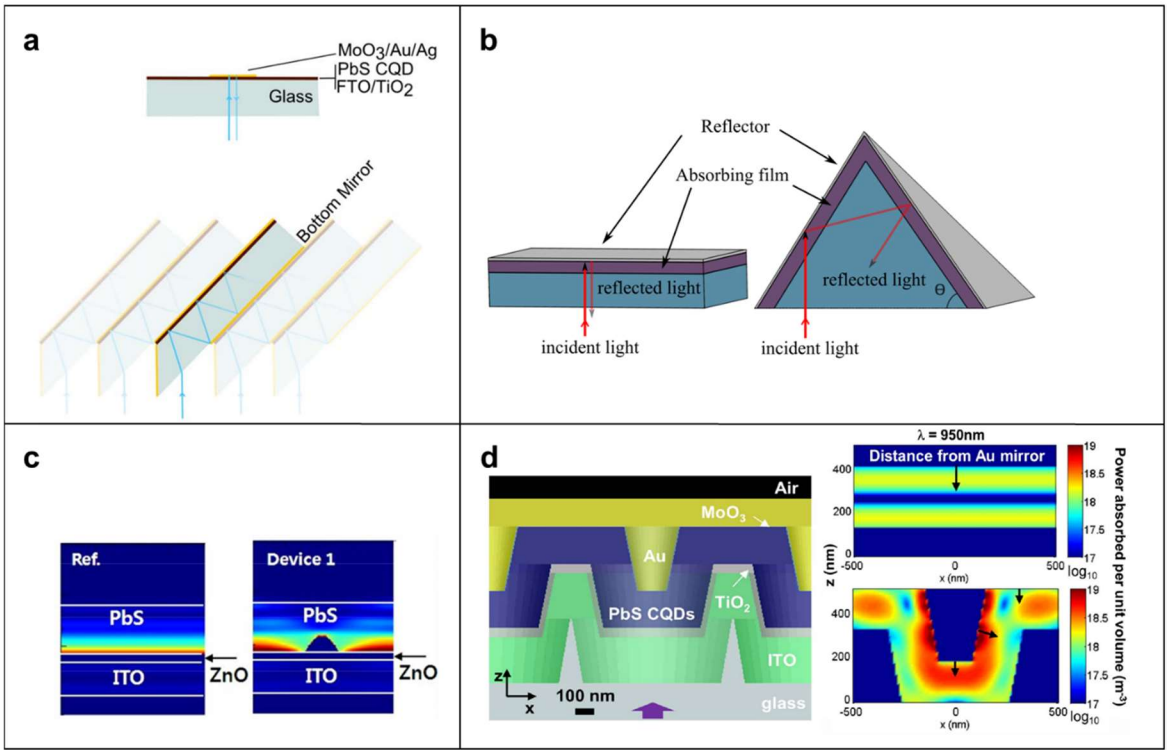

Figure 1-13: Light management techniques recently developed for CQD solar cells. (a) folded light pass design. ***Reprinted from [38] under creative commons license.*** *(b) pyramid-shaped bottom electrode.* ***Reprinted with permission from [39]. Copyright (2015) American Chemical Society.*** *(c) ZnO nanostructures using nanoimprint lithography.* ***Reprinted with permission from [40]. Copyright (2013) American Chemical Society.*** *(d) nanostructuring of the CQD layer using nanosphere lithography.* ***Reprinted from [41] under creative commons license.***

1.3.2. Light emitting devices

As was mentioned previously, the undesirable light trapping happens at almost every layer inside the LED's structure and thus light management strategies for light extraction enhancement in LEDs can be applicable to any of the layers forming the device. Here, we briefly review the most common light management techniques used in thin-film LED devices.

One of the most convenient and effective methods for light management in thin-film LEDs is substrate modification. The most basic way of substrate modification is the use of surface roughness on the outer side of the substrate [42], [43], as shown in figure 1-14-a. The rough surface can contribute to the extraction of waveguided modes at the substrate/air interface by locally manipulating the critical angle for total internal reflection at the surface. The waveguided at the other interfaces of the devices however will remain unaffected. Another popular technique for substrate modification is the use of backside patterned substrates in device fabrication [44], [45]. The shape of the pattern can be designed such that the escape cone from the substrate will be enlarged making it easier for light to couple out of the substrate. This concept for a spherical substrate pattern is depicted in figure 1-14-b.

A different light management strategy applicable to thin-film LEDs is the use of scattering medium for light extraction. In this method, material and structures capable light scattering can be designed in a way that they are able to locally manipulate the refractive index contrast at the interface between two layers in the device and thus promote light extraction. This strategy provides the advantages such as maintaining a constant color over all viewing angles, uniform light distribution and symmetric illumination. One low-cost way of creating a scattering medium for light extraction purpose is the use of texturing meshed surfaces as illustrated in figure 1-15-a [46].

As depicted in the figure, due to random changes in refractive index inside the medium created by the mesh network, light scattering can easily occur which can increase the chance of light extraction as a result of light propagation direction redistribution attributed to the scattering medium. This method is proven to be independent of the emitted light wavelength as a direct consequence of its random structure.

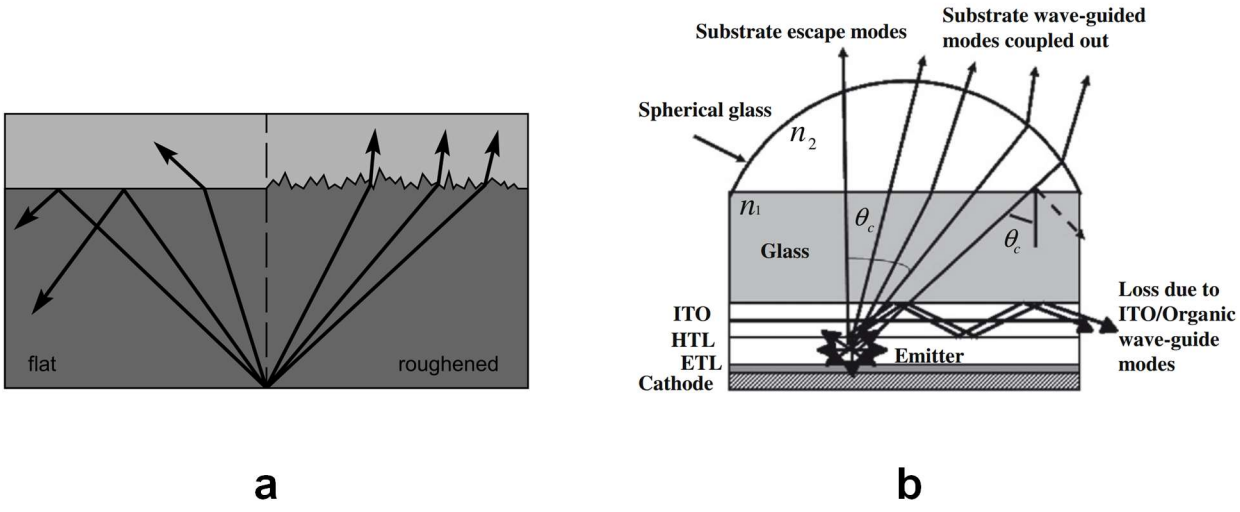

Figure 1-14: Extraction of waveguided modes in thin-film LEDs by using substrate modification techniques (a) Rough outer surface. ***Reprinted from [47], Copyright (2011), with permission from Elsevier.*** *(b) backside patterning.* ***Reprinted from [30], Copyright (2009), with permission from Elsevier.***

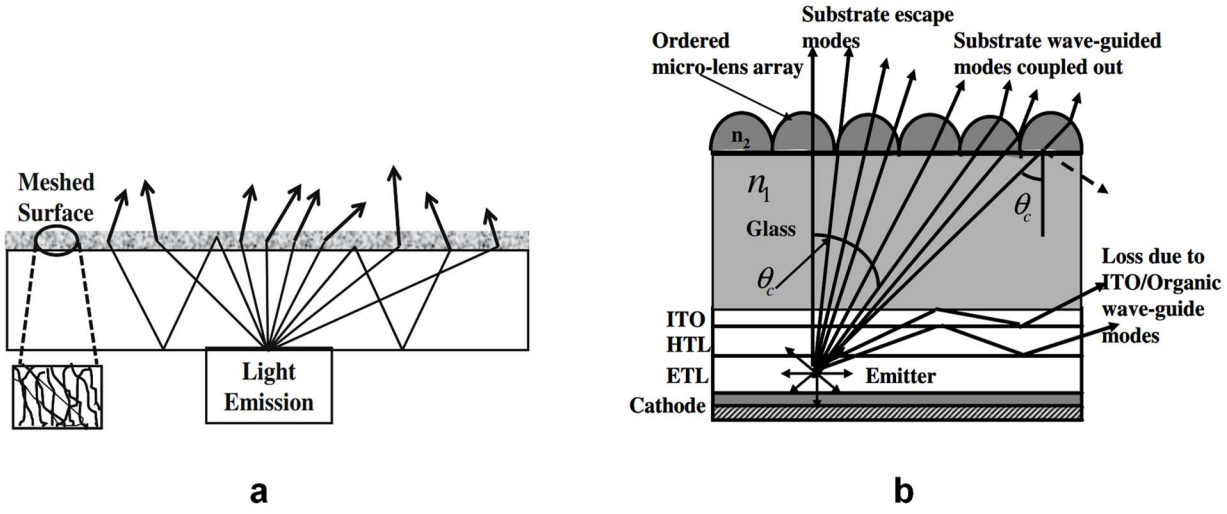

Figure 1-15: Extraction of waveguided modes in thin-film LEDs by using scattering media (a) Texturing meshed surface (b) Ordered periodic structure. ***Reprinted from [30], Copyright (2009), with permission from Elsevier.***

Another way of formation of a scattering medium is fabrication of an ordered periodic structure as depicted in figure 1-15-b. Depending on the way it is ordered, the periodic structure can form a

one or two dimensional diffraction lattice which can act as a strong scattering medium due to the periodic change in refractive index at its interface. A vast variety of materials and structures such as ordered micro-lens arrays [48], [49], diffraction gratings [50], [51], pyramid arrays [52], [53] and micro-sphere arrays [54] have been exploited to leverage the light management capabilities of a scattering medium, just to name a few.

A rather newer strategy for light extraction enhancement in thin-film LEDs involves the incorporation of photonic crystals in the structure of the devices. Thanks to their multi-dimensional periodic structure which enables them to form a photonic bandgap, photonic crystals are capable of control and manipulation of the propagation of light at different directions for different wavelengths [55]. Photonic crystals can contribute to light management in thin-film LEDs in two ways. When the period of the photonic crystal is equal to the wavelength of the supported guided mode, the trapped light propagating parallel to the interface of the layers will be coupled to the direction normal to the device's surface (radiation mode) since the Bragg diffraction condition is satisfied [30]. This concept is illustrated in figure 1-16-a. Furthermore, the photonic bandgap formed in the direction parallel to the interface can prohibit lateral light propagation, forcing light to couple to outward radiation modes. Photonic crystals can be exploited for light outcoupling from various interfaces inside the structure of thin-film LEDs including but not limited to charge transport layer/transparent conductive oxide interface [56] and substrate/transparent conductive oxide interface [57]. One major drawback of photonic crystals for light management is their tendency to modify the far-field radiation pattern as a result of their periodic structure [30].

Excitation of free electrons at the surface between a dielectric and a metal (surface plasmon) can also be exploited to enhance light extraction in thin-film LEDs [58]. Normally, the coupling between light emitting materials and surface plasmon modes supported by the smooth and flat metallic cathode in thin-film LEDs can cause loss in efficiency due to the excitation of non-

radiative surface plasmons which will decay away from the metal-dielectric interface as an evanescent wave. As is shown in figure 1-16-b, by careful engineering of the structure of the cathode, it is possible to convert non-radiative surface plasmons into radiative modes. This has been proven to be feasible by periodic structures with a period in the same order as the emitted light wavelength [59].

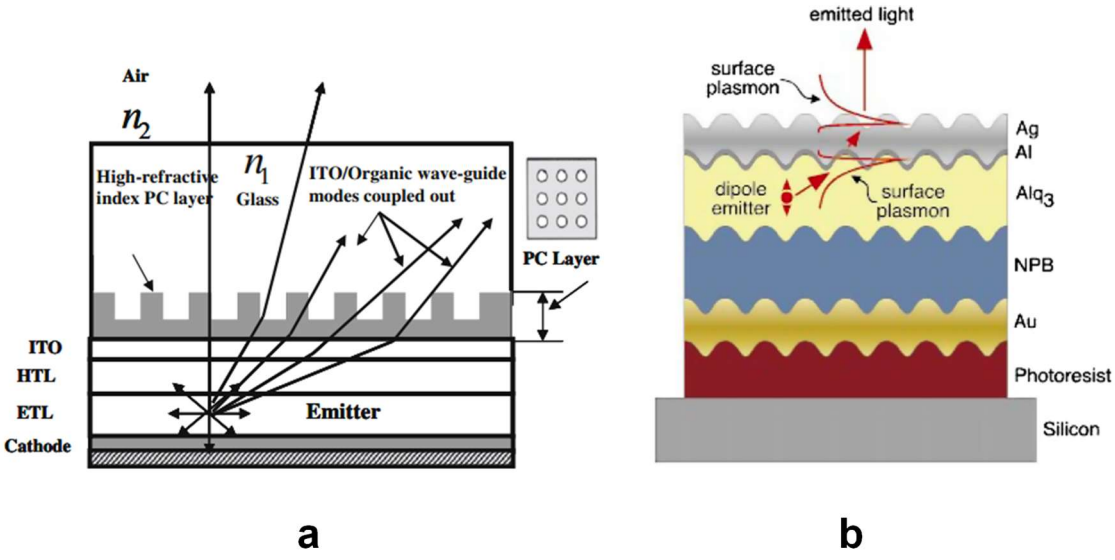

Figure 1-16: Extraction of waveguided modes in thin-film LEDs by using (a) photonic crystals (b) surface plasmons ***Reprinted from [30], Copyright (2009), with permission from Elsevier.***

In addition, recent advances in nanofabrication processes including interference lithography, electron-beam lithography and nano-imprinting has enabled researchers in the field of thin-film LEDs to incorporate numerous nanomaterials and nanostructures into these devices for the purpose of light management [60]-[75]. Both periodic and aperiodic nanostructures have been taken advantage of to promote light extraction capabilities of thin-film LEDs. Periodic nanostructures have the potential to convert guided waves traveling inside high refractive index layer of the device into external leaky waves. Non-periodic nanostructures, on the other hand, can act as scattering sites for light outcoupling at the interfaces inside the device. Their main

advantage over periodic nanostructures is that the LED's emission color and light intensity will remain independent of viewing angle and their extraction performance remains insensitive to the emission wavelength.

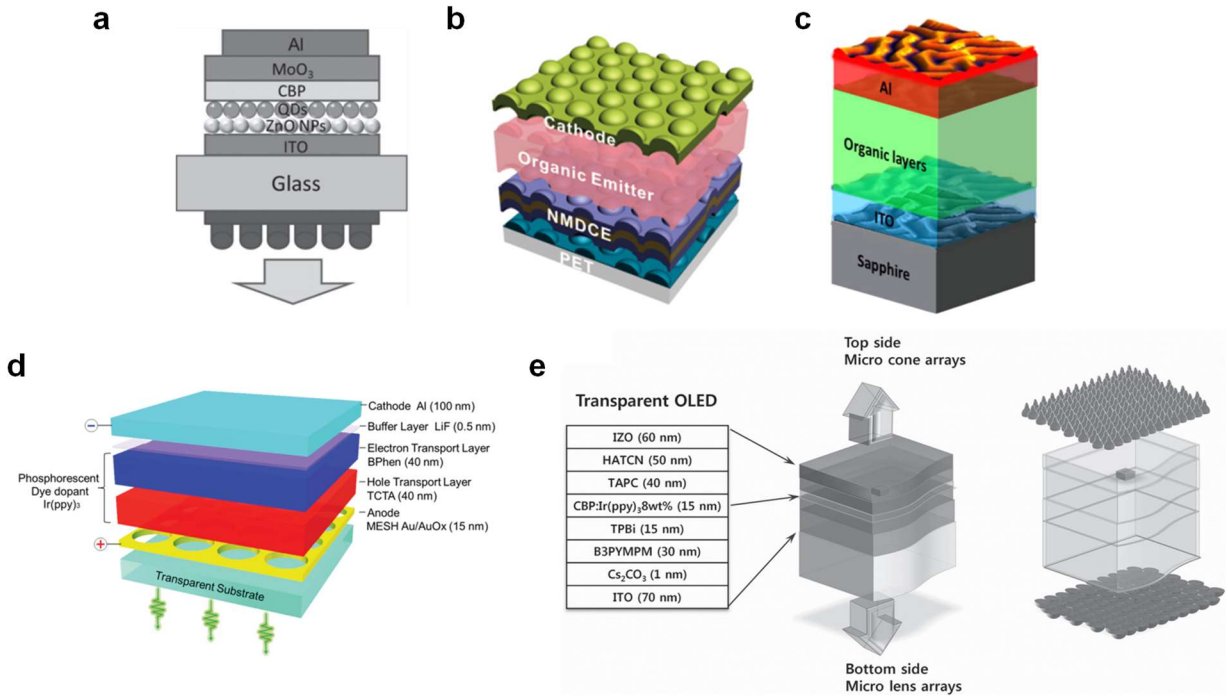

Figure 1-17: Examples of the use of dielectric and metallic nanostructures for light management in thin-film LEDs. (a) ZnO nanopillar arrays on quantum dot LEDs ***Reprinted with permission from [74]. Copyright (2014), Wiley-VCH.*** *(b) Nanostructured transparent metal-dielectric composites for flexible organic LEDs.* ***Reprinted with permission from [73]. Copyright (2016) American Chemical Society.*** *(c) Organic LEDs fabricated on corrugated sapphire substrates* ***Reprinted with permission from [75]. Copyright (2015) American Chemical Society.*** *(d) Gold nanocavities on organic LEDs for plasmonic based enhancement.* ***Reprinted with permission from [62]. Copyright (2014), Wiley-VCH.*** *(e) Micro-cone and micro-lens arrays for transparent organic LEDs.* ***Reprinted with permission from [76]. Copyright (2013), Wiley-VCH****.*

Metallic nanostructures are rarely used for light management in thin-film LEDs due to their parasitic absorption along the light propagation direction. However, it has been shown that metallic nanostructures have larger scattering cross-section than their dielectric counterparts thanks to their localized electromagnetic enhancement [77]. This alongside the potential for excitation of surface plasmons has still kept metallic nanostructures inside the circle of interest of

LED research community. Dielectric nanostructures, on the other hand, are more popular for light extraction efficiency enhancement due to their lack of absorption over a wide range of wavelengths and have been used in the form of nanorods, nanowires, nanotubes, nanoparticles, nanocavities and a variety of other structures. Some recent examples of metallic and dielectric nanostructures incorporated into the structure of thin-film LEDs are shown in figure 1-17. Due to the large extent of degree of freedom available on shape, material, periodicity, and location for light extracting nanostructures used in thin-film LEDs, this light management strategy has continued to grow in popularity among the LED research community.

1.4. Thesis objective

As was described in previous sections, thin-film optoelectronic devices are held back by their lackluster efficiency in competition with their traditional counterparts, despite offering significant advantages such as physical flexibility and cost-effectiveness. Since one major factor in low performance of these devices is known to be their deficiency in light absorption or extraction (especially in the case of thin-film solar cells and light emitting diodes), seeking for better light management seems to be an intuitive approach to boost thin-film optoelectronic devices performance. Although various materials and structures have been studied for the purpose of light management in thin-film optoelectronic devices for more than two decades, only a small number of the proposed solutions (such as micro-lenses for light extraction in LEDs) have deemed to be commercialized. This is mainly attributed to the high cost of materials used in the proposed solution or the complexity of the fabrication process which can drive up the ultimate cost of the fabricated devices.

In this thesis, the main objective is to seek simple and low-cost solutions at nanoscale for light absorption and light extraction deficiencies in thin-film photovoltaic devices and light emitting diodes, respectively. This objective was aimed to be accomplished using easily fabricable

hierarchical nanostructures by taking advantage of theory, simulation and experimental design, fabrication and characterization. Preference was given to light management solutions that require minimal or no change in the structure of the devices so that they can be applicable to any previously fabricated device which can increase the potential for commercialization. In addition, physical flexibility of the designed light management solutions was considered an important criterion for design in order to make sure that the solution is compatible with modern flexible optoelectronic devices as well as traditional ones.

1.5. Thesis outline

Chapter 2 is dedicated to the study of resonance-induced absorption enhancement in colloidal quantum dot solar cells using nanostructured electrodes. Colloidal quantum dot (CQD) solar cells have been under the spotlight in recent years mainly due to their potential for low-cost solution-processed fabrication and efficient light harvesting through multiple exciton generation (MEG) and tunable absorption spectrum via the quantum size effect [24]. In this chapter, the application of nanostructured indium-doped tin oxide (ITO) electrodes as diffraction gratings for light absorption enhancement in colloidal quantum dot solar cells is numerically investigated using finite-difference time-domain (FDTD) simulation. Resonant coupling of the incident diffracted light with supported waveguide modes in light absorbing layer at particular wavelengths predicted by grating far-field projection analysis is shown to provide superior near-infrared light trapping for nanostructured devices as compared to the planar structure. Among various technologically feasible nanostructures, the two-dimensional nano-branch array is demonstrated as the most promising polarization-independent structure and proved to be able to maintain its performance despite structural imperfections common in fabrication.

In chapter 3, a stretchable transmissive hexagonal diffraction grating, which has the potential to act as an optical diffuser, is demonstrated. Leveraging the simplicity of the self-assembly

fabrication process, the photon manipulation capability of polystyrene nanosphere arrays, and elastomeric properties of polydimethylsiloxane, the proposed device is capable of reproducible in situ tuning of both diffraction efficiency and spectral range. While being able to achieve maximum diffraction efficiencies of about 80%, the device displays highly efficient and broadband light diffusion fairly independent of incident light polarization and angle of incidence. Due to its efficient and tunable diffraction capabilities, one potential application of the reported device can be broadband photon management in solar cells and photodetectors by significant increase of the light path length inside the light-absorbing thin films of these devices. As a proof of concept, the proposed optical diffuser is utilized for light absorption enhancement in colloidal quantum dot semiconductor thin films. The demonstrated devices enable integration of cheap and widely used materials with simple cost-effective fabrication for photon management in optics, photonics, and optoelectronics.

Chapter 4 will leverage a modeling approach for optoelectronic engineering of colloidal quantum-dot solar cells. Using comprehensive optoelectronic modeling and simulation, we demonstrate the presence of a strong efficiency loss mechanism, here called the “efficiency black hole”, that can significantly hold back the improvements achieved by any efficiency enhancement strategy. We prove that this efficiency black hole is the result of sole focus on enhancement of either light absorption or charge extraction capabilities of CQD solar cells. This means that for a given thickness of CQD layer, improvements accomplished exclusively in optic or electronic aspect of CQD solar cells do not necessarily translate into tangible enhancement in their efficiency. The results suggest that in order for CQD solar cells to come out of the mentioned black hole, incorporation of an effective light trapping strategy and a high quality CQD film at the same time is an essential necessity. Using the developed optoelectronic model, the requirements for this incorporation approach and the expected efficiencies after its implementation are predicted as a roadmap for CQD solar cell research community.

In chapter 5, I report on a novel volumetric optical diffuser based on cellulose nano-crystals (CNCs) embedded in Polydimethylsiloxane (PDMS) or as I call it "CNP hybrid optical diffuser". By offering a very simple and low-cost fabrication process as well as compatibility with large-scale production using an earth-abundant material (cellulose) as filler, the proposed optical diffuser is an ideal choice for integration into optoelectronic devices for light management especially due to its insensitivity to physical damage at its surface and the lack of requirement for an index-matching layer between the diffuser and the optoelectronic device thanks to the unique surface properties, mechanical flexibility and optical transparency offered by PDMS as the bulk material. I demonstrate that CNCs are an excellent candidate for filler material in a volumetric optical diffuser providing excellent capabilities for broadband light softening in visible and near-infrared range of light and highly efficient light diffusion at very low concentrations. It is shown that at its optimized form, a CNP hybrid optical diffuser is capable of achieving super-high haze values (up to 85%) while maintaining a high degree of transparency (~85%) at the same time. As a proof of concept, I leverage light management capabilities of CNP hybrid optical diffusers to demonstrate their potential for light absorption enhancement in thin-film silicon solar cells and light extraction improvement in organic LEDs.

Finally, a summary of the key findings of the thesis and their potential impact on thin-film optoelectronic devices technology will be discussed in chapter 6. Furthermore, the possible future steps to extend the utility of the proposed light management solutions beyond the status quo are also elaborated.

2

Resonance-induced absorption enhancement in colloidal quantum dot solar cells using nanostructured electrodes

2.1. Background

Periodic nanostructured gratings have shown great potential for light trapping in various types of thin-film solar cells. Metallic gratings have been employed for enhancing light harvesting performance by excitation of free electrons at the surface between a dielectric and a metal (surface plasmons) [37], [78], [79]. However, metallic gratings are prone to parasitic light absorption which competes against the absorption in active layer [80]. Dielectric nanostructured diffraction gratings have also been at the center of attention because of their properties of refraction and the ability to excite light trapping modes inside solar cell active layer. It has been shown that dielectric diffraction gratings are superior to metallic gratings when placed at the same place inside a solar cell's structure [81].

In this work, various structures of indium-doped tin oxide (ITO) electrodes in colloidal quantum dot (CQD) solar cells as diffraction gratings have been investigated for light trapping. We show

that grating far-field projection analysis can be used for thin-film solar cells to predict the wavelengths at which guided-mode resonances responsible for absorption enhancement are excited. Also, a new type of nanostructured diffraction grating (two-dimensional ITO nano-branch array) is proposed as the best performing and polarization-independent structure for light absorption enhancement in CQD solar cells. Finally, simulation results show that ITO nano-branches performance is fairly insensitive to fabrication imperfections and flaws, therefore they seem to be promising in fabrication for light trapping inside CQD solar cells.

There are several architectures introduced for CQD based photovoltaic device most of which utilize the CQDs as the light absorbing layer and an n-type transparent semiconductor to establish the p-n junction. However, the most common and the best performing structure available to date is known as the depleted heterojunction CQD solar cell [82]. The schematic of the structure of a typical depleted heterojunction CQD solar cell based on PbS CQDs is shown in figure 2-1. Glass is being used as the substrate and a layer of transparent conductive oxide (Fluorine doped tin oxide, FTO) on the substrate forms the front contact. A thin layer of TiO_2 or ZnO which is optically transparent in the operating range of the cell serves as the n- side of the junction and the CQD layer plays a double role of being the p- side of the junction and the light absorbing layer. Gold can be used to establish an ohmic contact to CQD layer as the back contact, although it might be preceded by a thin layer of MoO_3 to reduce the energy barrier between the two adjacent layers. In addition, being highly reflective, gold doubles the optical pathway of photons inside the CQD layer, improving the overall light absorption of the device.

The energy band diagram of a depleted heterojunction CQD solar cell is also depicted in figure 2-1. The n- side of the junction is usually highly doped, leading the depletion region to extend in almost the entire CQD layer, making the charge extraction more efficient. Under short-circuit condition, because of the band bending present at the CQD side resulting from the significant doping difference between junction's sides, generated carriers will be mostly extracted with the

aid of the built-in electric field expanded across the depletion region. On the other hand, as the device is forward biased into the power-generating regime, the depletion region will recess and quasi-neutral regions formed inside the CQD layer force the carriers to rely more on diffusion, leaving them vulnerable to recombination by being captured into trap states. This limits the maximum thickness possible for the CQD layer as a thicker layer increases the likelihood of carrier recombination due to their limited diffusion length inside the layer. This is where light management in CQD solar cells, which is the subject of this work, becomes of great importance as it enables the enhancement in amount of light absorption by CQDs without changing the thickness of the CQD film to maintain efficient collection of photo-generated carriers.

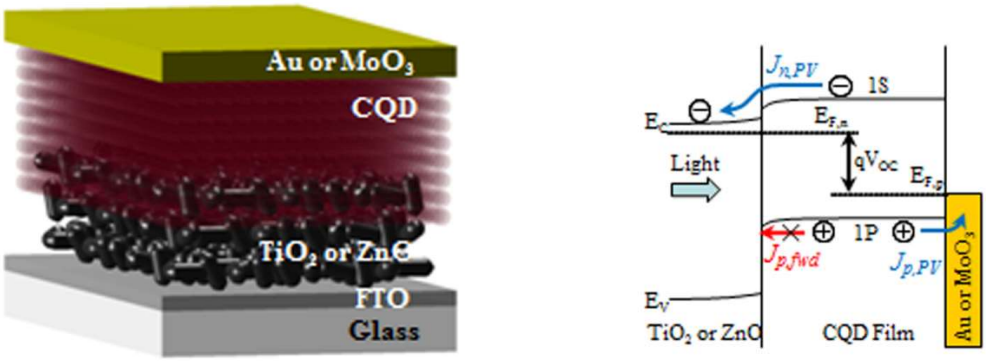

Figure 2-1: Structure of a depleted heterojunction CQD solar cell (left) and its energy band diagram (right) ***Reprinted with permission from [82]. Copyright (2010) American Chemical Society.***

The most basic structure of a diffraction grating is composed of a simple geometric pattern like a triangle that is repeated periodically in one dimension and has a finite thickness. The refractive index of the grating structure should be different than that of at least one of the two surrounding mediums at the top and the bottom of the grating. When the light is incident on grating interface, it will be scattered into multiple transmitted and reflected orders. Each order represents a different direction for scattered light and zeroth order is defined as the order in the same direction as the incident light. This basic diffraction grating structure and the resulting transmitted and reflected orders by normal incident light on grating interface are illustrated in Figure 2-2.

According to the theory, the number and the direction of supported orders depend on properties of the grating structure as well as the incident light and can be quantitatively determined by the following equation [29]:

$$m\lambda = \Lambda(n_i sin\theta_i + n_d sin\theta_d) \tag{2-1}$$

Where n_d and n_i are refractive index of the medium at which diffracted orders and the incident light are traveling, respectively, m is an integer number and represents the m^{th} diffracted order, λ refers to the wavelength of the incident light, Λ is the period of the grating structure and θ_d and θ_i represent the angle of the m^{th} diffracted order and the incident light measured with respect to the normal to grating interface.

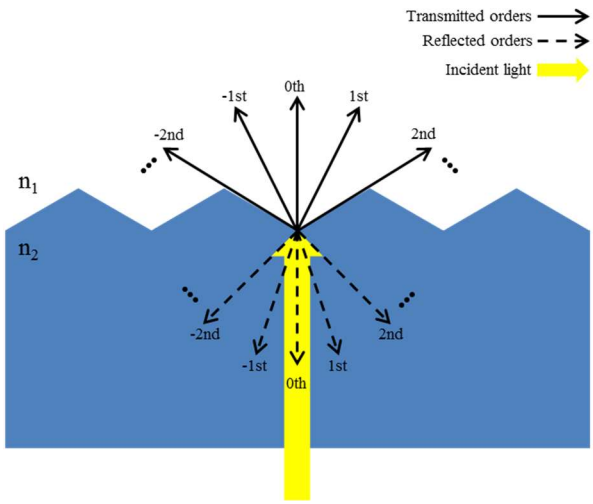

Figure 2-2: Schematic diagram of a basic diffraction grating structure and transmitted and reflected orders caused by normal light incidence on grating interface. ***Reprinted with permission from [83]. Copyright (2014) Optical Society of America.***

As is clear from the equations, for transmitted and reflected orders, the characteristics of the diffracted orders are not dependent on the shape of the grating structure. As a result, all grating structures with the same period and refractive index are expected to show the same scattering behavior in terms of the direction and the number of supported orders. However, as will be

discussed later, the difference in the shape can affect the energy distribution between different orders.

2.2. FDTD simulation: A modeling approach

Simulations in this work are done by Finite-Difference Time-Domain (FDTD) method. This method is known as one of the best methods for solving Maxwell's equations in complex geometries. It is discrete in both time and space. The electromagnetic fields and structures are described on a discrete spatial mesh and Maxwell's equations are solved discretely in time. In the case the mesh cell size goes to zero, this technique can be considered an exact representation of Maxwell's equations. The E-fields in a volume of space are calculated at a certain instant in time and then the M-fields in the same volume are obtained at the next instant in time. This cycle is repeated until a steady-state in EM fields is achieved. Therefore, the FDTD method is capable of calculating how the EM fields propagate from the source through the structure. Time-domain information can be recorded at any spatial point and frequency domain information can be obtained using Fourier transform at the same point. Thus, the frequency dependence of variables can be obtained over a wide range of frequencies from a single simulation.

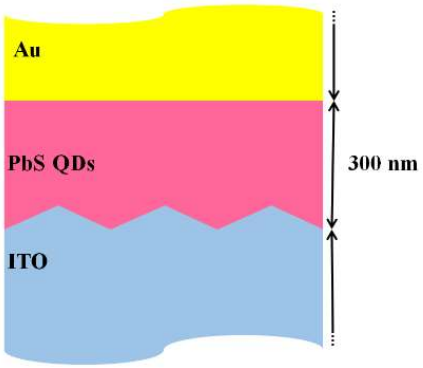

Figure 2-3: Schematic diagram of a PbS colloidal quantum dot solar cell with nanostructured ITO diffraction gratings used for simulation. ***Reprinted with permission from [83]. Copyright (2014) Optical Society of America.***

Simulations were performed by the Lumerical FDTD Solutions software. Schematic diagram of the typical heterojunction CQD solar cell structure [82] used for simulations is illustrated in figure 2-3. PbS quantum dots were chosen as active layer with a thickness of 300 nm which is the maximum thickness for efficient photo-generated carrier collection. A semi-infinite gold layer on top of the active layer serves as the top contact to collect photo-excited holes and back reflector and a semi-infinite indium-doped tin oxide (ITO) layer at the bottom acts as the transparent conducting electrode of the solar cell. There also exists a thin layer of titanium dioxide (TiO_2) layer to collect photo-excited electrons between ITO electrode and PbS quantum dots (QDs), but due to the similarity in optical properties of TiO_2 and ITO, we neglected the TiO_2 layer in all simulations. Grating structures are located at the interface between the ITO electrode and PbS quantum dots. We used the multi-coefficient fitting tool inside the software to model real (n) and imaginary (k) parts of refractive indices of materials from available experimental data [84]-[87]. In the case of grating far-field projection analysis, the dielectric materials were considered to be lossless and the average values of experimental refractive indices were used for ease of analysis.

The light source was a planewave source spanned in the whole simulation area and was placed inside the ITO layer for the purpose of simplicity for simulations. The wavelength range chosen for simulations is 700-1200 nm (near infrared region) at which current technology of PbS CQD solar cells needs absorption enhancement [87]. Periodic boundary conditions were defined for directions perpendicular to the planewave propagation direction because of the periodic nature of the device structure in these directions. For directions parallel to propagation direction, perfectly matched layer (PML) boundary conditions were defined. In order to calculate the amount of absorption inside the active layer, two power monitors were placed at the bottom and the top of the active layer to measure the power flow getting in and out of the layer, respectively. The power absorbed by the layer is obtained by calculating the power flow difference between the two monitors. To further verify the results acquired by this approach, the total absorption inside

the active layer was also calculated by using frequency-domain field profile monitors. The results obtained by both methods are very close to each other. All calculated powers are normalized to the power injected by the light source, which in turn is normalized to AM 1.5G solar spectrum data available from NREL [88]. Power absorption profiles were obtained by using the Poynting Theorem for a non-magnetic medium [89]:

$$P_{abs} = \frac{1}{2}\omega\varepsilon_o Im\{\varepsilon_r\}|E|^2 \tag{2-2}$$

Where ε_o is vacuum permittivity, ε_r depicts dielectric constant, ω refers to the angular frequency of the fields, and $|E|$ represents the magnitude of electric field at the desired point inside the device structure.

In order to have a reliable criterion for comparison between different grating structures in terms of light absorption, we considered a reference structure without any grating pattern between ITO and active layer. We call this structure as the flat structure. All grating structures are compared to the flat structure by a factor called absorption enhancement, which is defined according to the following equation:

$$Absorption\ enhancement(\%) = \frac{P_g - P_f}{P_f} \times 100 \tag{2-3}$$

Where P_g refers to the power absorbed by the cell with ITO grating structure and P_f depicts the power absorbed by the flat structure. All presented absorption enhancement factors are the average on the whole simulation range. Also, to be able to fairly compare the light absorption enhancement for different grating structures, the dimensions of the gratings are chosen such that they occupy the same volume inside the active layer so each cell includes the same volume of light absorbing material in both 2D and 3D simulations. No optimization has been done on the geometry of any of the grating arrays and a period of 500 nm was chosen for all of the grating structures under study.

For studying the diffraction behavior of the grating structures by grating far-field projection analysis, a monitor was placed inside the active layer between the grating structure and the top contact and another one was placed inside the ITO layer. This configuration enabled us to analyze the diffraction efficiency of grating structures for transmitted and reflected orders. A field intensity versus time monitor was used in all simulations to ensure the convergence of simulations.

2.3. Light trapping by one-dimensional nanostructured ITO diffraction gratings

As discussed before, periodic dielectric nanostructures are able to excite a variety of light trapping modes inside thin-film solar cells via resonant coupling of sunlight to the modes supported by solar cells. Here, four different one-dimensional nanostructured ITO diffraction grating structures including triangular, nano-pillar, nano-well, and nano-branch structures were investigated in terms of light trapping performance. First, grating far-field projection analysis [90] was used to study the light trapping behavior of 1D nanostructured ITO diffraction gratings in CQD solar cells. The obtained reflection and transmission diffraction efficiency of the triangular ITO gratings as a function of wavelength for both transverse electric (TE) and transverse magnetic (TM) polarizations of light are shown in figure 2-4. As is clear from the figure, at some particular wavelengths, a considerable decrease in reflection or equivalently increase in transmission can be observed. This can be attributed to the excitation of resonant modes inside the active layer of CQD solar cell caused by ITO diffraction gratings. The important point to mention here is that according to transmission diffraction efficiency plots, at resonance wavelengths, most of the light is diffracted into orders higher than zeroth order which indicates that the grating structure shows a very impressive light scattering performance when resonant modes are excited inside the device.

In addition, a close scrutiny of reflection diffraction efficiency plots reveals that at wavelengths larger than 750 nm, no reflection has been occurred at orders higher than the zeroth order. This can be confirmed by referring to the grating equation for reflected orders using equation 2-1. Based on the equation, for wavelengths longer than 750 nm, no orders higher than zeroth order are supported by a grating structure with a period of 500 nm, refractive index of 1.5 and normal light incidence. This property, which is specific to grating structures with dimensions smaller than or in the same order as the incident light wavelength, can cause a larger proportion of light to enter the active layer by not allowing reflection in orders higher than the zeroth order [91].

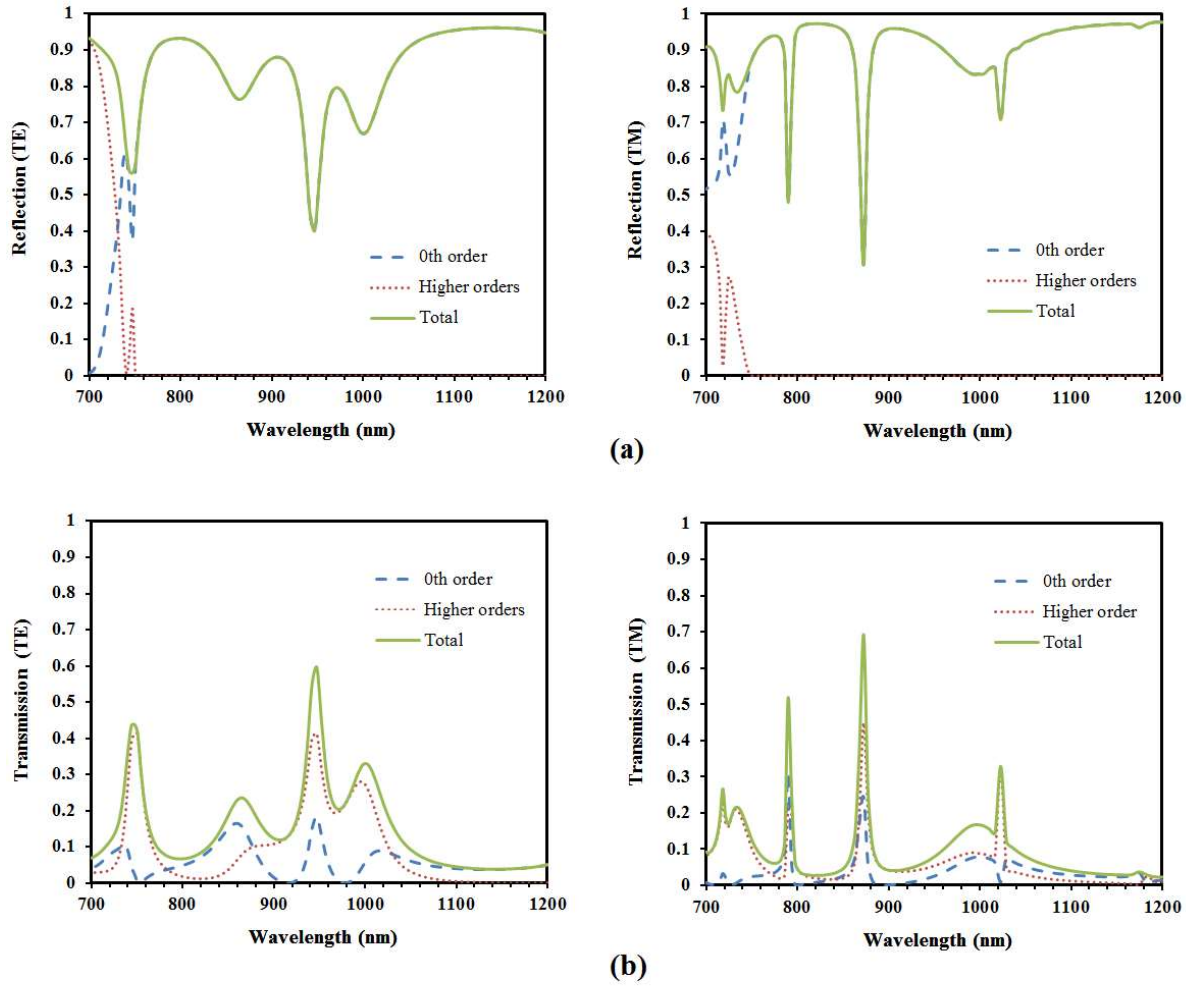

Figure 2-4: (a) Reflection and (b) Transmission diffraction efficiency of triangular ITO gratings as a function of wavelength for TE (left) and TM (right) light polarizations. Plotted efficiencies are for zeroth order, higher orders

and total diffracted orders. ***Reprinted with permission from [83]. Copyright (2014) Optical Society of America.***

Grating projection analysis can also be used to determine the number and the direction of supported diffracted orders by grating structures at particular wavelengths. Figure 2-5 depicts transmission efficiency as function of direction for supported diffracted orders of triangular ITO gratings at select on-resonance and off-resonance wavelengths of TE polarized light. As can be inferred from the results, at resonance, most of the light is scattered into the orders higher than the zeroth order, which is consistent with the results from Figure 2-4. As there is a good contrast between the active layer and the layers around it in terms of refractive index, the active layer can potentially act as a waveguide in the middle of the solar cell's structure [80].

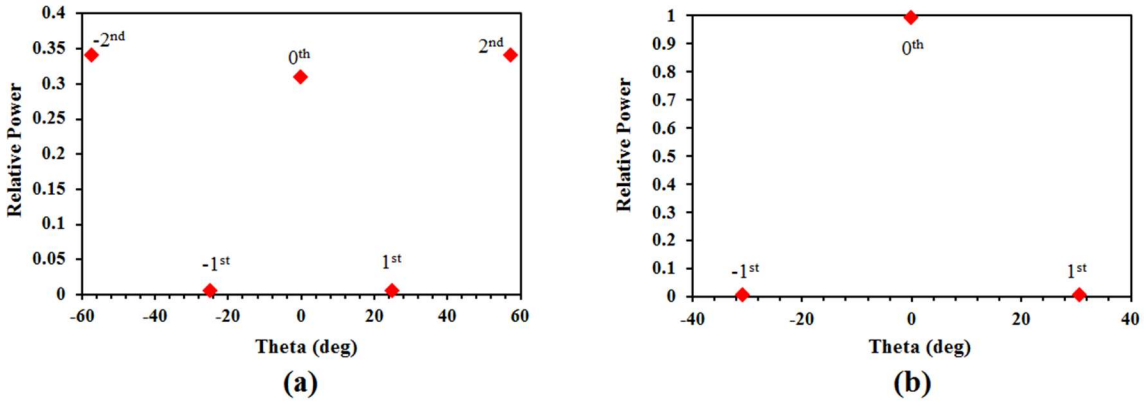

Figure 2-5: Relative transmission efficiency as a function of direction of diffracted orders for triangular ITO gratings at select (a) on-resonance (947 nm) and (b) off-resonance (1150 nm) wavelengths for TE polarization of light. ***Reprinted with permission from [83]. Copyright (2014) Optical Society of America.***

If the order into which most of the light is scattered has a direction suitable for guided-mode excitation inside the solar cell's active layer, phase-matched coupling of the incident light with supported guided-modes of the active layer (guided-mode resonance) [36] can effectively trap light inside the PbS quantum dot layer and greatly enhance the absorption. In contrast, for off-resonance wavelengths, as most of the light is not diffracted, guided-mode resonance cannot be excited and significant improvement in light absorption is not expected. We were able to validate the obtained number and the direction of supported orders by using equation (2-1). However, as

was mentioned before, grating theory is not able to predict the energy distribution between different orders. In fact, we found out that energy distribution between different orders varies significantly by the change in the shape of grating structure and that is why different grating structures have resonance peaks at different locations of the spectrum.

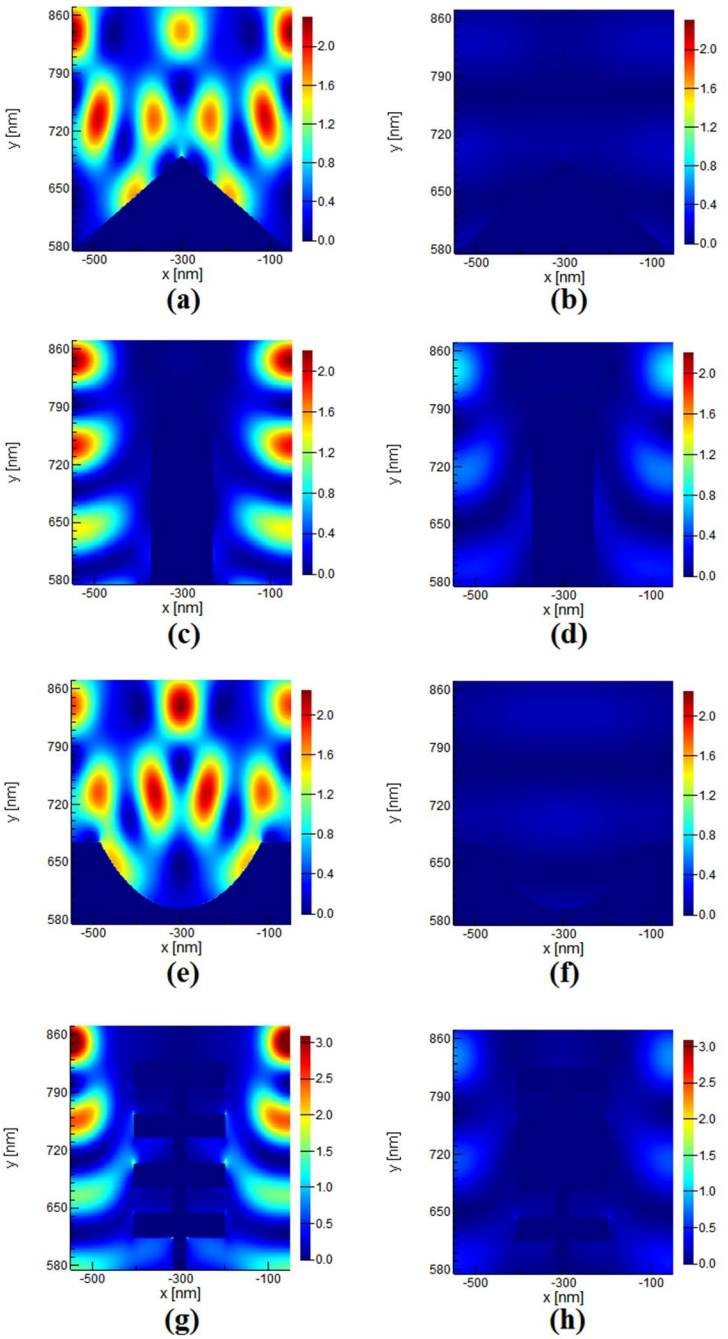

Figure 2-6: Light absorption profile for (a,b) triangular (c,d) nano-pillar (e,f) nano-well (g,h) nano-branch ITO gratings at select on-resonance (a,c,e,g) and off-resonance (b,d,f,h) wavelengths for TE polarization of light. ***Reprinted with permission from [83]. Copyright (2014) Optical Society of America.***

To further verify the light trapping ability of 1D ITO nanostructured diffraction gratings, light absorption profiles for solar cells with different grating structures were examined. Figure 2-6 illustrates light absorption profiles for one period of the investigated grating structures at select on-resonance and off-resonance wavelengths for TE polarized light. All the profiles disclose numerous absorption hot spots for on-resonance wavelengths while almost no hot spot is visible at off-resonance wavelengths. This confirms the contribution of resonant coupling of light with supported modes inside the active layer to light absorption enhancement in CQD solar cells. Moreover, periodic variation in intensity of absorption hot spots denotes the guided-mode resonance nature of the light trapping process happening in structures under investigation [36].

The ultimate criterion for light absorption performance of every type of solar cell is the overall absorption over a broadband spectrum. Absorption spectra of CQD solar cells with different 1D ITO diffraction gratings for TE and TM polarization of light obtained by broadband FDTD simulation are shown in Figure 2-7. Absorption spectrum for the CQD solar cell without any diffraction grating (flat structure) and the power available by the sun are also included as reference for comparison. Absorption enhancement factor for each of the grating structures compared to the flat structure is shown in inset.

It can be concluded from the results that triangle and nano-well gratings demonstrate a relatively similar light absorption performance for both types of light polarization, which can be attributed to the similarity in their physical shape. A similar conclusion can be drawn for nano-pillar and nano-branch gratings. Overall, the triangular grating which is the best performing structure for TE-polarized light showed 30.12% absorption enhancement over the flat structure and nano-

branch structure absorbed 32.94% more TM-polarized light than the flat structure, which is more than any other grating structure.

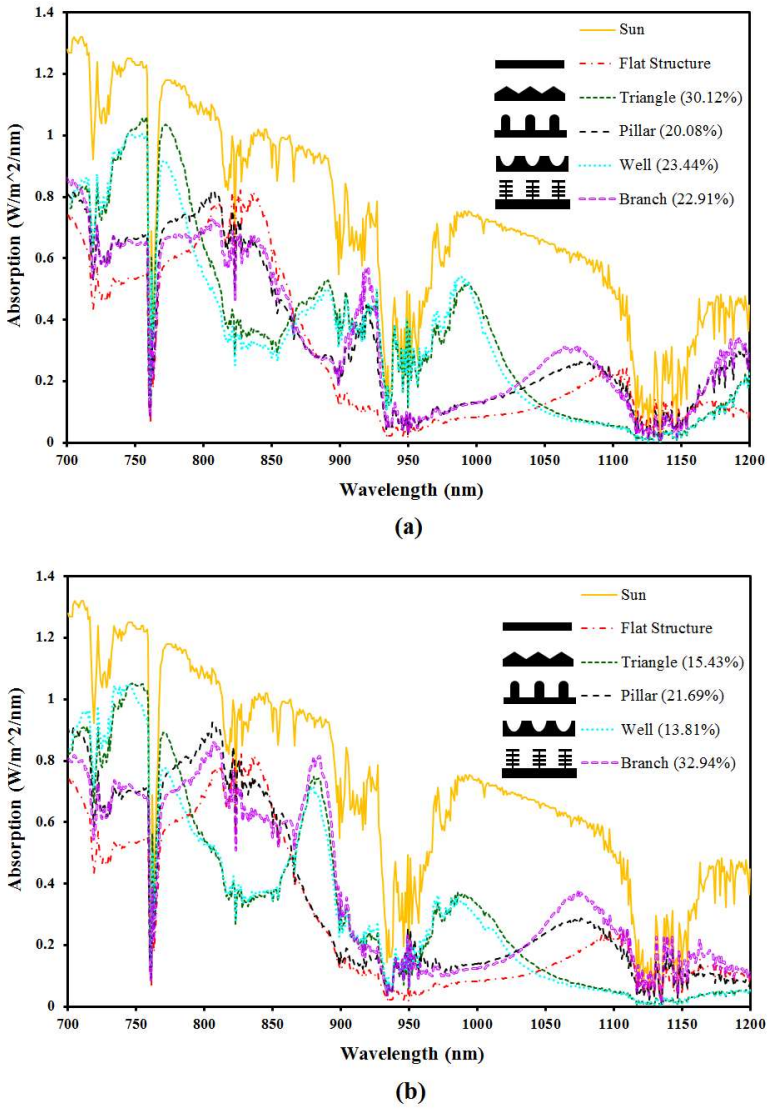

Figure 2-7: Simulated absorption spectra of CQD solar cells with different 1D ITO diffraction gratings for (a) TE and (b) TM light polarizations. The power available by the sun and the absorption spectra for solar cell without any diffraction gratings (flat structure) are also included for comparison. Absorption enhancement factor for each grating structure over the flat structure is shown in inset. ***Reprinted with permission from [83]. Copyright (2014) Optical Society of America.***

In addition, by comparing the diffraction efficiency results obtained from grating far-field projections in Figure 2-4 with the absorption spectra results acquired from broadband FDTD simulation, one can notice a meaningful consistency between the location of guided-mode

resonance peaks and the locations at which there is a considerable enhancement over the flat structure light absorption spectrum. This further emphasizes the important role of guided-mode resonances excited by ITO diffraction gratings in light absorption enhancement for CQD solar cells. Moreover, it shows that grating far-field projections can be used to predict the wavelengths at which guided-mode resonances take place in CQD solar cells. This eliminates the need for time-consuming broadband FDTD simulation to design structures for resonance excitation at desired frequencies.

2.4. Polarization-independent two-dimensional nanostructured ITO diffraction gratings

The problem about any kind of one-dimensional diffraction grating structure is that the performance of the structure is strongly dependent on the polarization of the incident light. This dependence on polarization was obvious from the results obtained for 1D ITO grating structures investigated in previous section. Two-dimensional diffraction gratings, however, do not suffer from this problem because of the 2D symmetry in their structure. Therefore, we tried to extend our investigation for light trapping performance of nanostructured ITO diffraction gratings to 2D grating structures. We chose two of the best performing 1D ITO gratings for TE (triangular) and TM (nano-banch) polarizations and extended the design from 1D to 2D to create pyramid and 2D nano-branch gratings. Again, in order to be able to fairly compare the structures, the dimensions of the structures are chosen such that the available light absorbing material volume for solar cells is the same. 3D FDTD simulation was used to study the light absorption performance of the resulting structures. Schematic diagram for one period of the 2D gratings and the resulting absorption spectrum for both TE and TM polarizations of light are shown in Figure 2-8. A similar behavior was also observed for other custom polarizations (30^o, 45^o) of incident light. The nano-branch structure seems to do a better broadband light trapping job with absorption enhancement

factor of 40.14% as opposed to pyramid with 31.45% enhancement mainly because of higher absorption at resonance peaks. Also, the results suggest that the performance of the structures is independent of the incident light polarization which is in agreement with our expectations due to the 2D symmetric nature of the structures.

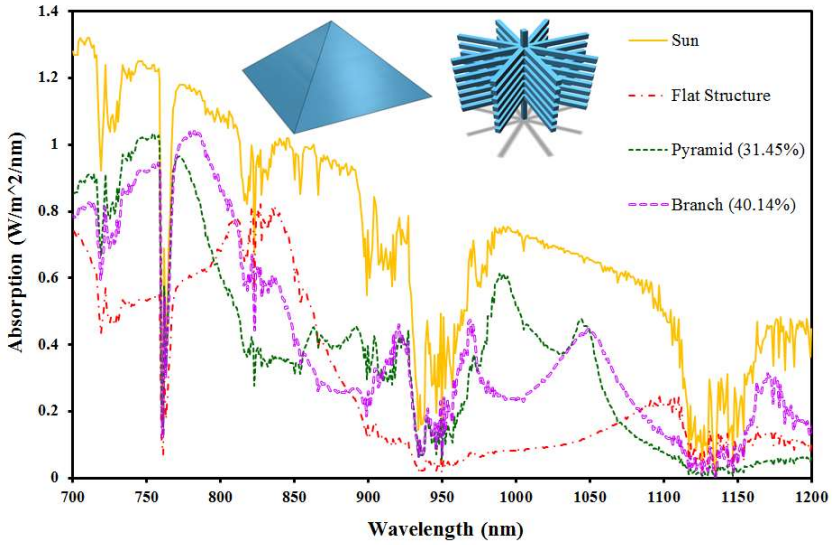

Figure 2-8: Simulated absorption spectra of CQD solar cells with 2D pyramid and nano-branch ITO diffraction gratings for TE and TM light polarizations. The power available by the sun and the absorption spectra for solar cell without any diffraction gratings (flat structure) are also included for comparison. The schematic diagrams of the simulated pyramid and nano-branch ITO gratings are included in the inset. ***Reprinted with permission from [83]. Copyright (2014) Optical Society of America.***

The independence of light trapping performance of 2D diffraction grating structures from incident light polarization can further be affirmed by investigating light absorption profiles for both TE and TM polarizations of light. As is clear from the top-view light absorption profiles for 2D nano-branch ITO gratings at select resonance wavelengths depicted in Figure 2-9, due to the symmetry in the structure of 2D nano-branch, when the polarization changes, the absorption hot spots are rotated around the structure's symmetry axis without any variation in intensity distribution. In addition, the hot spots observed in profiles confirm effective light trapping performance of 2D nano-branch ITO gratings at resonance wavelengths.

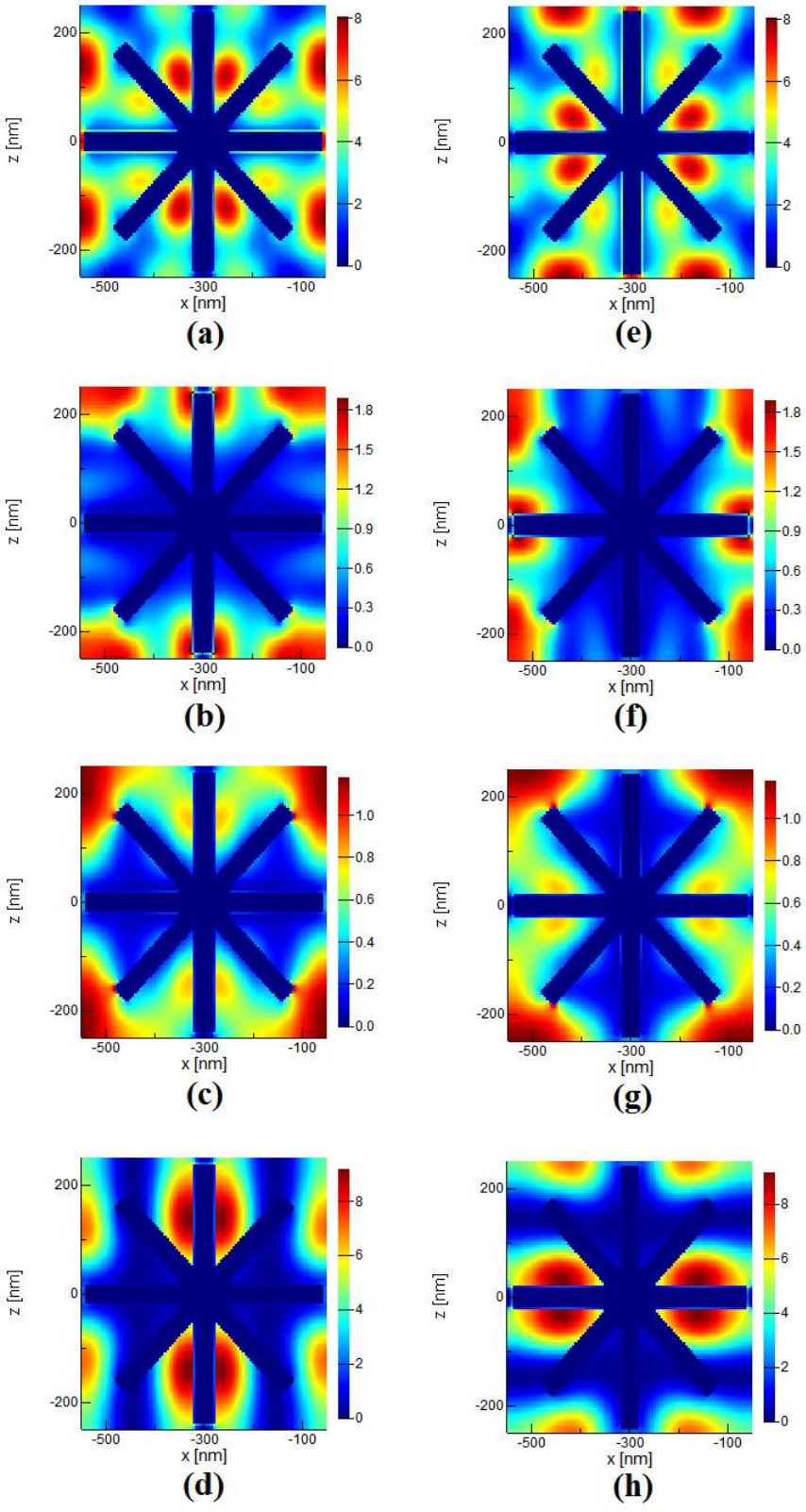
z [nm]
x [nm]
200
0
-200
-500
-300
-100
(a)
(e)
(b)
(f)
(c)
(g)
(d)
(h)

Figure 2-9: Top-view light absorption profile for 2D nano-branch ITO gratings at select resonance wavelengths for TE (a-d) and TM (e-h) polarizations of light. (a,e) 757 nm (b,f) 918 nm (c,g) 1050 nm (d,h) 1167 nm. ***Reprinted with permission from [83]. Copyright (2014) Optical Society of America.***

2.5. Effect of fabrication flaws on performance of two-dimensional ITO nano-branch diffraction gratings

As far as we know, all the modeling and simulation works done on diffraction grating structures in literature have considered the structures to be physically ideal. In reality however, it is not always possible to fabricate perfectly structured diffraction gratings. In the case of ITO nano-branches for example, although it has recently become feasible to fabricate such structures [92]-[94], there is still problems for precise control of the dimensions, arrangement and distribution of nano-branches. Here, we tried to investigate the effect of flaws in branch placement on light trapping performance of 2D ITO nano-branch diffraction gratings. Although it is not possible to impose non-periodic imperfections on grating structures due to the necessity of using periodic boundary conditions, having periodic imperfections can to some degree give us an idea about the performance of non-ideal nano-branch gratings. Therefore, randomly eliminating some of the branches from the grating structure without disturbing its periodic nature was considered a reasonable approach.

Schematic and absorption spectrum for perfect and imperfect 2D ITO nano-branch diffraction gratings are shown in figure 2-10. The results indicate that the imperfect structure closely follows the perfect one in terms of light absorption at most of spectrum wavelengths and even has considerably superior performance at around 990 nm which results in slightly better broadband performance for imperfect structure (41.4%) than the perfect one (40.14%). Top-view light absorption profiles shown in the inset of figure 2-10 for both structures at 990 nm suggest that the enhancement is mainly due to the presence of absorption hot spots inside active layer at some places where the branches have been eliminated. This may be attributed to excitation of local

resonances at spaces created inside the active layer as a result of branch elimination since breaking the symmetry in diffraction gratings is believed to induce extra modes of light trapping [91]. The trend was found to be the same for other randomly modified structures. This indicates the practicality of ITO nano-branch diffraction gratings as a promising approach for light absorption enhancement in CQD solar cells.

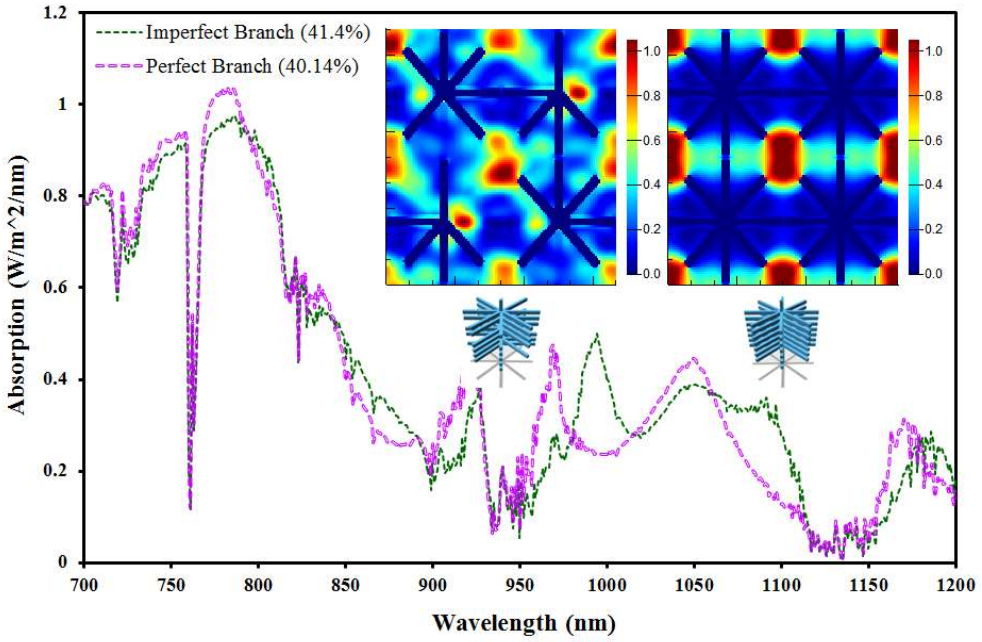

Figure 2-10: Simulated absorption spectra of CQD solar cells with perfect and imperfect 2D nano-branch ITO diffraction gratings. Inset includes schematic and top-view light absorption profile at the wavelength of 990 nm for perfect (right) and imperfect (left) ITO nanobranch gratings. ***Reprinted with permission from [83]. Copyright (2014) Optical Society of America.***

2.6. Conclusions

In summary, using 2D and 3D FDTD simulations, this work has highlighted the potential of nanostructured ITO diffraction gratings as an effective structure for light absorption enhancement in PbS CQD solar cells at near-infrared region where they typically demonstrate weak light absorption. Four different 1D ITO diffraction grating structures (triangular, nano-pillar, nano-well and nano-branch) were investigated and compared to each other in terms of

broadband light absorption. We believe that guided-mode resonances excited by coupling of the incident diffracted light into the supported waveguide modes is the main reason behind the broadband light absorption enhancement in solar cells with ITO grating structures as compared to the reference planar solar cell without any gratings. Moreover, it has been shown that grating far-field projection analysis is a powerful approach to predict guided-mode resonance wavelengths in CQD solar cells. Polarization-independent broadband light absorption enhancement of 40.14% was achieved for 2D ITO nano-branch gratings as the best-performing structure and the absorption enhancement proved to be almost independent of possible fabrication flaws in grating structure. More careful engineering of the nano-branch grating structure may lead to even better light trapping performance and the idea can possibly be extended to other thin-film solar cell technologies.

3

Stretchable hexagonal diffraction gratings as optical diffusers for in-situ tunable broadband photon management

3.1. Introduction

Light diffusion has always been an important requirement for many of the optical and photonic systems where there is a need for the so-called soft light. One of the most common applications of optical diffusers is the backlighting system of the liquid crystal displays (LCDs) [95]-[97]. More recently, emerging applications for optical diffusers such as smart windows [98] and invisible labels [99] have been demonstrated. In addition, light softening has found its way to optoelectronic devices such as solar cells, [36], [83], [100] photodetectors, [101]-[103] and light emitting diodes (LEDs) [104]-[106] to enhance their power conversion efficiency, sensitivity, and brightness, respectively through efficient photon management.

Generally, optical diffusers can be divided into two categories. The first category involves randomly structured diffusers which are usually based on a mixture of materials with different refractive indices in a film [107]-[109]. Although efficient in light softening, the Achilles' heel for randomly structured optical diffusers is their lack of design elements that can be customized for various needs and applications which is a direct consequence of their random nature. On the other hand, the second category includes carefully engineered periodic patterns on a surface [110], [111] , offering lots of degrees of freedom for design and adjustment mostly through tuning of the periodicity. Nanostructured transmissive diffraction gratings can also be considered as a special case of optical diffuser in which the structure's periodicity is comparable to the wavelength of the incident light thus enabling large spatial separation of diffused light based on the wavelength. Unfortunately, most of the proposed periodic structures for optical diffusers and gratings are not in-situ tunable which greatly limits their application range. In-situ tunability means that as an optical element inside an optical system, the performance of the diffuser can be dynamically tuned through a signal of some sort such as mechanical strain or electricity.

In this regard, Polydimethylsiloxane (PDMS) is the material of first choice when it comes to flexible and tunable optical devices due to its superior optical transparency and mechanical properties. In particular, PDMS has recently attracted great attention for tunable optical diffusers and gratings [99], [112]-[114]. The proposed structures, however, require rather complicated and expensive fabrication processes including Glancing Angle Deposition (GLAD) [99], surface wrinkling [113], E-beam lithography and pattern transfer [112] and holographic lithography [114].

While massively famous for their application as a pattern-inducing layer in fabrication of periodic nanostructures [115]-[117] via the so-called colloidal lithography [118], Polystyrene (PS) nanospheres are extremely under-appreciated when it comes to their own optical properties and photon management capabilities as a stand-alone structure. Due to the hexagonal arrangement of close-packed nanosphere assemblies, PS nanospheres can form a hexagonal diffraction grating

[119], [120], which is favorable in integrated optics since they occupy the least space compared to any other periodic arrangement [121]-[124]. Recently it was demonstrated that PS nanospheres can enhance light absorption in silicon solar cells through light softening [125], but to the best of our knowledge, their photon management potential for in-situ tunable optical diffusion has never been explored to date.

Here, we demonstrate the first tunable hexagonal diffraction grating by taking advantage of PS nanospheres as a periodic structure for optical diffusion and PDMS as stretchable substrate for tunability. Through leveraging the simplicity of the self-assembly fabrication process, the tunable optical diffuser illustrated in this work provides the potential for cost-effective light softening. In addition, the ability to tune the light diffusing properties of the optical diffuser by grating diffraction efficiency adjustment across the spectrum offers widespread application for various types of optical systems and optoelectronic devices. As a proof of concept, the capability of the proposed optical diffuser for in-situ tunable photon management in PbS colloidal quantum dot (CQD) semiconductor thin-films is demonstrated.

3.2. Experimental and modeling details

3.2.1. Optical diffuser fabrication

Polydimethylsiloxane (PDMS) substrates were made by mixing silicone elastomer with curing agent from a Sylgard 184 kit (Dow Corning) in 10 wt% ratio. The mixture was then degassed in a vacuum desiccator for 30 min and was dispensed and spin-coated on a Polystyrene plate at 200 rpm for 30s. The resulting film (~ 250-300 μm in thickness) was then cured on a hot plate at 80°C for 2h before it was surface-treated with a 20W O_2 plasma at 700 mT for 30s. The plasma treatment is known to increase the PDMS surface hydrophilicity which is essential for nanosphere self-assembly [126], [127]. Due to the temporary nature of the effectiveness of the plasma treatment, the treated films were quickly taken for nanosphere self-assembly process immediately

after the plasma treatment. Because of the hydrophobicity of the Polystyrene plate, the treated PDMS films were easily detachable from the plate and were cut into appropriate sizes before undergoing the nanosphere assembly. Air/water interface self-assembly process [128] was then employed for self-assembly of PS nanospheres of 1μm in diameter (Thermo Scientific) on plasma-treated PDMS substrates. In brief, with the PDMS substrates being inside a glass petri dish, a piece of cleaned 1mm thick glass slide was placed at the edge of the petri dish. DI water was then slowly added to the dish until its surface is at the same level as the upper surface of the glass slide. Numerous droplets of a colloidal water/ethanol suspension (1.5% v/v) were then dropped on the glass slide. It was noticed that the PS nanospheres spread on the water surface as soon as the suspension droplets come into contact with the surrounding DI water at the edges of the glass slide. The process continued until the whole water surface in the petri dish was covered with a monolayer of PS nanospheres. The water in the dish was then slowly sucked out using a micro-pipet until the nanosphere monolayer is settled on the PDMS substrates. Finally, the substrates were left in air for a few hours to be completely dried out.

3.2.2. FDTD simulations

The Lumerical FDTD solutions software was used. All the simulations were performed in a three-dimensional space. A unit cell of the structure was simulated with periodic boundary conditions along the x and y directions, and perfectly matched layer (PML) conditions along the light propagation direction (z). The nanospheres were assumed to sink into PDMS substrate with a depth of 200 nm. A plane wave source was used to launch the light normally incident on the unit cell. Simulation of diffraction efficiencies was carried out using grating projection options of the software and diffraction patterns were obtained using far-field projections. E-field intensities were detected using a frequency-domain field profile monitor located inside the CQD film. Optical constants of the materials were modeled by fitting to the experimental data available in literature [85], [129], [130].

3.2.3. Diffraction efficiency measurement

Diffraction efficiencies were calculated by measuring the specular and total transmission from the sample. For specular transmission, the 3-detector module of a Perkin-Elmer Lambda 1050 UV/Vis/NIR Spectrophotometer was used with the sample aligned with respect to the detector window. A custom-made fixture was used to hold and apply variable stretch to the sample inside the module. Angle dependent diffraction efficiencies were measured using the same setup with the sample being located on a rotating stage. Due to the restrictions of the employed setup, incident angles wider than $\pm 70^{o}$ were not possible to test. In the case of total transmission, the 150 mm integrating sphere module of the spectrophotometer was utilized while the sample was held at the sample beam entrance port of the sphere. All the other ports of the sphere except the reference beam entrance port were kept closed. Transmission spectra for polarized light were obtained by a J. A. Woollam VASE spectroscopic ellipsometer.

3.2.4. Diffraction pattern projections

The monochromatic diffraction patterns of the optical diffuser were projected on a screen with a HeNe laser (Newport) emitting at ~ 633 nm as the light source while the sample was held between the light source and the screen using a custom-made fixture. A CCD camera behind the projection screen was used to capture photographs of the projected patterns. For diffraction patterns of white light, the light from the Xenon lamp of a monochromator (Sciencetech Inc.) was directed toward to sample.

3.2.5. CQD film synthesis and absorption measurement

CQD synthesis and film deposition, and ZnO/TiO_2 film deposition were all carried out according to previously published procedures [82], [131]. After the formation of ZnO/TiO_2 and CQD films on the glass substrate, a 200 nm thick Ag back reflector layer was deposited using e-beam

evaporation (Kurt J. Lesker). For absorption measurement, both optical diffuser and CQD film sample were located at the center of the integrating sphere of a Perkin-Elmer Lambda 1050 UV/Vis/NIR Spectrophotometer using a center mount sample holder. The stretch was applied to the optical diffuser using especially designed holder clips.

3.3. The proposed device structure and properties

The proposed device is composed of self-assembled Polystyrene (PS) nanospheres on a Polydimethylsiloxane (PDMS) substrate. Figure 3-1-a shows the photograph of a sample optical diffuser fabricated using a variation of air/water interface self-assembly process [128]. The purpose of the figure is to demonstrate typical sizes of PS nanosphere domains formed on a PDMS substrate by this method. The sample shown in this figure was coated with gold (Au) for ease of demonstration of the domain sizes through diffuse reflectance from the sample's Au-coated surface. As is clear from the figure, domains with same crystalline structure and orientation exhibit the same reflected color. Using the aforementioned self-assembly process, formation of domains with area of a few millimeter squares was possible. Upon the formation of a PS nanosphere monolayer on the substrate, a strong diffractive behavior is observed from the sample which can easily be attributed to the presence of nanospheres when compared to a bare substrate as illustrated in Figure 3-1-b.

Schematic and SEM image of the structure of the fabricated optical diffuser are depicted in Figure 3-1-c. Hexagonal close-packed assembly of the PS nanospheres onto the PDMS substrate is obvious from the SEM image. The innovative aspect of the fabricated device is that the distance between PS nanospheres can be manipulated by means of mechanical strain applied to the elastomer PDMS substrate. This concept is illustrated in Figure 3-1-d where the schematic and SEM image of the device structure under stretched condition are demonstrated. As can be seen from the SEM image, PS nanospheres can closely follow the direction of the applied strain in their

movement. In addition, a firm bonding between PS nanospheres and PDMS substrate seems to be present which helps the spheres to remain attached to the substrate's surface despite being exposed to heavy mechanical strain for numerous times. We achieved this firm bonding by the O_2 plasma treatment that the substrate undergoes before PS nanosphere self-assembly as it is known that O_2 plasma treatment can establish strong bonding between polymer materials [127]. As shown in figure 3-2, the slight sinking of PS nanospheres into PDMS observed from cross-sectional SEM images can also help retaining their attachment to the substrate.

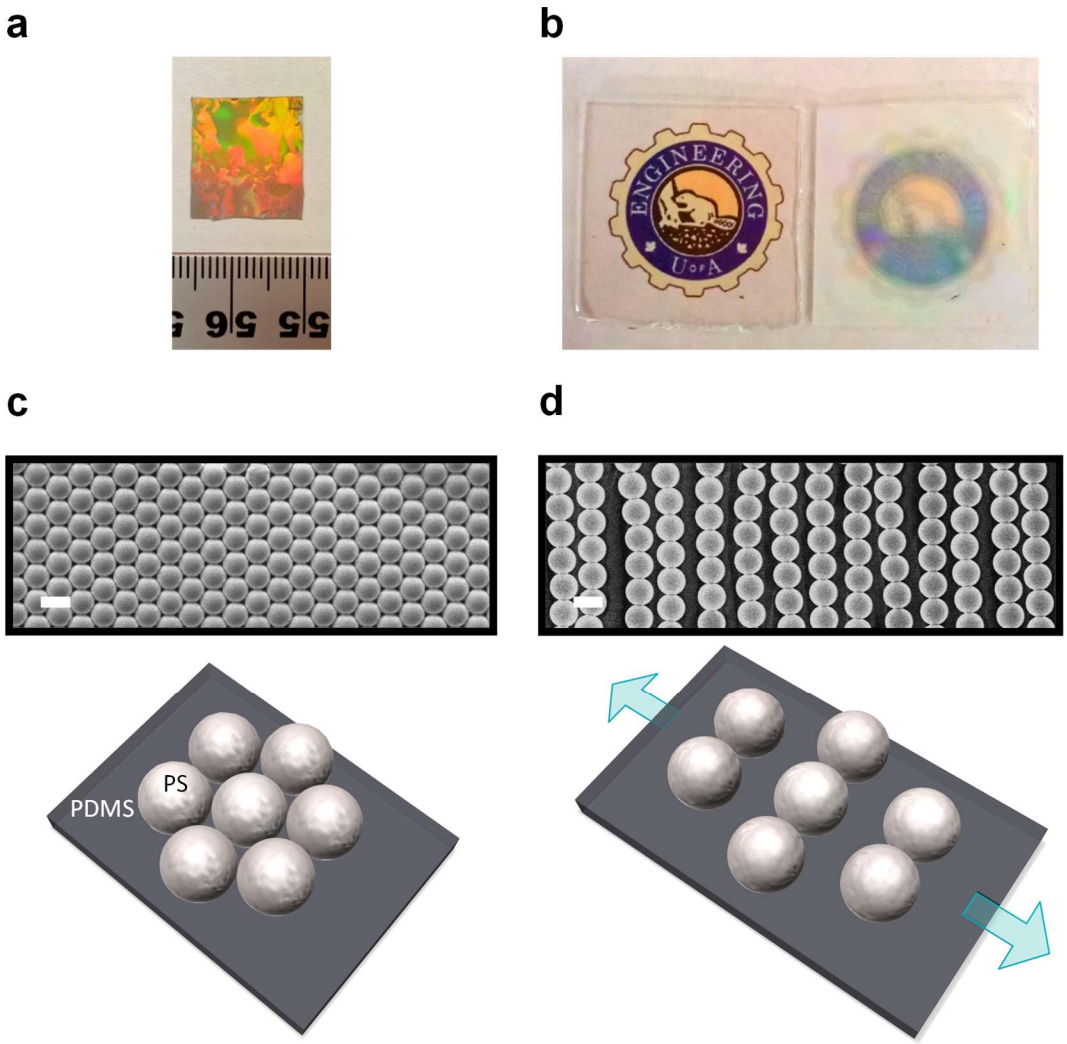

Figure 3-1: Tunable optical diffuser structure and properties. (a) Demonstration of the size of PS nanosphere domains on a PDMS substrate. Domains with same structure exhibit the same reflected color. The sample is coated with gold for ease of demonstration through diffuse reflectance from the sample's surface. (b) Diffusive behavior of a substrate coated with PS nanospheres (right) as opposed to a bare substrate (left). (c,d) Schematic and SEM images of the

structure of the fabricated optical diffuser at unstretched (c) and stretched (d) condition. The distance between PS nanospheres can be manipulated by means of stretching the elastomer PDMS substrate. The scale bar for SEM images is 1 μm. ***Reprinted with permission from [132]. Copyright (2016), Wiley-VCH.***

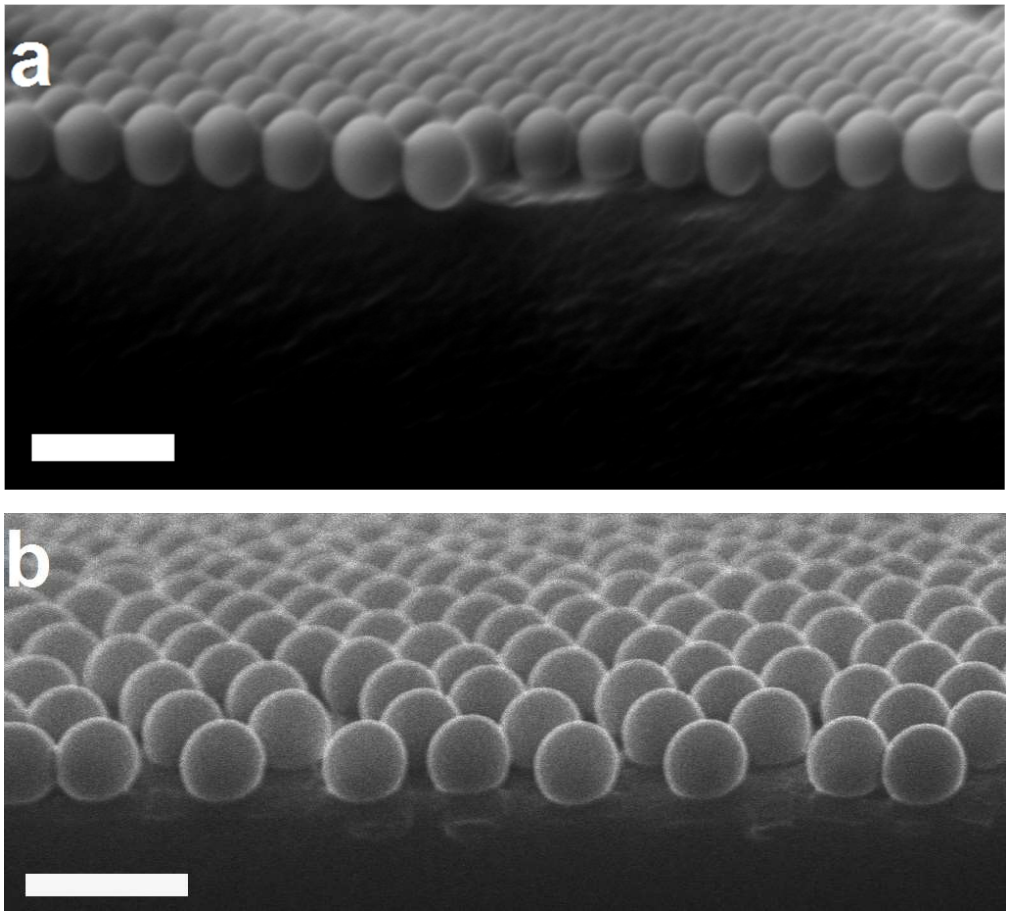

Figure 3-2: Cross-sectional SEM image of a sample fabricated optical diffuser under (a) unstretched and (b) stretched condition. Due to the relative softness of the PDMS, it was found that the PS nanospheres sink into the substrate with an average depth of ~ 200 nm after self-assembly. The scale bars are 2 μm. ***Reprinted with permission from [132]. Copyright (2016), Wiley-VCH.***

3.4. Tunable diffraction efficiency

Because of the hexagonal close-packed structure of a PS nanosphere monolayer and periodic nature of its assembly, the fabricated device can be considered as a hexagonal diffraction grating [122]. The diffraction behavior of the proposed device was therefore analyzed in detail as is shown Figure 3-3. Schematics of the experimental setups used for measuring specular and total transmitted light from fabricated optical diffusers are elucidated in Figure 3-3-a and 3-3-b,

respectively. For specular transmission measurement, a detector located at a significant distance away from the sample was utilized to capture specular transmitted light since any diffuse transmitted light from the device will not get the chance to hit the detector window in this configuration. In the case of total transmitted light, an integrating sphere was employed to capture both specular and diffuse transmitted light from the optical diffuser positioned in front of the integrating sphere.

Figures 3-3-c and 3-3-d depict 3D Finite-Difference Time-Domain (FDTD) simulated and experimentally measured specular and total transmitted light from the proposed optical diffuser under various levels of applied stretch, respectively. For the results obtained from 3D FDTD simulation, a unit cell of PS nanosphere array similar to schematics in Figure 3-1-c and 3-1-d was considered with periodic boundary conditions. As is noticeable from the results, simulation and experiment are in close agreement. The fabricated device exhibits a very broadband diffraction behavior across the measured spectrum and the significant percentages of diffuse transmission (the difference between specular and total transmission) denote the device's high diffraction efficiency throughout both visible and near-infrared regions. Furthermore, the obtained total transmission intensities indicate that the device does not show a remarkable amount of parasitic absorption or reflection, a property which is highly expected from an optical diffuser. This is thanks to the extremely low absorption coefficients and small difference in refractive index of Polystyrene (PS) and PDMS materials forming the device structure. The change in the thickness of the substrate resulting from the applied stretch does not seem to have a significant effect on light diffusion as was noticed from specular transmission spectra of a bare PDMS substrate for different levels of stretch illustrated in figure 3-4. The discrepancy between the total transmission intensities in simulation and that of the experiment may be ascribed to the intrinsic measurement error introduced by the integrating sphere due to its finite area to port fraction leading to a small portion of light escape from its entrance port. More importantly, the device's diffraction

efficiencies are in-situ tunable through the amount of stretch applied to the sample. As is upheld by FDTD simulations, this tunability of the diffraction efficiency is feasible because of the ability to manipulate the distance between PS nanospheres or in other words the pitches of the hexagonal grating along different directions.

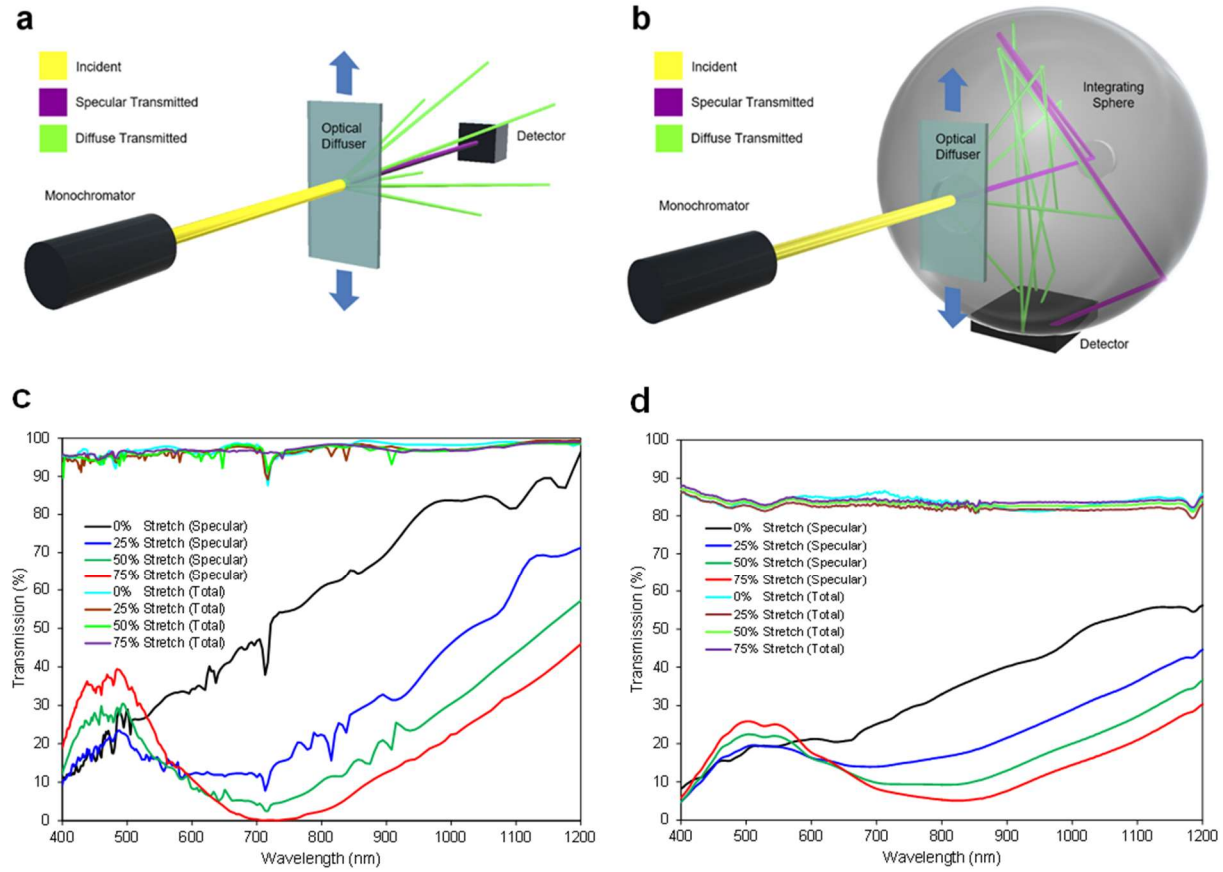

Figure 3-3: Specular and total transmission of the optical diffuser. (a,b) Schematic of the experimental setup used for measuring specular (a) and total (b) transmitted light from fabricated optical diffusers. For specular transmission, a detector at a significant distance from the sample can detect specular transmitted light and for total transmission, an integrating sphere will capture any transmitted light in any direction from a sample located in front of the sphere. (c,d) 3D FDTD simulated (c) and experimentally measured (d) specular and total transmitted light from fabricated optical diffuser at various amounts of stretch. The percentage of diffuse transmittance (the difference between specular and total transmittance) is tunable through the amount of stretch applied to the sample. ***Reprinted with permission from [132]. Copyright (2016), Wiley-VCH.***

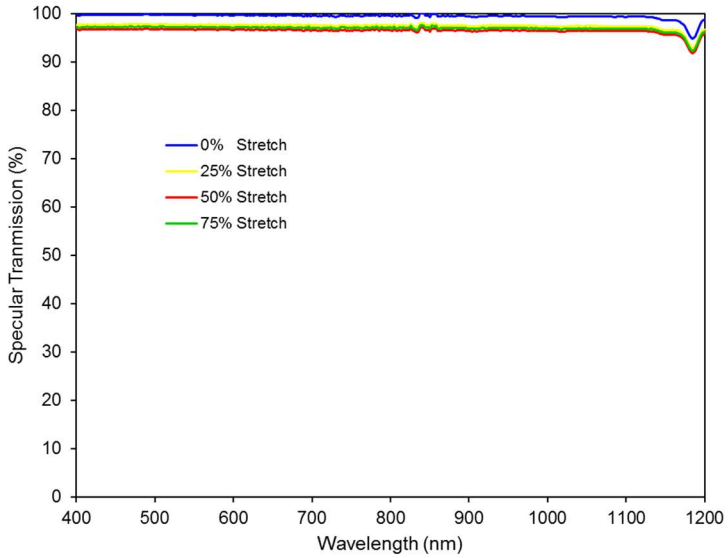

Figure 3-4: Specular transmission spectra of a bare PDMS substrate for different levels of stretch. The change in the thickness of the substrate resulting from the applied stretch does not seem to have a significant effect on light diffusion. ***Reprinted with permission from [132]. Copyright (2016), Wiley-VCH.***

It is highly beneficial to clarify here that the percentages of applied stretch mentioned in this work imply the ratio of the change in sample's length under stretch to its original length. It was noticed however that the amount of displacement of the PS nanospheres does not always exactly follow the amount of change in substrate's length. This can be held responsible for the small difference between simulated and measured specular transmission intensities since in simulation it was always assumed that the sphere displacement percentage is exactly same as the substrate's length change. Also, high intensity sharp changes in transmission spectra from the simulated results could be attributed to resonant peaks usually observed in periodic structures with perfect lattice. As for the experimental results, the lattice disorders stemming from the exposure of nanosphere arrays to multi-directional mechanical stress during sample stretch leads to the broadening and disappearance of the aforementioned resonant peaks. A similar trend has been noticed in intentionally disordered photonic crystals [133]. This can be further confirmed by investigating the specular transmission spectra from a PS nanosphere-coated glass substrate as depicted in figure 3-5. With some resonant peaks being visible, the obtained spectra was found to be closer to the simulation result for specular transmission of an unstretched optical diffuser. This is possibly

due to the fact that nanospheres' domain structure remains intact after fabrication on a rigid substrate as opposed to a flexible substrate which can introduce physical defects and thus disorders to the lattice structure. On the other hand, small fluctuations in simulated spectra can be attributed to numerical errors stemming from inadequately small mesh size for FDTD simulation due to our limited available processing power.

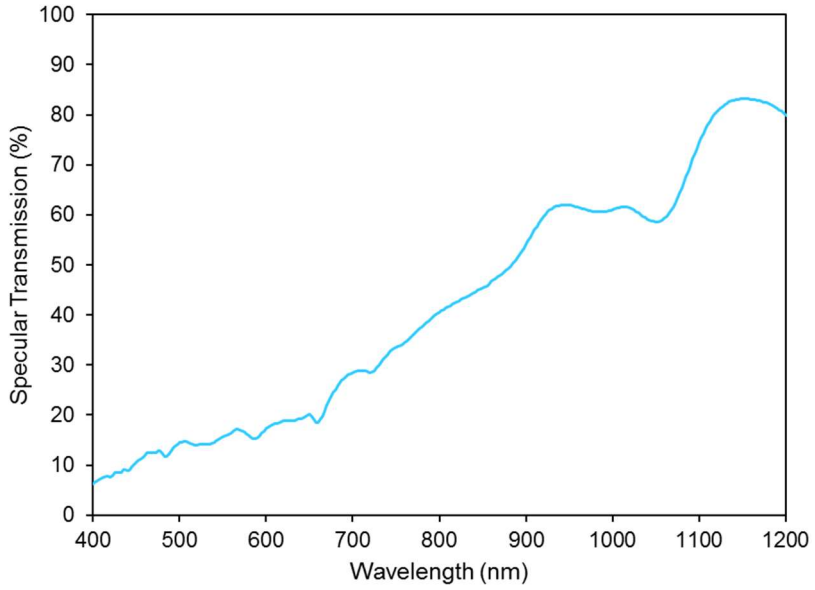

Figure 3-5: Experimentally measured specular transmission from a PS nanosphere-coated glass substrate. The obtained spectra is closer to the simulation result for specular transmission of an unstretched optical diffuser possibly due to the fact that nanospheres' domain structure remains intact after fabrication on a rigid substrate as opposed to a flexible substrate which can introduce physical defects to the pattern structure. ***Reprinted with permission from [132]. Copyright (2016), Wiley-VCH.***

The dependence of the optical diffuser's performance on incident light polarization and angle was also analyzed. As shown in Figure 3-6-a, specular transmission spectra of the optical diffuser at various levels of stretch for s- and p-polarized light reveals no significant dependence on incident light's polarization possibly due to the multi-directional symmetry of the proposed structure. The diffraction efficiency of the optical diffuser as a function of the incident light angle with respect to substrate normal depicted in Figure 3-6-b indicates the relative independency of the performance of the device from incident light angle. In addition, repeatability of the device performance was

examined by measuring the specular transmission from a fabricated optical diffuser at various levels of stretch after certain numbers of stretch-release cycle repetition and is shown in figure 3-7. The device was perceived to offer good reliability for its light diffusion performance. The obtained results imply the high reliability of the performance of the proposed device under a wide variety of conditions.

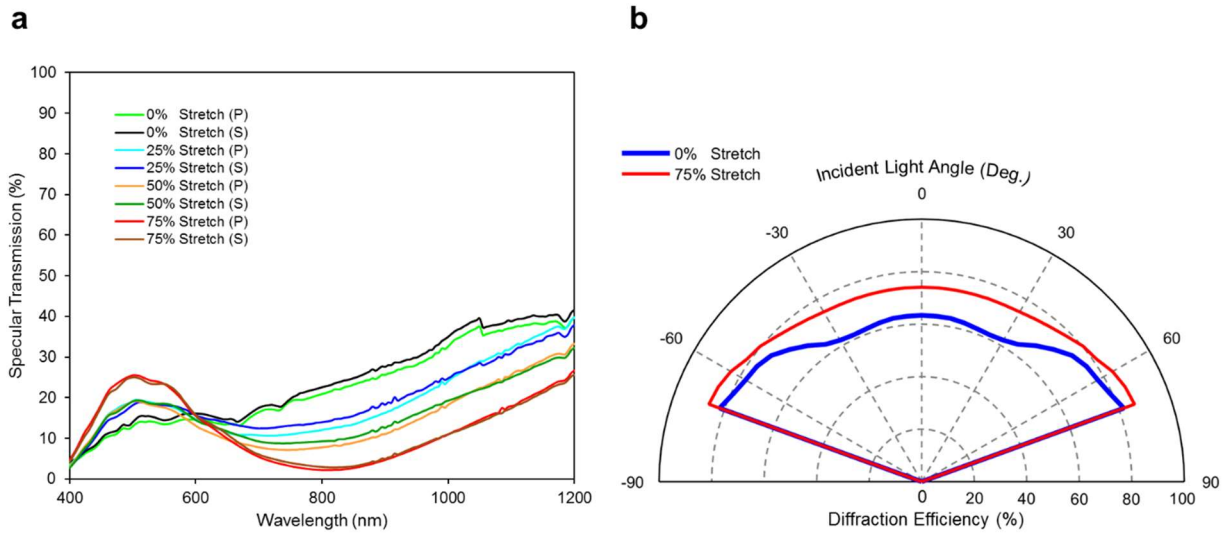

Figure 3-6: The dependence of the optical diffuser's performance on incident light polarization and angle. (a) Specular transmission spectra of the optical diffuser at various levels of stretch for s- and p-polarized light. (b) Diffraction efficiency of the optical diffuser as a function of the incident light angle with respect to substrate normal for unstretched and stretched samples. The performance is almost independent of the incident light's polarization and angle. ***Reprinted with permission from [132]. Copyright (2016), Wiley-VCH.***

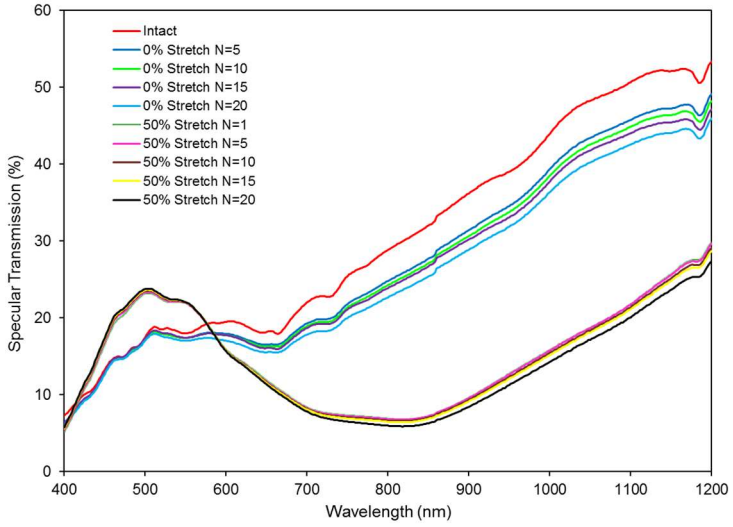

Figure 3-7: Specular transmission measured from a fabricated optical diffuser at various levels of stretch after certain numbers of stretch repetition. N indicates the number of times the sample has gone through a cycle of stretch and release before the measurement is taken. A sample that has not been subject to any stretch after fabrication is depicted as "Intact". 0% describes the state of release after a stretch tension. Although the sample does not show the same characteristics as before the first time it is exposed to mechanical stress (intact condition), repeatability of light diffusion performance after first stress seems to be reliable with small variations. ***Reprinted with permission from [132]. Copyright (2016), Wiley-VCH.***

3.5. Diffraction Pattern Analysis

3.5.1. Experimental analysis

As was mentioned before, the proposed optical diffuser can be considered as a hexagonal diffraction grating. Since it is known that hexagonal gratings tend to produce diffraction patterns of hexagonal origin [122], a detailed analysis of the diffraction patterns generated by the fabricated optical diffuser can be of great importance. Figure 3-8-a illustrates the schematic of the experimental setup utilized for diffraction pattern analysis. The sample is located between a HeNe laser emitting at the wavelength of about 633 nm and a projection screen. A custom-designed fixture was used for stretching the sample. Diffraction patterns resulting from the aforementioned setup for unstretched, 25% stretched, and 75% stretched samples are shown in Figure 3-8-b-d, respectively. The corresponding patterns obtained by 3D FDTD simulation are depicted in Figure 3-8-e-g.

From the obtained diffraction patterns of hexagonal origin, it can be concluded that the fabricated device consists of hexagonal diffraction gratings. Moreover, a good accordance between the patterns acquired from simulation and those of experiment is remarkable. However, some discrepancy was noticed at high levels of stretch which may be attributed to the difficulty of keeping the strain applied to PS nanosphere arrays to remain one-dimensional under highly stretched conditions due to the 2D deformation of the PDMS substrate under strong stretch. This is why the simulated pattern in Figure 3-8-g is obtained by a slight stretch application in the x

direction in addition to 75% stretch in y direction which makes the obtained pattern more close to the experiment. Nevertheless, the observed changes in diffraction patterns at various levels of stretch further endorse the in-situ tunability of diffraction properties of the proposed device. In addition, relative values of energy distribution into different orders calculated by FDTD simulation were found to be in excellent agreement with diffraction efficiencies shown in Figure 3-3. For example, as demonstrated in figure 3-9, for light with the wavelength of 633 nm, simulated diffraction patterns indicated that only about 20% of the incident energy is distributed into the zeroth order and the rest is diffracted into higher orders. This is an additional evidence for the accuracy of the diffraction efficiencies obtained in Figure 3-3.

It has been previously argued that any general hexagonal diffraction grating can be considered as it is composed of three two-dimensional diffraction gratings with different periods along the x and y directions [122] (also known as crossed or doubly periodic gratings). While it is possible to analyze the proposed device with this approach (see section 3.5.2 for details), we were able to simplify the analysis by basic geometric calculations on the obtained diffraction patterns. In this technique, as illustrated in Figure 3-8-a, the diffraction angle of the diffracted orders (θ) was calculated from measuring the distance between the corresponding diffracted pattern and the pattern's center (Δx), and the distance between the projection screen and the sample (Δl) using the following equation:

$$\theta = tan^{-1}(\frac{\Delta x}{\Delta l}) \tag{3-1}$$

The calculated diffraction angles with this approach were found to be in close agreement with the angles obtained from simulated diffraction patterns. Moreover, in the case of the unstretched optical diffuser, the cut-off wavelength (the wavelength beyond which there will be no diffracted orders and all the incident energy is distributed into the zeroth order) was noticed to be in

accordance with the calculated value (~ 1250 nm) for a simple hexagonal grating as provided in the following equation for normal light incidence [134]:

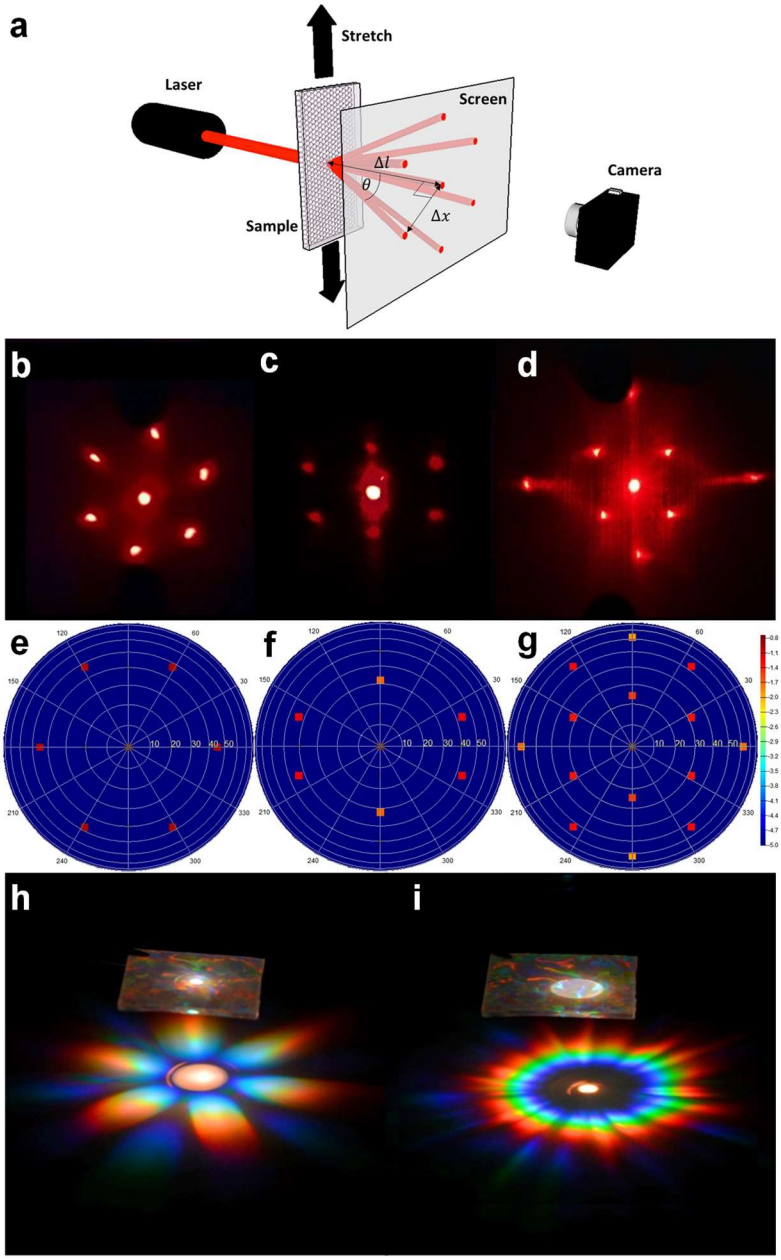

Figure 3-8: Diffraction pattern analysis of the optical diffuser. (a) Schematic of the experimental setup utilized for diffraction pattern analysis. The sample is located between a HeNe laser emitting at ~ 633 nm and a projection screen. A custom-designed fixture was used for stretching the sample. (b-g) Experimental (b-d) and simulated (e-g) diffraction patterns obtained from an unstretched (b,e), 25% stretched (c,f) and 75% stretched (d,g) optical diffuser. Simulated pattern intensities are shown in logarithmic scale for ease of demonstration. The diffraction angle for each diffracted order can be inferred from its pattern position on corresponding concentric circles with the zeroth order being located at the center. Figure g is obtained by a slight stretch application in the x direction in addition to 75%

stretch in y direction in order to resemble the experiment situation. (h,i) Diffraction of white light by fabricated optical diffuser when the light is incident on a single nanosphere domain (h) or multiple domains at the same time (i). In case the light hits a single domain, a diffraction pattern of hexagonal origin is expected and when the light is incident on multiple domains, the sample still demonstrates diffractive behavior, but patterns from all the domains are combined together, resulting in a ring-shaped diffraction pattern. ***Reprinted with permission from [132]. Copyright (2016), Wiley-VCH.***

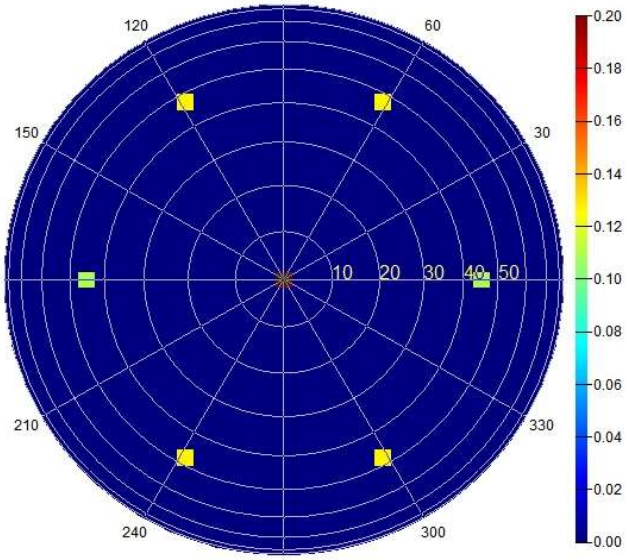

Figure 3-9: Simulated diffraction pattern intensities from the unstretched optical diffuser at the light wavelength of 633 nm. The color bar indicates the relative energy intensity value for diffracted orders out of total energy level of 1. Only about 20% of the incident energy is distributed into the zeroth order (the dot at the center) and the rest of energy is diffracted into the first order with diffraction angle of 47 degrees. ***Reprinted with permission from [132]. Copyright (2016), Wiley-VCH.***

$$\lambda_c = \frac{n\Lambda}{f_g} \tag{3-2}$$

Where λ_c is the cut-off wavelength, n describes the refractive index of the substrate, Λ depicts the grating period, and f_g is the grating geometrical factor which is equal to 1.155 for a hexagonal grating [134]. Obviously, under stretched conditions, the cut-off wavelength can be further shifted towards infrared since the grating period has been increased due to the applied mechanical strain.

Figure 3-8-h and 3-8-i show diffraction patterns of white light produced by the fabricated optical diffuser when the light is incident on a single nanosphere domain or multiple domains at the same

time, respectively. In case the beam size of incident light is small such that it only hits a single domain, a diffraction pattern of hexagonal origin is generated and when the beam size is larger and thus it is incident on multiple domains, the sample still demonstrates diffractive behavior, but patterns from all the domains are combined together, resulting in a ring-shaped diffraction pattern due to different orientation of each domain. This implies that non-idealities in the structure of the device will not result in the loss of its diffractive function.

All in all, the detailed analysis of the diffraction patterns suggests that the reason behind the tunability of the diffraction behavior of the proposed device lies in the fact that as the device is stretched, due to the change in grating periods along the stretch direction, the diffraction angles, the energy distribution among different diffracted orders, and even the number of supported diffraction orders can be changed, which can greatly broaden the application range of the device.

3.5.2. Theoretical analysis

As is shown in Figure 3-10, a hexagonal grating can be decomposed into three two-dimensional gratings and these three components of the hexagonal grating have different periods along the x and y directions [122]. For an arbitrary orientation of the PS nanosphere array, the periods of the grating components along the x and y directions can be calculated using the following relations [122]:

$$P_{xn} = \frac{d}{\left|\cos\left(\alpha-(n-3)\frac{\pi}{3}\right)\right|} \quad n = 1,2,3 \tag{3-3}$$

$$P_{yn} = \frac{d}{\left|\sin\left(\alpha-(n-3)\frac{\pi}{3}\right)\right|} \quad n = 1,2,3 \tag{3-4}$$

Where n is the number of the grating component, α is the orientation angle of the array with respect to the y axis and d is the pitch of hexagonal grating. For the special case when the array is

oriented such that $\alpha = 0$ and the grating pitch, which here is equal to spheres diameter, is 1 μm, the following values can be obtained for grating components periods:

$$P_{x1} = P_{x2} = \sqrt{3} \quad P_{x3} = \frac{\sqrt{3}}{2} \quad P_{y1} = P_{y2} = 1 \quad P_{y3} = \infty \tag{3-5}$$

All values are in μm. A value of infinity for a period means that the structure is not periodic in the corresponding direction, which is obvious for the special case under study.

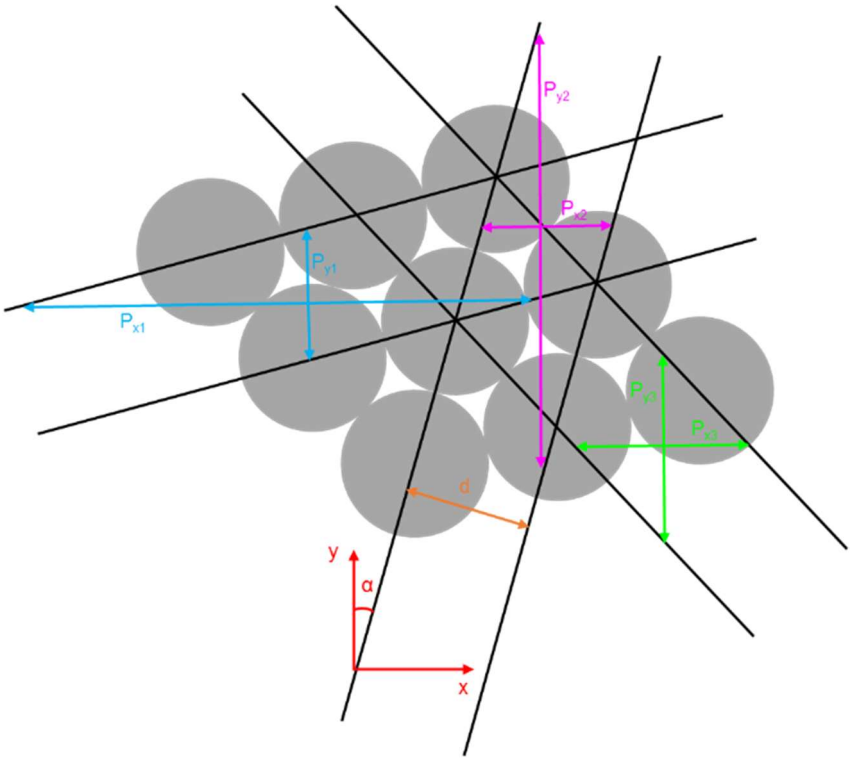

Figure 3-10: Generalization of the analysis of the structure of a hexagonal grating. The hexagonal grating can be decomposed into three two-dimensional gratings with different periods along the x and y directions. ***Reprinted with permission from [132]. Copyright (2016), Wiley-VCH.***

Using the classic grating equation for 1D gratings, supported orders for each grating component along the x and y directions and their corresponding diffraction angles can be calculated as follows. The grating equation for normal incidence is provided below:

$$m\lambda = nP\ sin\theta \tag{3-6}$$

Where m is the supported diffraction order number, λ is the incident light wavelength, n is the refractive index of the medium into which the diffracted orders travel, P is the grating period, and θ is the diffraction angle of the m^{th} diffracted order. For instance, by replacing the above obtained grating components periods in the grating equation, for the light wavelength of 633 nm and refractive index of air (n=1), the diffraction angles of the supported orders along the x and y direction can be obtained as follows:

$$m = 1 \quad \theta_{x1} = \theta_{x2} \cong \mp 35^o \ \ \theta_{x3} \cong \mp 47^o \ \ \theta_{y1} = \theta_{y2} \cong \mp 39^o \ \ \theta_{y3} = 0 \tag{3-7}$$

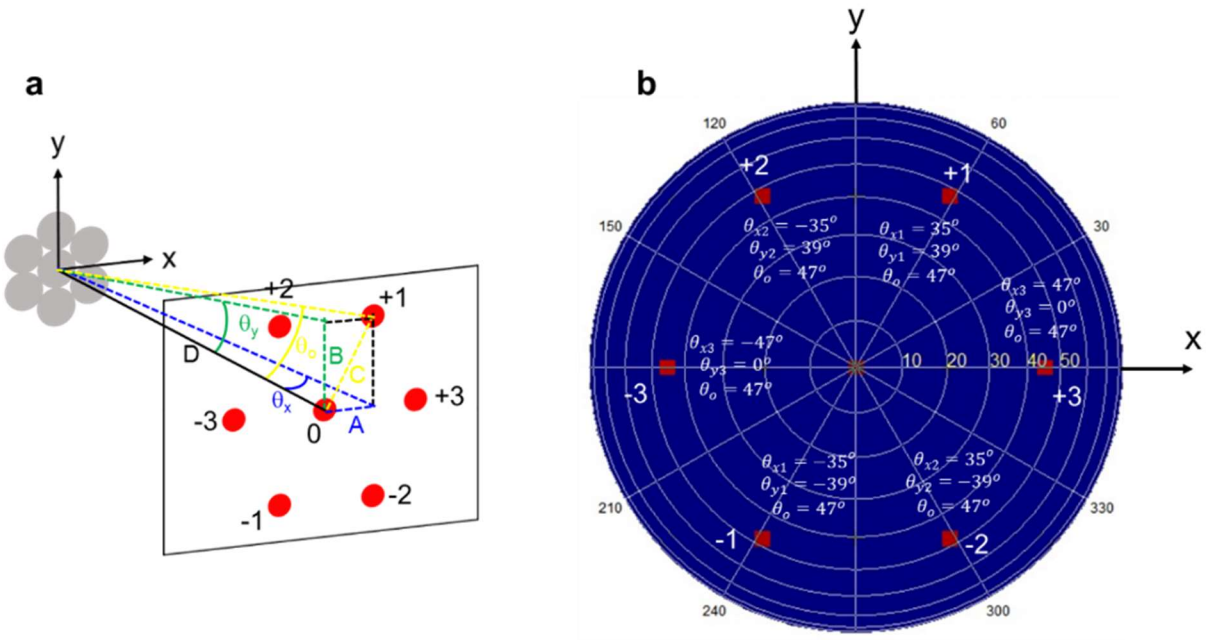

Figure 3-11: Analytical projection of the diffraction pattern of a hexagonal grating. (a) Demonstration of geometrical parameters used to predict the diffraction pattern from a hexagonal nanosphere array. (b) Comparison of the calculated diffraction angles for the diffraction pattern and those obtained from simulation. ***Reprinted with permission from [132]. Copyright (2016), Wiley-VCH.***

Where θ_{xn} and θ_{yn}, as defined in Figure 3-11-a, indicate the diffraction angle of the n^{th} grating component along the x and y directions, respectively. In this case, no second order is supported

by the grating structure. As θ_x and θ_y represent the diffraction along the x and y directions, the diffraction pattern resulting from each grating component can be easily predicted by the values obtained for these angles. As illustrated in Figure 3-11-a, the diffraction angle for each pattern (θ_o) can be obtained using simple geometrical calculations. For example, for the point labeled "+1", which indicates a pattern created by the first grating component in positive direction, the diffraction angle (θ_o) can be calculated from the above obtained θ_x and θ_y values for this point:

$$tan\theta_x = \frac{A}{D} \rightarrow A = 0.7D \quad tan\theta_y = \frac{B}{D} \rightarrow B = 0.81D \tag{3-8}$$

$$C = \sqrt{A^2 + C^2} = 1.07D \tag{3-9}$$

$$tan\theta_o = \frac{C}{D} = 1.07 \rightarrow \theta_o \cong 47^o \tag{3-10}$$

As shown in Figure 3-11-b, the obtained value for θ_o closely matches the one obtained from simulation which can be implied from the point's position with respect to the concentric circles. A similar procedure can be followed to acquire the diffraction angles for other parts of the diffraction pattern which are already shown in Figure 3-11-b. In addition, the same approach can be applied to any other structure of hexagonal grating with different orientation and/or grating pitch to analytically predict its diffraction pattern. For a highly stretched structure, for example, additional dots will be added to the diffraction pattern because of the support for higher diffracted orders which is due to the increase in grating components periods along the stretch direction.

3.6. Photon Management for Absorption Enhancement in Colloidal Quantum Dot (CQD) Thin-films

As it is known that dielectric nanospheres can enhance light absorption in thin-film solar cells [135], one potential application of the proposed tunable optical diffuser can be the enhancement of light absorption in light-absorbing layer of thin-film solar cells and photodetectors through its

adjustable diffractive properties. The optical diffuser can cover the front surface of any previously fabricated device to add photon management capability to it. Furthermore, the light management performance and thus absorption enhancement could be tunable across a wide range of light wavelengths due to the unique properties of the proposed optical diffuser. In order to conceptually examine this potential application, the optical diffuser was utilized to improve light absorption in thin-films of PbS CQDs. CQD-based devices can be considered a great candidate to pair up with our proposed device because of their critical need for photon management in near-infrared region where they suffer from low absorption coefficients and also their absorption spectra tunability via the quantum size effect [24] which demands a similarly tunable photon management solution.

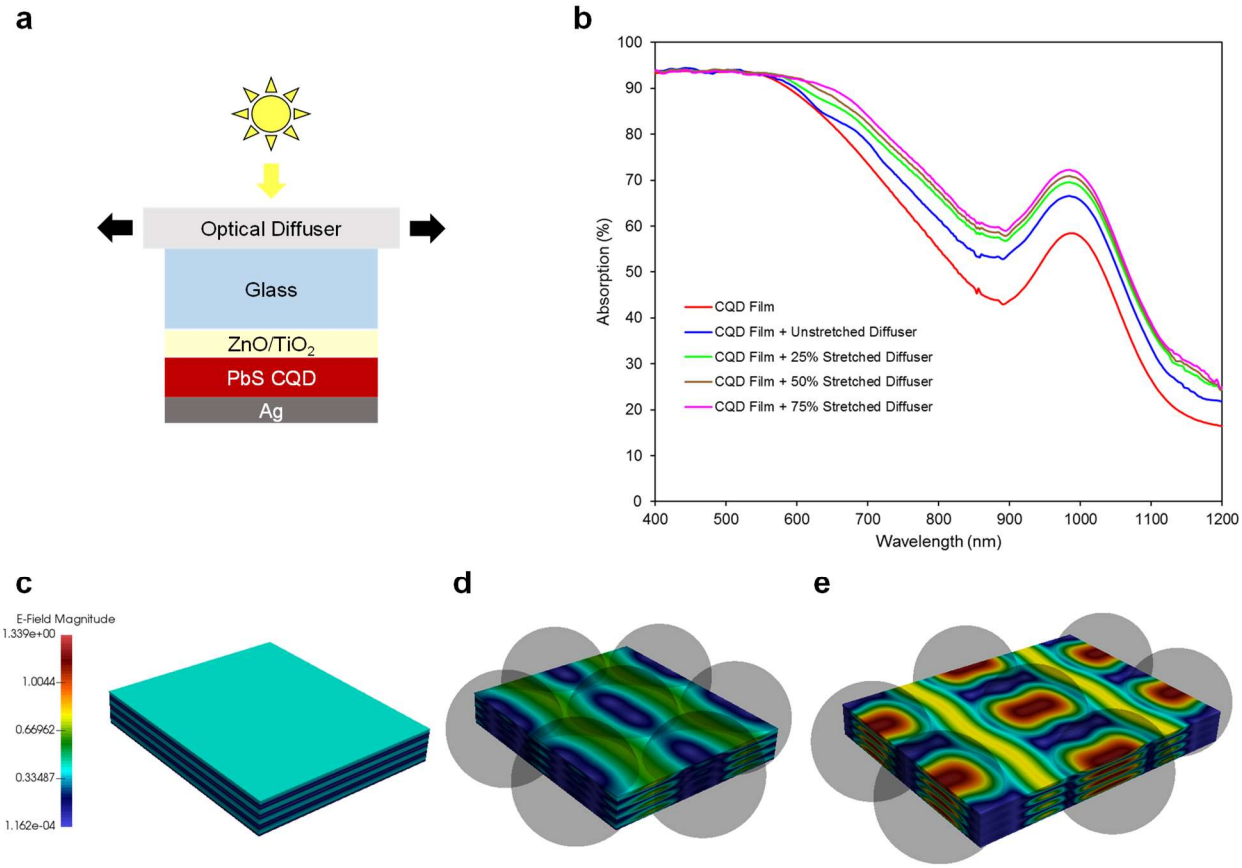

Figure 3-12: Absorption enhancement in CQD films using optical diffuser. (a) Schematic of the sample structure used for absorption measurement in CQD films. The sample was intended to roughly mimic the structure of a depleted heterojunction CQD solar cell. (b) Experimentally measured absorption in CQD films under different conditions. An optical diffuser can significantly enhance light absorption in a CQD film and the amount of absorption in tunable through optical diffuser stretch. (c-e) FDTD simulated E-field intensities at 850 nm wavelength inside a 300 nm thick

CQD film (c) and same film under the influence of a unit cell of unstretched (d) and stretched (e) optical diffuser. Colors represent the relative magnitude of E-field. An optical diffuser can greatly boost E-field intensities inside a CQD film and the intensities can be further enhanced under stretched condition. The schematic does not represent the actual vertical position of the nanosphere array with respect to the CQD film. A shadow of the nanosphere array is present for ease of demonstration. ***Reprinted with permission from [132]. Copyright (2016), Wiley-VCH.***

Figure 3-12-a shows the schematic of the sample structure used for absorption measurement in CQD films. The sample was intended to roughly mimic the structure of a basic depleted heterojunction CQD device [82]. As is clear from the figure, CQDs and a mixed layer of ZnO/TiO_2 nanoparticles form the heterojunction while a layer of silver acts as the back reflector to reflect back any unabsorbed light passing through the CQD film. No FTO layer was implemented inside the sample structure in an effort to eliminate the possible error in measurement due to the parasitic absorption caused by this layer. The optical diffuser is placed on top of the glass substrate to diffusely transmit the incident light into the sample. The experimentally measured absorption spectra in CQD films under different conditions are plotted in Figure 3-12-b. The results reveal that an optical diffuser can significantly enhance light absorption in a CQD film and the amount of absorption is tunable through the level of applied stretch. This is due to the fact that the diffusive behavior of the optical diffuser leads to the increase in the light path length inside the thin-film which in turn increases the chance of light absorption. The absorption enhancement mostly occurs in near-infrared part of the spectrum since the absorption coefficients of CQDs are large enough in visible region such that almost all the incident light is absorbed even if no light management strategy is employed.

The optical diffuser capability to enhance light absorption in CQD films was further affirmed by 3D FDTD simulation. Simulated E-field intensities at 850 nm wavelength inside a 300 nm thick CQD film and same film under the influence of a unit cell of unstretched and stretched optical diffuser are shown in Figure 3-12-c-e, respectively. From the figure, it is obvious that an optical diffuser can greatly boost E-field intensities inside a CQD film and the intensities can be further enhanced under stretched condition. Moreover, the proposed optical diffuser was also tested for

absorption enhancement in crystalline Silicon. As depicted in figure 3-13, comparison of the absorption spectra of a 500 μm thick Silicon slab with and without an optical diffuser disclosed that the optical diffuser is able to greatly enhance light absorption in the silicon slab showcasing the wide spread application of the proposed optical diffuser for devices with different materials and technologies.

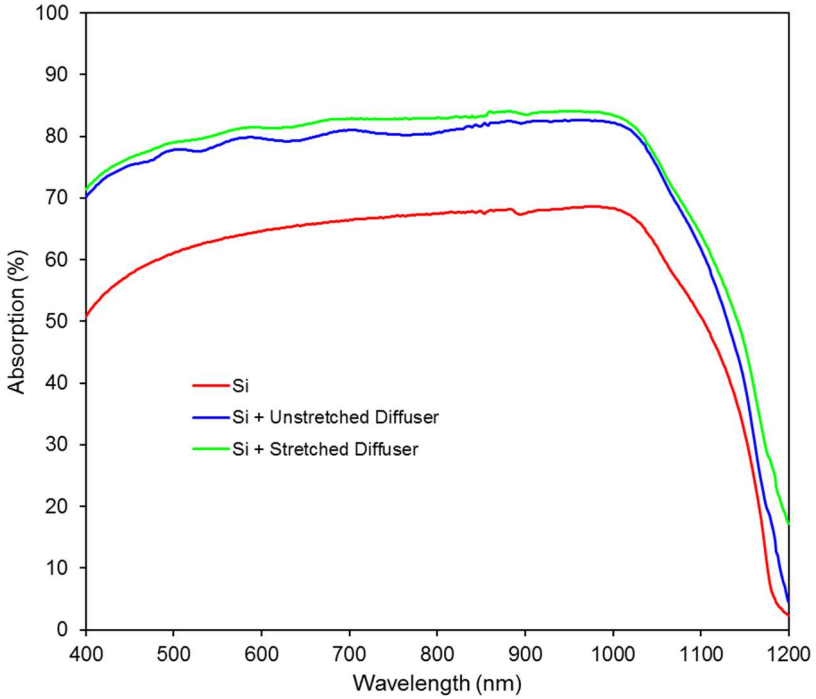

Figure 3-13: Absorption spectra of a 500 μm thick Silicon slab with and without an optical diffuser. The optical diffuser is able to greatly enhance light absorption in the silicon slab showcasing the wide spread application of the proposed optical diffuser for different light absorbing materials and photovoltaic technologies. However, due to the extreme thickness of the slab, which ideally should absorb all the incident light above the Si bandgap, we believe the optical diffuser here is functioning as an anti-reflection coating, reducing the reflection from Si surface thus enhancing light absorption. ***Reprinted with permission from [132]. Copyright (2016), Wiley-VCH.***

3.7. Conclusion

In summary, a novel type of diffraction grating referred to as 'stretchable hexagonal diffraction grating' was introduced in this work and its potential as an optical diffuser for photon management in thin-film optoelectronic devices was explored. The easily fabricated grating's

structure is based on hexagonal arrays of PS nanospheres formed on elastomer PDMS substrate. The proposed device was shown to be widely tunable in terms of the diffraction angles, the number of supported orders, and the energy distribution into higher diffracted orders, thanks to the flexibility of its structure. As an application example, the stretchable hexagonal grating was demonstrated both numerically and experimentally to be able to offer broadband tunable light absorption enhancement in colloidal quantum dot (CQD) thin-films.

In addition to physical flexibility, the stretchable hexagonal diffraction grating concept illustrated here offers lots of degrees of freedom in its structure design. A variety of different nanosphere sizes can be chosen, and even their size can be fine-tuned with nanometer accuracy by reactive ion etching (RIE) processes which provides endless possibilities for adjusting the diffractive properties of the device. Moreover, optimizing the mechanical properties of the PDMS substrate for smaller elasticity modulus [136] is expected to enhance the device's diffusive capability due to the possibility of higher stretch application which can provide support for additional diffracted orders. Better engineering of the nanosphere self-assembly for larger area of perfectly patterned domains [137], [138] may also lead to performance enhancement for the proposed optical diffuser. The novel optical diffuser proposed in this work is easily usable for any previously fabricated optoelectronic device, without the cumbersomeness of modifying the device's structure or fabrication process.

4

Optoelectronic engineering of colloidal quantum-dot solar cells beyond the efficiency black hole: a modeling approach

4.1. Introduction

Persistently growing demand for energy across the globe has increased the importance of photovoltaic technology as a green alternative to traditional energy resources. Reduction in production cost of photovoltaic devices has been the main motivation behind the development of emerging thin-film solar cell technologies [24], [32], [33], [139] despite the current dominance of their silicon-based counterparts in the market.

In order to take the place of silicon-based photovoltaics, thin-film solar cells need a significant boost in their efficiency to fill the gap in efficiency to production cost ratio that currently exists between these two technologies. In this regard, light management techniques are considered one viable engineering approach to overcome the so-called light absorption-charge extraction trade-

off in the design of their active layer thickness which emerging thin-film solar cells suffer from and is the main culprit behind their lackluster efficiency [36]. The basic concept of light management is that by manipulating the path that light travels inside the cell's structure, the chance for light absorption inside the active layer (light absorbing layer) will be increased without any change in the active layer's thickness which, as a result, will not compromise the charge extraction efficiency [36]. The importance of light management in thin-film photovoltaics turns out to be bolder for longer wavelength photons with longer absorption length and photon energies near the bandgap of the absorbing material due to the huge mismatch between the absorption length and the cell's active layer thickness which is severely confined by charge carriers' diffusion length inside the light absorbing material.

The aforementioned trade-off in active layer's thickness also applies to colloidal quantum dot (CQD) solar cells, an emerging type of photovoltaic technology which has demonstrated the potential for low-cost solution-processed fabrication and efficient light harvesting through multiple exciton generation (MEG) and tunable absorption spectrum via the quantum size effect [24]. Although since their emergence impressive advances have been achieved in charge transport properties of quantum dot solids and CQD cells' light trapping capabilities [38]-[41], [83], [140]-[142], the recent progress in CQD solar cell efficiencies has been very sluggish, making them less competitive in comparison to other solar cell technologies.

Especially, light management strategies exploited for CQD solar cells have not been significantly effective in uplifting their performance [38]-[41], [83], leaving the community dubious about the necessity of light management in CQD-based solar cells as a long-term reasonable approach to their competitiveness enhancement in the market. Here, using comprehensive optoelectronic modeling and simulation of CQD solar cells, we pursue a possible sensible reasoning behind their lackluster progress in performance, offering a clear roadmap for CQD solar cell research

community in order to achieve the milestones required for commercialization of the CQD-based photovoltaic technology.

4.2. Modeling and simulation methods

4.2.1. Device structure

Figure 4-1 shows the schematic of the device structure used for optoelectronic simulation of CQD solar cells. The chosen structure was intended to model the structure of a typical depleted heterojunction CQD solar cell based on PbS quantum dots [82]. In a typical depleted heterojunction CQD solar cell, a thin layer of TiO_2 or ZnO which is optically transparent in the operating range of the cell serves as the n-side of the junction and the CQD layer plays a double role of being the p- side of the junction and also the light absorbing layer. Gold (Au) can be used to establish an ohmic contact to CQD layer as the back contact to extract photo-generated holes. In addition, being highly reflective, gold doubles the optical pathway of photons inside the CQD layer, improving the overall light absorption of the device. Glass is being used as the substrate and a layer of transparent conductive oxide (Indium-doped tin oxide, ITO) on the substrate forms the front contact to the junction.

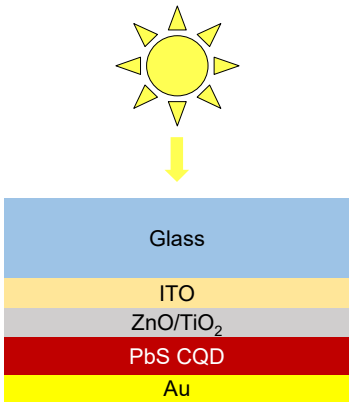

Figure 4-1: Schematic of the device structure used for optoelectronic simulation of PbS CQD solar cells. The structure is intended to mimic the structure of a typical depleted heterojunction CQD solar cell. ***Reprinted with permission from [143]. Copyright (2017), Society of Photo-Optical Instrumentation Engineers.***

4.2.2. Optoelectronic modeling and simulation

The AM1.5G solar spectrum was used for all the simulations. The transfer matrix optical modeling developed for thin-film solar cells [144] was utilized and performed in MATLAB to obtain the carrier generation rate profile inside the CQD film of the solar cell. The real part of refractive index (n) of PbS CQDs was estimated from that of bulk PbS based on a 75% volume fraction of PbS CQD films compared to bulk PbS [144] as it is known that n has a linear relationship with volume fraction [145]. This approximation is justified since the transfer matrix method is not sensitive to the accuracy of n values of the materials for the purpose of absorption measurement in the active layer [144]. This statement was confirmed by observing the effect of perturbations in n values on calculated absorption in active layer. On the other hand, as the accuracy of the imaginary part of refractive index (k) is crucial for transfer matrix modeling, the k values for PbS CQD films were obtained from experimentally measured absorption coefficient (α) of the films, as plotted in figure 4-2, using the following formulation [132]:

$$k = \frac{\alpha\lambda}{4\pi} \tag{4-1}$$

Where λ is the wavelength at which the absorption coefficient has been measured. For measuring the absorption coefficient, CQD film samples were mounted at the center of the integrating sphere of a Perkin-Elmer Lambda 1050 UV/Vis/NIR Spectrophotometer using a center mount sample holder. This setup was used to measure the optical density (OD) of the CQD film, from which the absorption coefficient (α) of the film was calculated using the following equation after measuring the film's thickness (d) by a KLA Tencor Alpha-Step iQ contact profilometer:

$$\alpha = OD \times \frac{\ln(10)}{d} \tag{4-2}$$

Other required optical constants of materials for modeling were taken from the literature [84]-[87]. The generation rate profile obtained from optical modeling was imported into Lumerical

DEVICE software for electrical simulation. A full list of material parameters used for device physics modeling is provided in Table 4-1. Contacts boundary conditions were forced to be ohmic. Trap states were considered to be single level at 0.2 eV below the conduction band [35]. External quantum efficiencies (EQEs) were calculated from the output current of the cell under short-circuit condition at each wavelength using the following expression:

$$EQE(\lambda) = \frac{hc}{q\lambda} \times \frac{J_{SC}(\lambda)}{P_{AM1.5G}} \tag{4-3}$$

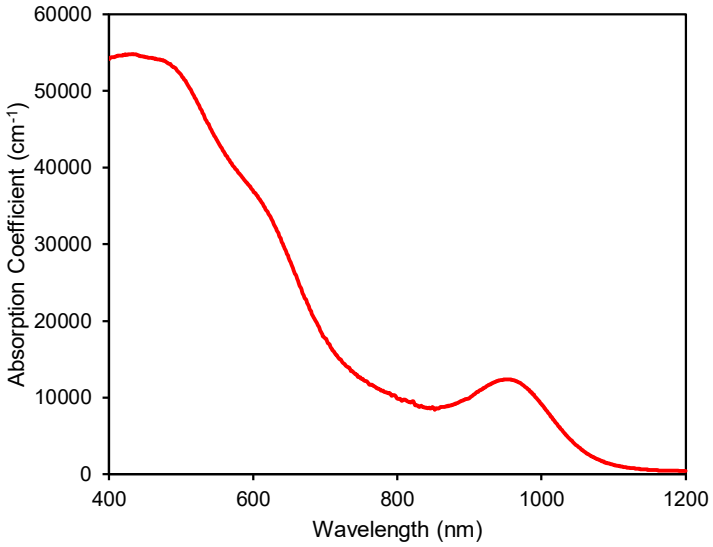

Figure 4-2: The measured absorption coefficient of PbS colloidal quantum dots used for optoelectronic modeling and simulation. ***Reprinted with permission from [143]. Copyright (2017), Society of Photo-Optical Instrumentation Engineers.***

Where λ is the wavelength at which the measurement has been done, h denotes the Planck's constant, c indicates the speed of light in vacuum, q is the electron electric charge, J_{SC} implies the short-circuit current and $P_{AM1.5G}$ denotes the incident power from AM1.5G solar spectrum. Diffusion lengths inside the CQD film were tuned by adjusting the mobility and carrier life times of the model. Light path length enhancement was modeled by uniform increment in effective absorption coefficient ($\alpha_{effective}$) of CQD films across the whole spectrum in optical modeling (absorption enhancement ratio= $\alpha_{effective}$ / $\alpha_{intrinsic}$) as it is believed that light path length

enhancement caused by a diffusive surface is directly equivalent to the per-pass absorption enhancement [146].

Table 4-1: Materials parameters used for a typical optoelectronic simulation of a depleted heterojunction CQD solar cell. Superscripts indicate the references from which the parameter values are taken. ***Reprinted with permission from [143]. Copyright (2017), Society of Photo-Optical Instrumentation Engineers.***

	PbS	**ZnO/TiO_2**	**Au**	**ITO**
Work Function (eV)	4.6 [35]	5.7 [35]	5.1[147]	4.4 [148]
Thickness (nm)	300	150	100	200
E_g (eV)	1.3 [35]	3.2 [35]	-	-
$\mu_{e,h}$ ($cm^2/V.s$)	0.01 [35]	0.05 [35]	-	-
$\tau_{e,h}$ (s)	$1e^{-7}$ [35]	$1e^{-5}$ [149]	-	-
Doping (cm^{-3})	$1e^{16}$ [35]	$1e^{18}$ [35]	-	-
ε_r	20 [150]	85 [151]	-	-
m^*_e/m_0	0.2 [152]	0.943 [153]	-	-
m^*_h/m_0	0.27 [152]	1.805 [153]	-	-

4.3. Simulation results and performance analysis

4.3.1. Optical simulation results

Sample outputs from a transfer matrix optical simulation for a typical PbS CQD solar cell are illustrated in figure 4-3. As is demonstrated in figure 4-3-a, transfer matrix simulation is capable of calculating the fraction of incident light absorbed in each layer of the device structure and total light reflected from the device for any desired wavelength range. This is possible by estimating the electric field intensity distribution for each wavelength at various depths inside the device, as shown in figure 4-3-b. From the simulation results, it can be implied that the gold back contact is responsible for most of the parasitic absorption across the spectrum and any other layer except

the active layer does not absorb a significant amount of the light incident on the device. On the other hand, due to low absorption by CQDs in near-infrared region, most of the incident light in this region is reflected back from the device which emphasizes on the importance of light management strategies that are specifically designed for near-infrared portion of light in CQD-based photovoltaic devices. Furthermore, as depicted in figure 4-3-c, using the transfer matrix method, the generation rate profile inside the active layer of the device can be plotted as a function of depth. This generation rate profile can then be exploited to numerically simulate the electrical performance of the CQD solar cells.

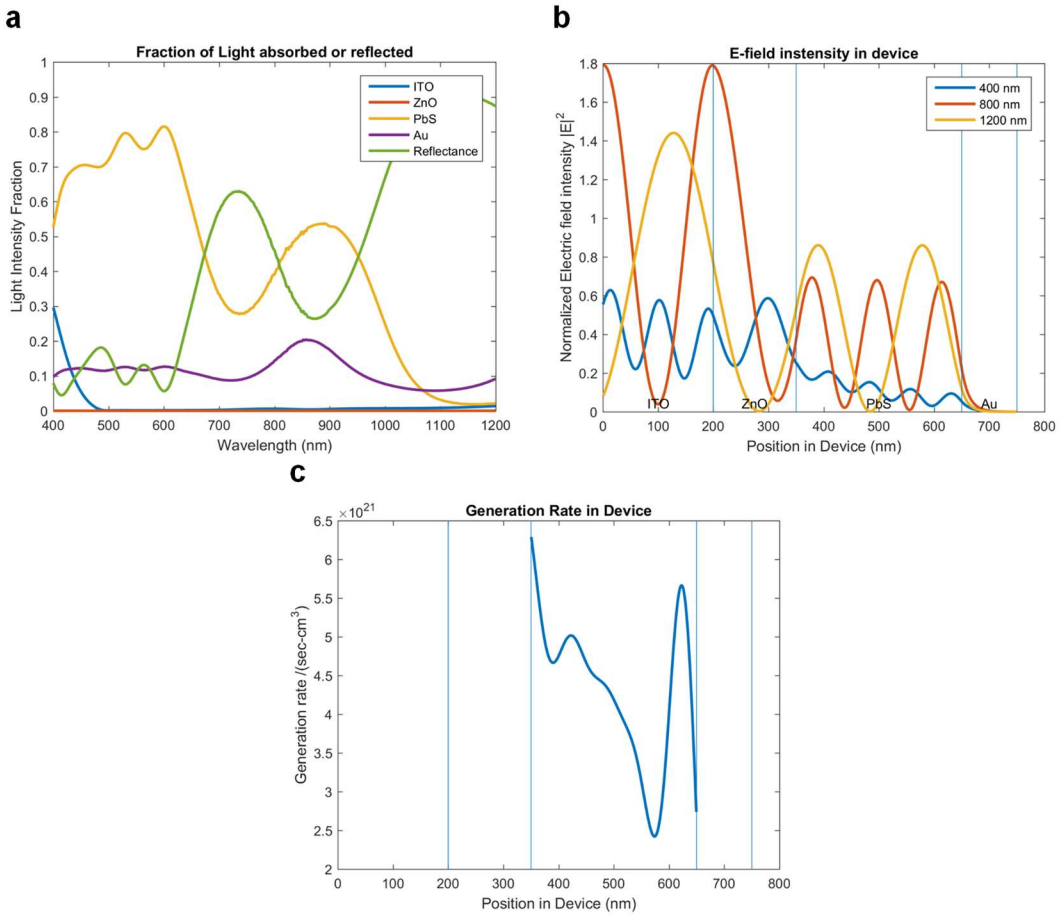

Figure 4-3: Sample output from a transfer matrix optical simulation for a typical PbS CQD solar cell. (a) Fraction of light absorbed in each layer of the device structure and total light reflected from the device. The gold back contact is responsible for most of the parasitic absorption across the spectrum. (b) Normalized E-field intensity distribution inside the device for 400, 800, and 1200 nm incident light wavelengths. (c) Generation rate profile as a function of depth inside the device structure. As is expected, carrier generation only happens inside the active layer of the device.

4.3.2. Electrical simulation results

As the ultimate goal of any light management technique is to improve the performance of thin-film solar cells, in this work, the effect of light management, or in other words light absorption enhancement, on performance merits of a CQD solar cell was numerically studied. Here, simulation conditions (see the Modeling and Simulation Methods section for details) were considered such that the cell's performance is close to experimental results for a typical depleted heterojunction CQD solar cell [35], [82], [154]. Figures 4-4-a and 4-4-b represent the simulated External Quantum Efficiency (EQE) and current-voltage characteristics of a CQD solar cell under the influence of light management at different average levels light path enhancement, respectively and table 4-2 summarizes the related performance merits and enhancements under the same conditions. As is clear from the results, light management is able to enhance the electrical performance of a CQD solar cell through broadband light path length enhancement. EQE improvements are bolder across the near-infrared region which is most needed for CQD-based photovoltaic devices. Enhancements are also obvious in the case of short-circuit current density (J_{SC}) which is clearly because of the increase in light absorption induced by light path enhancement.

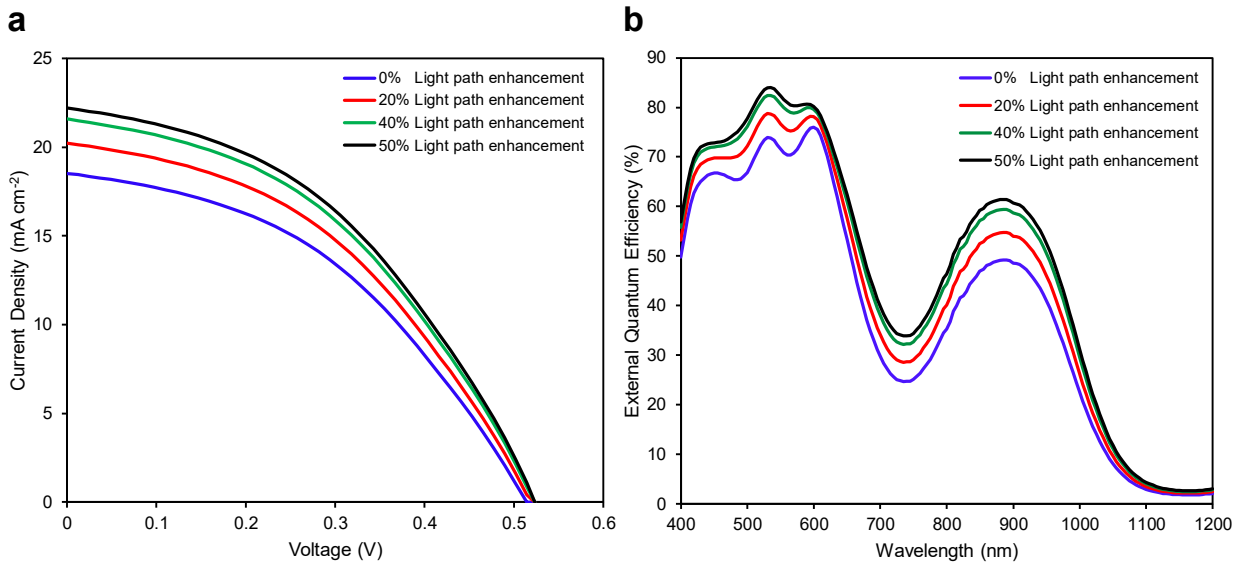

Figure 4-4: Simulation of the performance of a depleted heterojunction CQD solar cell under the influence of light management. Current-voltage characteristics (a) and external quantum efficiency (b) of a CQD solar cell with and without light management. Light path enhancement is able to improve the performance of a CQD solar cell however the improvements are not as high as expected. ***Reprinted with permission from [143]. Copyright (2017), Society of Photo-Optical Instrumentation Engineers.***

Table 4-2: Summary of the effects of light management on performance merits of a typical CQD solar cell with 300nm CQD film thickness and 100nm diffusion length. ***Reprinted with permission from [143]. Copyright (2017), Society of Photo-Optical Instrumentation Engineers.***

Average light path length enhancement ratio (%)	Average light absorption enhancement over the reference cell (%)	J_{SC} (mA/cm^2)	J_{SC} enhancement over the reference cell (%)	V_{OC} (V)	FF	η (%)	η enhancement over the reference cell (%)
0	0	18.52	0	0.513	0.42	4.04	0
20	11.91	20.23	9.23	0.518	0.42	4.45	10.15
40	22.56	21.58	16.52	0.522	0.43	4.79	18.56
50	27.51	22.21	19.92	0.523	0.43	4.95	22.52

4.4. Efficiency black hole

4.4.1. The origin

A closer look into the enhancement values summarized in table 4-2 reveals that the improvement in power conversion efficiency (η) is mainly due to the increment in short circuit current (J_{SC}), which in turn is the result of more light absorption stemming from light path length enhancement. On the other hand, although the average light path enhancement ratios considered for simulation are quite significant, the corresponding enhancements for η and J_{SC} are much lower in quantity. Even though part of this difference is because of lower than expected average light absorption enhancement due to already high enough absorption coefficient for CQDs in visible region, this indicates the presence of some strong loss mechanism that can significantly hold back the improvements achieved by light management. Detailed investigation of carrier generation and recombination rate profiles inside the CQD film of the cell without (Figure 4-5-a,c) and with (Figure 4-5-b,d) light management implementation implies that higher generation rates resulting from higher light absorption ignited by light path length enhancement are accompanied by higher recombination rates possibly stemming from high trap state densities inside the CQD film, thus limiting the electrical performance enhancement caused by light management. Therefore, the important takeaway here is that a low quality CQD film with high trap densities can severely hurt the achievements of any light management strategy. As will be discussed in the following, the validity of this conclusion for CQD-based photovoltaic devices was further examined through extensive optoelectronic modeling, simulation and performance projection under different conditions.

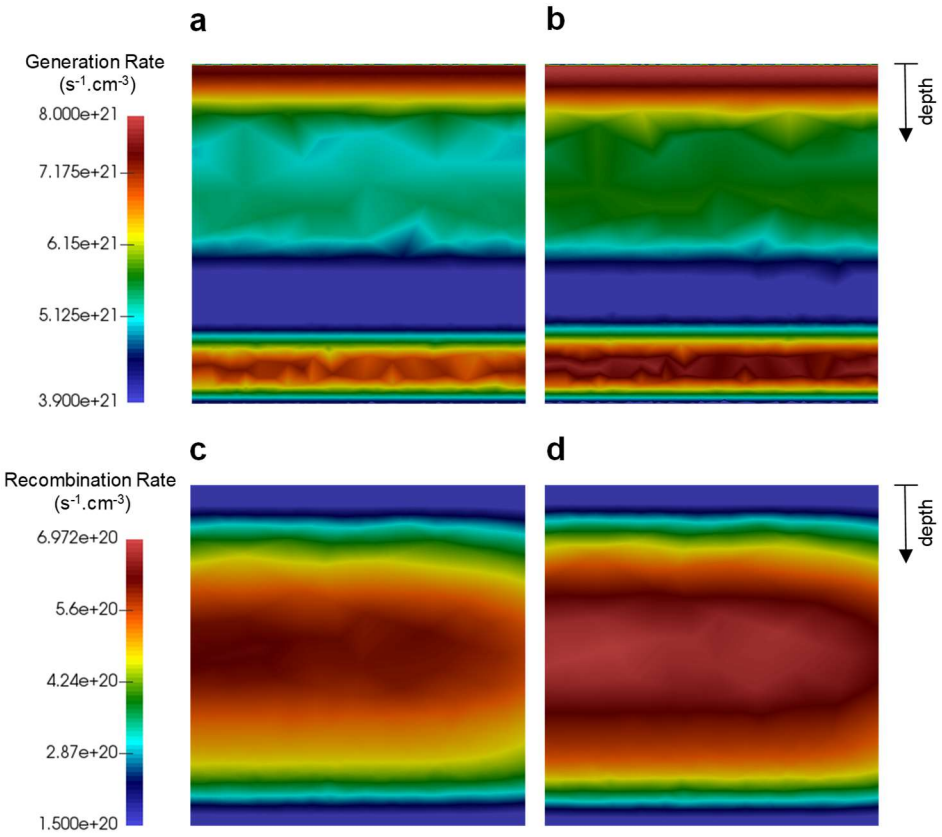

Figure 4-5: Numerical study of electrical performance of a depleted heterojunction CQD solar cell under the influence of light management. (a,b) Carrier generation and (c,d) recombination rate profiles as a function of depth inside the CQD film of the solar cell without (a,c) and with (b,d) light management. Higher generation rates resulting from higher light absorption ignited by light management are accompanied by higher recombination rates stemming from high trap state densities inside the CQD film, thus limiting the electrical performance enhancement caused by light management. ***Reprinted with permission from [143]. Copyright (2017), Society of Photo-Optical Instrumentation Engineers.***

4.4.2. Performance projections beyond the efficiency black hole

Figure 4-6 depicts the summary of optoelectronic performance projections for a PbS CQD solar cell at various levels of optical, structural and electrical enhancement for short-circuit current density (figure 4-6-a), power conversion efficiency (figure 4-6-b), fill factor (figure 4-6-c) and open-circuit voltage (figure 4-6-d). To obtain these projections, performance merits of the cell were calculated as a function of variation in the diffusion length of charge carriers inside the CQD film (which is heavily dependent on trap states densities), changes in the CQD film thickness, and

also the average light path length inside the CQD film which can be manipulated by any light management strategy.

A deep look into the obtained results suggests that for any thickness of CQD film, if the diffusion length of the charge carriers inside CQDs is below a certain limit (~ 100 nm, which is about the best practically possible value at present [35]), no matter how much the light path length is enhanced by any light management strategy, the power conversion efficiency of the cell will not be significantly improved. In other words, CQD solar cells will be stuck in an "efficiency black hole" if the carriers' diffusion length in their active layer stays below a certain limit. As can be seen from the results, even three times enhancement in light path length of a CQD solar cell cannot improve its efficiency if the cell is located in the so called efficiency black hole. This supports the aforementioned conclusion that due to the increase in trap-assisted recombination rates, higher light absorption does not necessarily translate into higher cell performance if the CQD film is not electronically optimized.

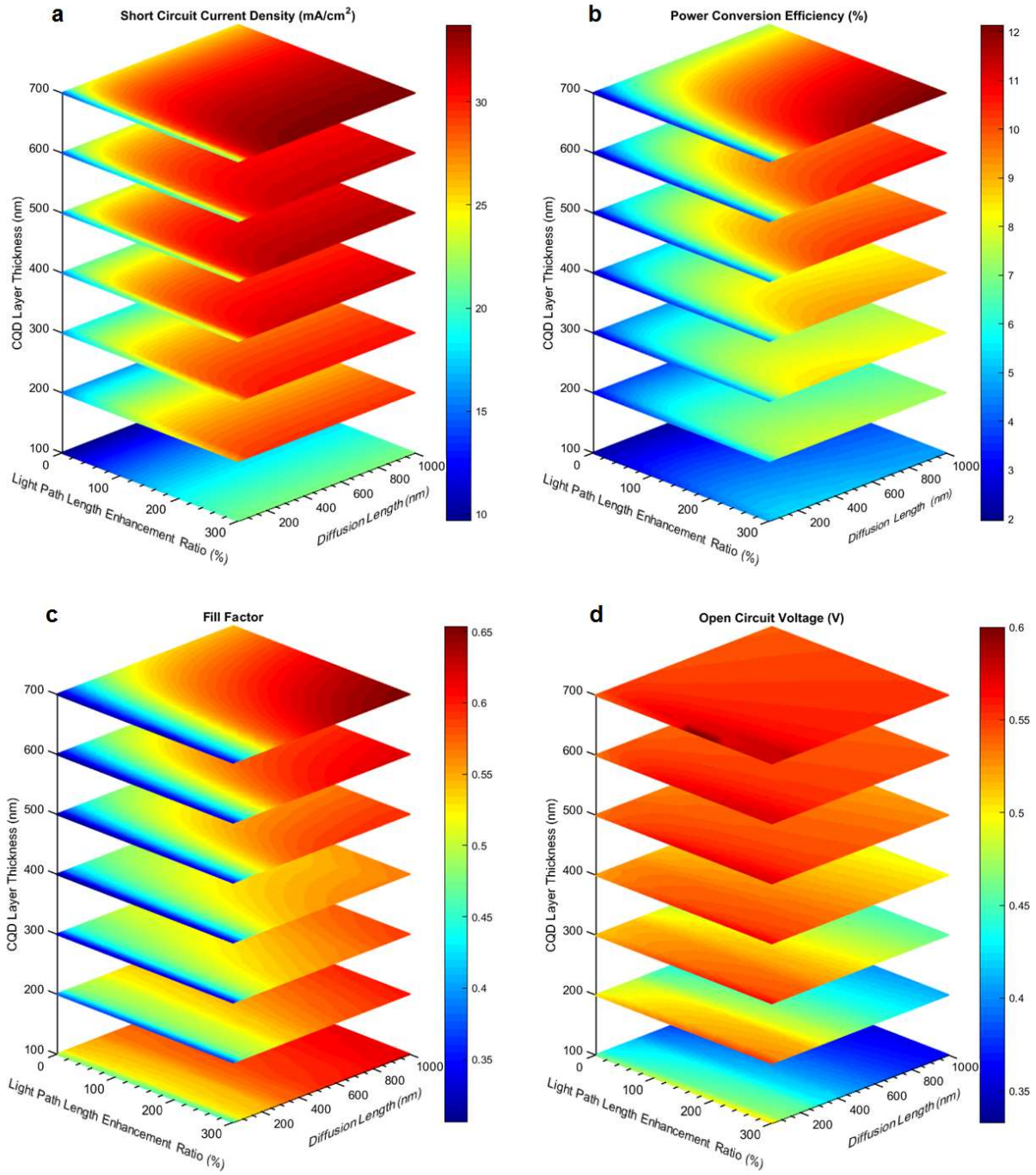

Figure 4-6: Simulated optoelectronic performance projections for a PbS CQD solar cell at various levels of optical, structural and electrical enhancement. (a) Short-circuit current density. (b) Power conversion efficiency. (c) Fill factor. (d) Open circuit voltage. The investigation of the effect of light management (light path length enhancement), structural improvement (CQD film thickness increment), and electronic property enhancement (diffusion length optimization) on the cell's performance merits reveals that both optical and electronic optimizations are equally important for an efficient photovoltaic device and neither of them should be completely neglected. ***Reprinted with permission from [143]. Copyright (2017), Society of Photo-Optical Instrumentation Engineers.***

Further investigation of performance projections plotted in figure 4-6 reveals that the mentioned efficiency black hole is mainly the result of invariability in short-circuit current and fill factor of the cells with diffusion length values below the mentioned limit. This can be attributed to the aforementioned loss mechanism due to high trap states density of CQDs which can result in higher recombination rates as the light path length in enhanced in the cell. Moreover, the same trend can be observed if no light management technique has been employed in the cell's structure. Any increase in diffusion length will not result in remarkable efficiency improvement if the light path length is not enhanced beyond a certain limit. Therefore, it seems reasonable to conclude that the efficiency black hole is the result of sole focus on enhancement of either light absorption or charge extraction capabilities of CQD solar cells.

On the other hand, based on the performance projection results illustrated in figure 4-6, it can be inferred that, in order to get out of the efficiency black hole, incorporation of an effective light trapping strategy and a high quality CQD film at the same time is an essential necessity for CQD-based photovoltaic devices. This means that CQD solar cells should increase the charge carriers' diffusion length and light path length inside their active layer to a level beyond the current practical limit. In this case, simultaneous optimization of optical (light path length), structural (CQD film thickness), and electronic (diffusion length) properties of the cell can lead to realization of very high efficiency CQD solar cells with efficiencies more than 12%. This requires light path length enhancements up to 300% and diffusion lengths up to 1μm which will then allow much thicker CQD films to be integrated into the cells' structure.

4.5. Conclusions

In summary, by employing comprehensive optoelectronic modeling and simulation, we demonstrated the presence of a strong efficiency loss mechanism, here called the "efficiency black

hole", that can significantly hold back the improvements achieved by any efficiency enhancement strategy. We proved that this efficiency black hole is the result of sole focus on enhancement of either light absorption or charge extraction capabilities of CQD solar cells. From the obtained extensive performance projection results it was inferred that, in order to get out of the efficiency black hole, incorporation of an effective light trapping strategy and a high quality CQD film at the same time is an essential necessity for CQD-based photovoltaic devices and simultaneous optimization of optical (light path length), structural (CQD film thickness), and electronic (diffusion length) properties of the cell beyond current practical limits can lead to realization of very high efficiency CQD solar cells with efficiencies more than 12%.

5

Cellulose nanocrystal:polymer hybrid optical diffusers for index-matching-free light management in optoelectronic devices

5.1. Introduction

Optical diffusers play a major role as a component in many of optoelectronic devices in which the so-called soft light with uniform spatial and directional intensity distribution is desired. For instance, optical diffusers have been extensively exploited for the purpose of uniform backlighting, brightness enhancement, efficiency improvement and increased sensitivity in liquid crystal displays (LCDs) [155]-[157], light emitting diodes (LEDs) [104]-[106], solar cells [36], [83], [100] and photodetectors [101]-[103], respectively, all of which possible through excellent light scattering properties offered by optical diffusers.

Surface-relief diffusers [158]-[160] perform light diffusion by micro/nanostructures fabricated on the surface of a film. Despite their popularity for a variety of applications, surface-relief diffusers

are not an ideal choice for integration into optoelectronic devices due to vulnerability of their surface to the damage resulting from coming into contact with other parts of the device. In addition, the requirement for the use of sophisticated surface patterning processes such as lithography makes this type of diffusers expensive to fabricate. On the other hand, volumetric diffusers [161]-[166], which rely on randomly-distributed particles as filler inside a bulk material, are not sensitive to physical contact at their surface since light diffusion happens inside the device rather than the surface. Furthermore, unlike surface-relief diffusers, they offer broadband polarization-independent light scattering thanks to the randomness of their structure. Polymeric materials such as polyethylene terephthalate (PET) [95], [155], polymethyl methcrylate (PMMA) [95], [167] and poly-carbonate (PC) [155] have gained popularity as bulk materials of optical diffusers due to their optics-friendly properties. In particular, Polydimethylsiloxane (PDMS) offers unique mechanical flexibility and optical transparency and has recently been taken advantage of in fabrication of optical diffusers [113], [132]. The filler material could be of type organic [168], in-organic [169], [170] or hybrid organic/inorganic [108], [171] and light scattering relies on the difference between refractive index of the filler and the bulk material.

As a non-toxic and biodegradable material, Cellulose nano-crystals (CNCs) are more environmental friendly than other materials since they are directly extracted from natural resources such as wood and other fiber supplies available in plants. As a high molecular weight linear polymer formed of monomers linked together by glycosidic oxygen bridges [172], They offer unique bulk and nanoscale properties (e.g. high tensile strength, high surface area for interaction with surrounding species) [173] making them suitable for use as substrate in a variety of biodegradable device applications including but not limited to sensors [174], solar cells [175], light emitting diodes [176] and transistors [177]. In addition, recently, cellulose nanofiber (CNF)-based films and papers have attracted attention for their light scattering capabilities [100], [178], [179]. Both CNCs and CNFs are very similar in terms of chemical composition and can be derived from the same source but are morphologically different in that CNFs are long (in order of microns)

and flexible composed of both crystalline and amorphous parts while CNCs are short rod-like crystals with lengths in the range of a few hundreds of nanometers [180].

Here, we propose a novel structure for optical diffusers using CNCs embedded in Polydimethylsiloxane (PDMS) matrix, or cellulose nanocrystal:polymer (CNP). Our hybrid diffuser is capable of achieving very high haze values (up to 85%), which is significantly higher than cellulose nanofiber/wood pulp diffusers [100], [179], while maintaining a high degree of transparency (~85%) at the same time. While some of the recently proposed volumetric diffusers are made of rare earth materials such as Cerium [162] which can drive up the cost of fabrication, our proposed diffuser relies on a ubiquitous material, cellulose, which is extremely cheap to produce. In addition, in the case of integration with optoelectronic devices, unlike previously reported cellulose nanofiber/wood pulp optical diffusers which require an additional index-matching layer between the diffuser and the device for efficient light coupling [100], [179], no index-matching layer between the diffuser and the device is required here due to the unique surface properties offered by PDMS as the bulk material. Through extensive experimental characterization, we prove that CNCs are an excellent candidate for filler material in a volumetric optical diffuser thanks to their rod-like shape and wavelength-scale lengths in the order of a couple of hundreds of nanometers [181], which offers excellent capabilities for broadband light softening in visible and near-infrared range of light. This is backed by the fact that while most volumetric diffusers require a filler material with concentrations up to 15 wt% for efficient light scattering [161], [163], CNP hybrid diffusers offer highly efficient light diffusion at concentrations as low as 1 wt%. As a proof of concept, we leverage light management capabilities of CNP hybrid optical diffusers to demonstrate their potential for light absorption enhancement in thin-film silicon solar cells and light extraction improvement in organic LEDs.

5.2. Experimental details

5.2.1. Cellulose nano-crystal synthesis

CNCs were obtained in powder form from Alberta-Innovates Bio Solutions and were synthesized by Acid hydrolysis technique [182]. The process was performed in two Pfaudler 50 gallon acid-resistant glass-lined reactors with a steam-heated jacket. Sulfuric acid with concentration of 64% was used with an initial reaction temperature of 45 ^{o}C. This was followed by a centrifuge step using a GEA Westfalia SC-35 separator. The next step in the process was a microfiltration step performed by a GEA filtration-ultrafiltration plant. The wet CNC powder obtained from this step was then dried in a SPX-Anhydro Model 400 spray dryer plant under an inlet temperature of 220 ^{o}C and outlet temperature of 85 ^{o}C.

5.2.2. CNP hybrid optical diffuser fabrication

CNP hybrid optical diffusers with different wt% concentrations of CNC were fabricated by a modified version of standard PDMS curing process [132]. First, a PDMS mixture was made by mixing a silicone elastomer with curing agent from a Sylgard 184 kit (Dow Corning) in 10:1 ratio. Different amounts of CNC powder (0.5-4 wt%) were then added to the mixture and vigorously mixed together using a combination of manual stirring, ultrasonic agitation and a vortex mixer to ensure uniform distribution of CNCs inside the bulk material. The mixture was then degassed in a vacuum desiccator for 60 min before being poured into a polystyrene petri dish. The resulting film was then left on a pre-leveled platform at room temperature overnight to form a uniformly thick film and then was cured on a hot plate 80^{o}C for 2h. The thickness of the film was controlled by carefully adjusting the amount of volume for the mixture that was being poured into the petri dish. After the curing step, the film could easily be peeled off due to the hydrophobicity of polystyrene surface.

5.2.3. Characterization

The transmission electron microscopy images were obtained by a Hitachi S-9500 TEM. Transmittance and haze for optical diffusers were obtained by using the 150 mm integrating

sphere module of a Perkin-Elmer Lambda 1050 UV–Vis–NIR Spectrophotometer. A custom-made fixture was used to hold the sample at the sample beam entrance port of the sphere. Angle dependent specular transmissions were measured using the same setup with the sample being located on a rotating stage. For transmittance measurement, all the ports of the integrating sphere except the reference and sample beam entrance ports were kept closed. In the case of haze, the back port of the integrating sphere was opened to prevent the specular transmission from the sample to be captured by the detector.

Visual demonstrations of optical diffusion by samples were performed using a laser diode (Newport) emitting at 635 nm as the light source with the sample covering the output window of the laser diode. The light passing through the diffuser samples was projected on a white screen located in front of the laser diode. The angular intensity distribution of the laser beam was acquired by a Thorlabs power meter situated in the same horizontal plane as the center of the laser beam. The angular position of the power meter was then changed using a custom-built fixture to measure the light intensity at different angular positions with respect to the center of the laser beam.

The effect of CNP hybrid optical diffusers on light absorption enhancement in silicon was investigated using a 200μm thick silicon slab with optical diffuser samples being directly attached to the silicon surface. The absorption measurement was accomplished by putting the sample at the center of the integrating sphere of a Perkin-Elmer Lambda 1050 UV–Vis–NIR Spectrophotometer using a center mount sample holder.

In order to test the application of CNP hybrid optical diffusers on light extraction improvement in organic LEDs, diffuser samples were directly attached to the back side of the glass substrate of an OLED device fabricated according to a previously published procedure [183]. Quantum efficiency, luminance, power efficiency and current-voltage characteristics of the OLED device were measured using a Keithley 2400 source-meter, a calibrated luminance meter (Konica

Minolta LS-110) and a PR-705 Spectrascan spectrophotometer with an integrating sphere in the air and at room temperature.

5.3. Optical diffusion, transmission and haze analysis

Figure 5-1-a shows a photograph of CNP hybrid optical diffusers with different CNC concentrations (from left to right 0.5, 1, 2, and 4 wt.%). As is obvious from the appearance of the samples in the picture, a change in transparency and light diffusion behavior of the samples is observed with increase in CNC concentration. Higher concentration provides lower transparency while offering higher light diffusion performance. This is in agreement with other types of volumetric diffusers as it is known that the density of the filler material can directly affect the transparency and the haze (the percentage of total transmitted light that is diffusely scattered) of the diffuser [161], [163], [169]. Additionally, it was observed that the flexibility and mechanical properties of PDMS enable the CNP diffusers to withstand harsh physical stresses such as stretch, twisting and bending (figure 5-1-b) without any change in their properties, a feature that is not offered by cellulose nanofiber/wood pulp optical diffusers.

By employing Transmission Electron Microscopy (TEM) of the CNCs (figure 5-1-c-f), both individual and aggregated clusters of CNCs were found to be present in the raw material, a feature which we believe could be carried over once CNCs are embedded in PDMS. In this case, the observed aggregations in TEM images can potentially enhance the scattering efficiency of CNCs. In addition, Helium Ion Microscopy (HIM) was used to characterize the morphology of CNC embedded films. From the obtained images (not shown), due to the similarity of the composition of CNCs and PDMS (one a naturally occurring polymer and the other a synthetic polymer), it was not possible to observe the distribution of CNCs inside PDMS due to the lack of any contrast between the two materials during imaging. Based on the observations, we believe that a combination Rayleigh and Mie scattering can be responsible for light scattering in CNP hybrid

diffusers, the former resulting from individual CNCs and the latter stemming from possible clusters of aggregated CNCs in the matrix material.

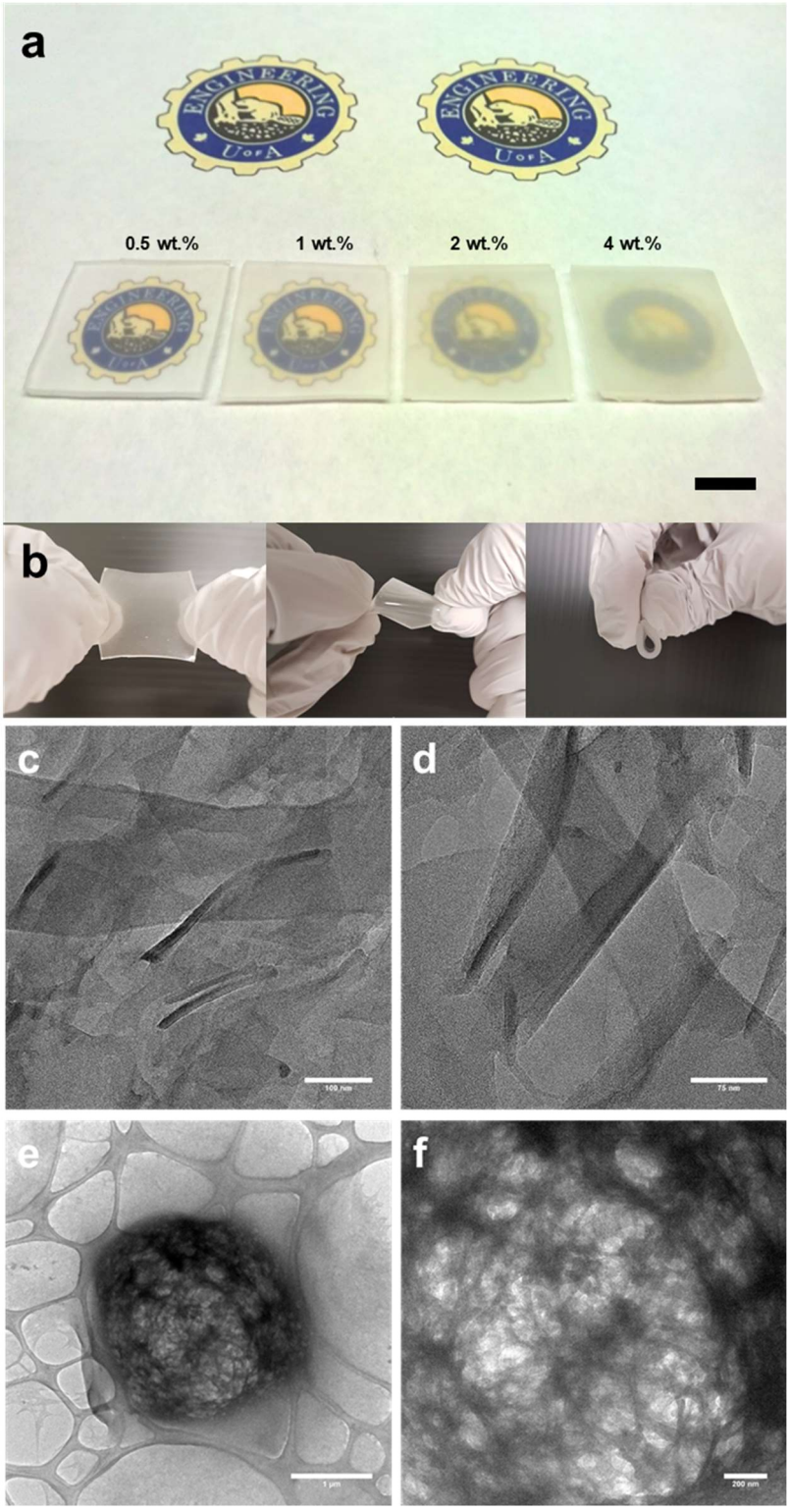

Figure 5-1: (a) Photograph of CNP hybrid optical diffusers with different CNC concentrations (from left to right: 0.5, 1, 2, and 4 wt.%). The change in transparency and light diffusion behavior of the samples with an increase in CNC concentration is obvious from the picture. (The scale bar is 1 cm) (b) Physical durability of the diffusers allows application of stretch, twisting and bending without any effect on their optical properties. (b,c) Transmission electron microscopy images of individual cellulose nanocrystals. (c-f) Transmission electron microscopy images of cellulose nanocrystals before mixing with matrix material. (c,d) individual nanocrystals (e,f) an aggregated cluster of nanocrystals. ***Reprinted with permission from [189]. Copyright (2017), Wiley-VCH***

In order to optimize the amount of filler material for the composite diffuser, we measured the transmittance and haze of various CNP hybrid optical diffusers with different concentrations (wt.%) of CNC as a function of wavelength for visible and near-infrared regions of light. Transmittance and haze of a commercially available diffuser (market diffuser) from a solar simulator system were also measured for comparison. As is depicted in figure 5-2, high transmittance and very high haze values are achievable across a wide range of wavelengths with the proposed diffuser structure, which can be attributed the difference in refractive index of cellulose (~1.6) [184] and PDMS (~1.4) [185]. Compared to other cases, a 1 wt.% concentration for CNC in PDMS seems to provide a very high level of haze (more than 90%) while maintaining a high level of transparency at the same time. Furthermore, it is able to provide the same performance level as a commercial diffuser. In all the other cases, either the transparency or the haze level are compromised in favor of each other. For instance, in the case of a 4 wt.% CNC concentration, despite the fact that almost all light that is passing through the sample is being diffused (~100% haze), the transmittance is significantly lower than the acceptable level for an optical diffuser. In addition, from the obtained results, it can be concluded that the performance of CNC/PDMS optical diffusers is almost independent of the wavelength of incident light which is a direct consequence of the randomness of their light scattering structure.

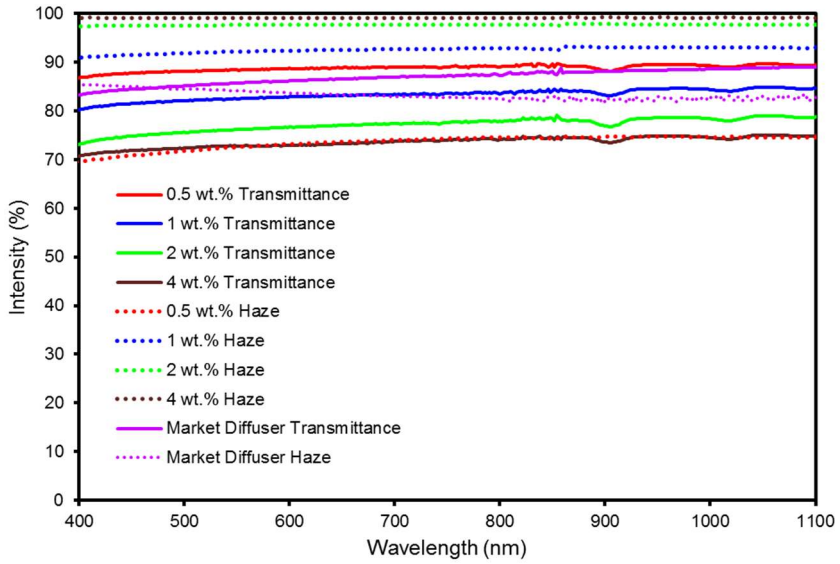

Figure 5-2: Transmittance and haze of CNP hybrid optical diffusers with different concentrations (wt.%) of CNC as a function of wavelength. High transmittance and super-high haze values are achievable across a wide range of wavelengths with the proposed diffuser structure. Transmittance and haze of a commercially available diffuser (market diffuser) are also included for comparison. ***Reprinted with permission from [189]. Copyright (2017), Wiley-VCH***

Optical diffusion of a 635 nm laser beam by CNP hybrid optical diffusers with different concentrations of CNC and their comparison with a market diffuser are demonstrated in figure 5-3. It can be inferred from the figure that the addition of CNC filler to PDMS as bulk material is the only reason for the observed light scattering since no noticeable change on the laser beam was observed when passing through a PDMS film with no CNC addition (0 wt.%). Additionally, better light softening performance and wider scattering angles were observed with increase in filler material concentration which is in complete agreement with the observations from wavelength-dependent haze measurements in figure 5-2. Moreover, as is clear from the figure, a 1 wt.% diffuser offers almost the same performance as the market diffuser while catering wider scattering angles which can be attributed to the superior light scattering capabilities of CNCs as a filler material.

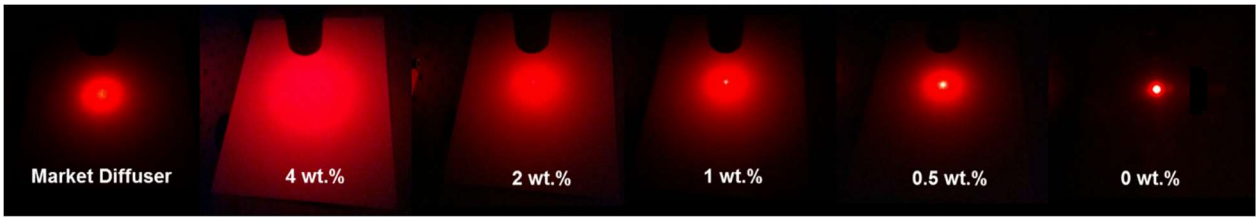

Figure 5-3: Optical diffusion of a 635 nm laser beam by CNP hybrid optical diffusers with different concentrations (wt.%) of CNC and comparison with a market diffuser. ***Reprinted with permission from [189]. Copyright (2017), Wiley-VCH***

Figure 5-4 illustrates the angular intensity distribution of a 635 nm laser beam after passing through a CNP hybrid optical diffuser with different concentrations of CNC. It is evident from the results that as the concentration of light diffusing material increases, light scattering angles tend to be wider and the intensity distribution becomes more uniform which is consistent with visual observations of light diffusion from figure 5-3. In the case of the sample with 4 wt.% CNC concentration, the intensity distribution is very close to an ideal diffuse surface with Lambertian distribution (dashed line). This emphasizes the excellent light diffusion ability of CNCs being able to offer a Lambertian-like distribution with only 4 wt.% concentration of filler material.

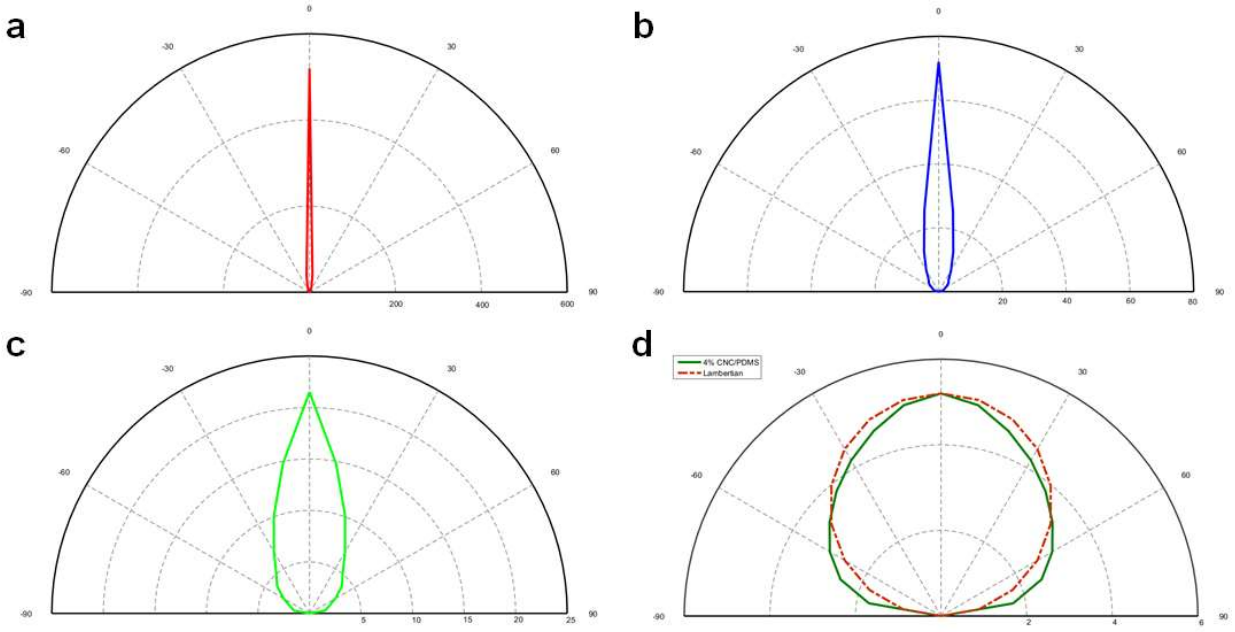

Figure 5-4: Angular intensity distribution of a 635 nm laser beam after passing through a CNP hybrid optical diffuser with different concentrations (wt.%) of CNC. (a) 0.5 wt.% (b) 1 wt.% (c) 2 wt.% (d) 4 wt.%. As the concentration of light diffusing material increases, the distribution becomes more uniform. The sample with 4 wt.% concentration is very close to an ideal diffuse surface with Lambertian distribution (dashed line). ***Reprinted with permission from [189]. Copyright (2017), Wiley-VCH***

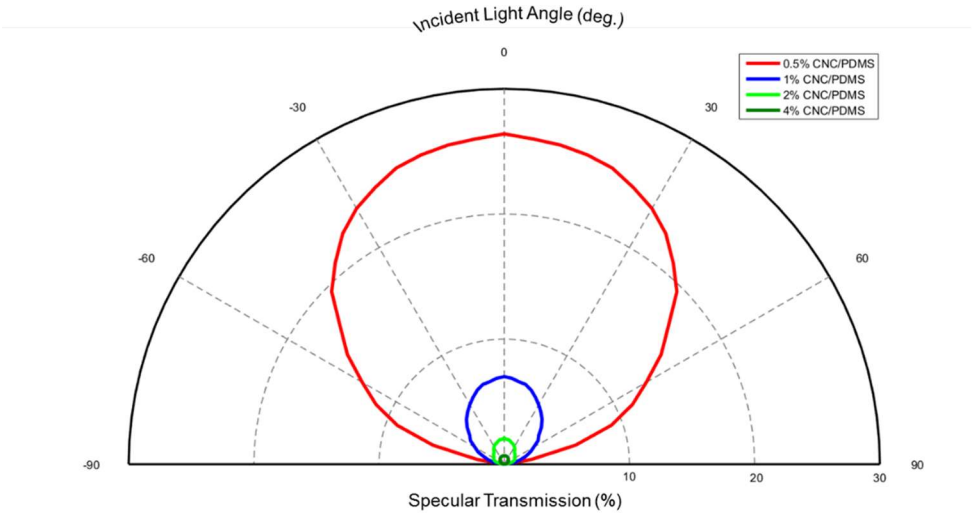

Figure 5-5: Dependency of specular transmission of CNP hybrid optical diffusers on the incident light angle for different concentrations of CNC. At oblique angles, more light diffusion can be observed from the diffusers. ***Reprinted with permission from [189]. Copyright (2017), Wiley-VCH***

Since it is expected from an optical diffuser to maintain its performance at different incident light angles, the dependency of the performance of CNP hybrid optical diffusers on the incident light angle for different concentrations of CNC was investigated as shown in figure 5-5. From the obtained results, it can be concluded that at oblique angles, CNP hybrid optical diffusers offer even higher performance than a normal light incidence. This can be related to the fact that light has to travel a longer path inside the light scattering medium at oblique angles and in this case the chance of light being scattered will become higher due to high density of scattering sites created by the filler material inside the volumetric diffuser. This can be especially useful in light harvesting applications for ambient light since the incident direction can be randomly oriented most of the times.

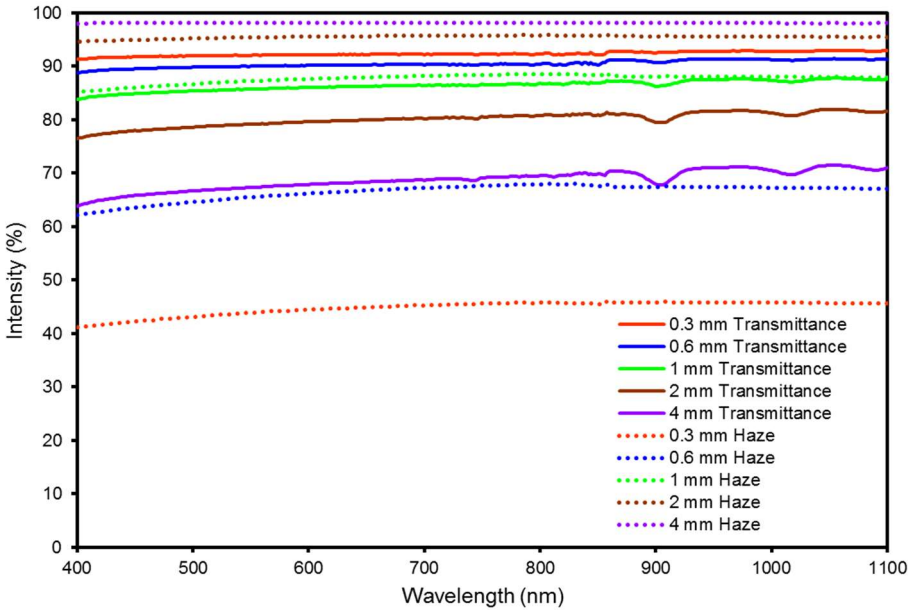

Figure 5-6: Transmittance and haze of 1 wt.% CNP hybrid optical diffusers with different thicknesses as a function of wavelength. Although higher thicknesses can provide higher haze, the transmittance of the diffuser can be severely affected by the thickness. A 1 mm thick diffuser seems to have optimum transmittance and haze values for optoelectronic applications. ***Reprinted with permission from [189]. Copyright (2017), Wiley-VCH***

In a volumetric diffuser, because the light scattering material is distributed inside the bulk material, the thickness of the diffuser itself can play an important role in the performance of the device. Therefore, optimization of the thickness of CNP hybrid optical diffusers for the desired transparency and haze seems to be an essential step toward the design of an optimally performing optical diffuser. Figure 5-6 depicts the transmittance and haze of 1 wt.% CNP hybrid optical diffusers with different thicknesses as a function of wavelength. It is evident from the figure that although higher thicknesses can provide higher haze obviously due to longer light traveling path inside a scattering medium, the transmittance of the diffuser can be negatively affected by the thickness. From the results, it is reasonable to infer that a 1 mm thick diffuser seems to have optimum transmittance and haze values (~85%) for optoelectronic applications.

5.4. Index-matching-free light management in optoelectronic devices

Due to the excellent light scattering capabilities offered by CNP hybrid optical diffusers, one potential application of the proposed optical diffuser can be the enhancement of light absorption inside the active layer of thin-film solar cells and photodetectors through its high haze property. The optical diffuser can laminate the front surface of any previously fabricated photovoltaic device to contribute to its light management capabilities. In order to investigate this potential application, CNP hybrid optical diffusers were tested for enhancement of light absorption in a 200μm thick silicon slab as illustrated in the schematic of the light scattering effect of the CNP hybrid optical diffuser on the silicon slab in figure 5-7 (left). Unlike most of the cellulose-based optical diffusers [99], [177], no index-matching layer between the diffuser and the device is required due to the smooth surface offered by PDMS as the bulk material and also its tendency to easily adhere to glass and silicon surfaces without leaving any air gap in between.

Figure 5-7 (right) depicts the amount of absorption in a 200 μm thick silicon slab versus incident light wavelength without diffuser and with diffusers having different concentrations of CNC. As is clear from the figure, the absorption in silicon slab is significantly enhanced with the addition of a CNP hybrid optical diffuser. This is due to the fact that the diffusive behavior of the optical diffuser results in the increase in the light path length inside the slab which in turn increases the chance of light absorption. In addition, a portion of the observed absorption enhancement could be the result of lower light reflection from the surface of silicon since the optical diffuser can reduce the refractive index contrast between air (1) and the silicon slab (~3) by its intermediate refractive index (~1.5). However, it is obvious that high concentrations of CNC are not as effective in enhancing the absorption due to the reduction in transmittance of the diffuser at high concentrations as was shown in figure 5-2. For example, lower transmittance offered by 2 wt.% CNC despite providing higher haze compared to 1 wt.% can be considered the reason behind observing similar light absorption performance in silicon slab for both concentrations. From the results, it can be concluded that a concentration of 1 wt.% for CNC as the filler material is the optimized concentration for this application. The absorption enhancement in all cases occurs over

a broad range of wavelength in both visible and near-infrared regions of light which is a common feature of volumetric diffusers.

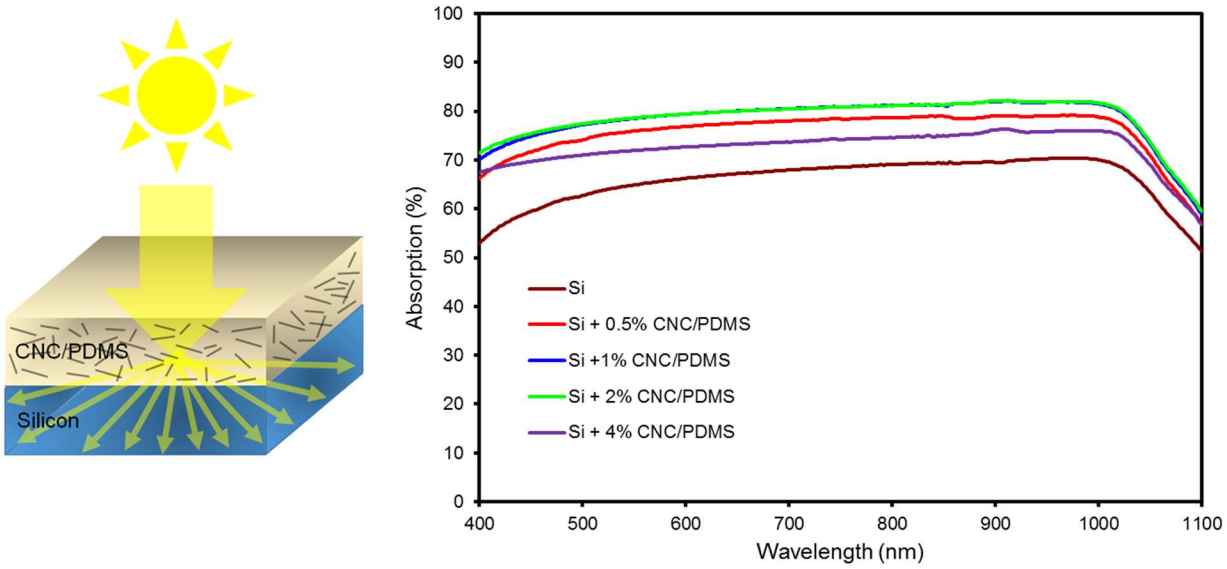

Figure 5-7: Demonstration of the potential application of CNP hybrid optical diffusers for light management in silicon solar cells. (Left) The schematic of the light scattering effect of the CNP hybrid optical diffuser on a silicon slab. (Right) Absorption in a 200μm thick silicon slab versus incident light wavelength without diffuser and with diffusers having different concentrations of CNC. The absorption in silicon slab is significantly enhanced with the addition of a CNC/PDMS diffuser. However, high concentrations of CNC can reduce the absorption due to the reduction in transmittance of the diffuser. A concentration of 1 wt.% for CNC seems to be the optimized concentration for this application. ***Reprinted with permission from [189]. Copyright (2017), Wiley-VCH***

The application of CNP hybrid optical diffusers can be extended to thin-film light emitting diodes (LEDs) as well. LEDs are known to suffer from light trapping as the so-called substrate modes inside their substrate due to the refractive index contrast between glass and air which contributes to the occurrence of total internal reflection [187]. As illustrated in figure 5-8-a, the proposed optical diffuser can be exploited to enhance light extraction efficiency in an organic LED by being directly attached to the glass substrate of the device which can provide local scattering sites and refractive index change to suppress part of total internal reflection at the substrate/air interface. Just like the case of photovoltaic devices, no index matching layer is required between the diffuser and the OLED device. Current-voltage characteristics and luminance of the OLED device as a

function of bias voltage without diffuser and with diffusers having different concentrations of CNC are shown in figures 5-8-b and 5-8-c, respectively. It is evident from the results that although in all cases the OLED device draws the same current at different bias voltages, its luminance is subject to change when the optical diffuser is attached, which confirms that the attachment of an optical diffuser to the OLED device can affect the OLED's light extraction capability.

A deeper look into the luminance of the OLED device with optical diffusers having different concentrations of CNC reveals that a 1 wt.% CNP hybrid optical diffuser provides highest light extraction performance compared to the other concentrations which can be attributed to its optimal level of transparency and haze as was demonstrated in the previous section. Furthermore, it was found that a 0.5 wt.% concentration makes almost no difference in light extraction from an OLED possibly because of its low level of haze and a 4 wt.% concentration can result in lower luminance than an OLED without a diffuser probably due to its lackluster degree of transparency.

Power efficiency and External quantum efficiency (EQE) of the OLED device as a function of luminance without diffuser and with diffusers having different concentrations of CNC are illustrated in figures 5-9-a and 5-9-b, respectively. The results are consistent with the observations in figure 5-8 as 1 and 2 wt.% CNP hybrid diffusers offer almost the same light extraction enhancement while a 0.5 wt.% device results in fairly the same performance as the reference device with no diffuser and the 4 wt.% device provides a lower performance than the reference device. Thanks to its superior light extraction capabilities, the proposed CNP hybrid optical diffuser is able to enhance the external quantum efficiency of an OLED device by about 15% on average which showcases the great potential of the proposed optical diffuser for light extraction enhancement in light emitting devices. The proposed light extraction technique is applicable to any previously fabricated LED device since the light extraction structure is not part of the device structure and can easily be laminated on any device and could be replaced in case of degradation.

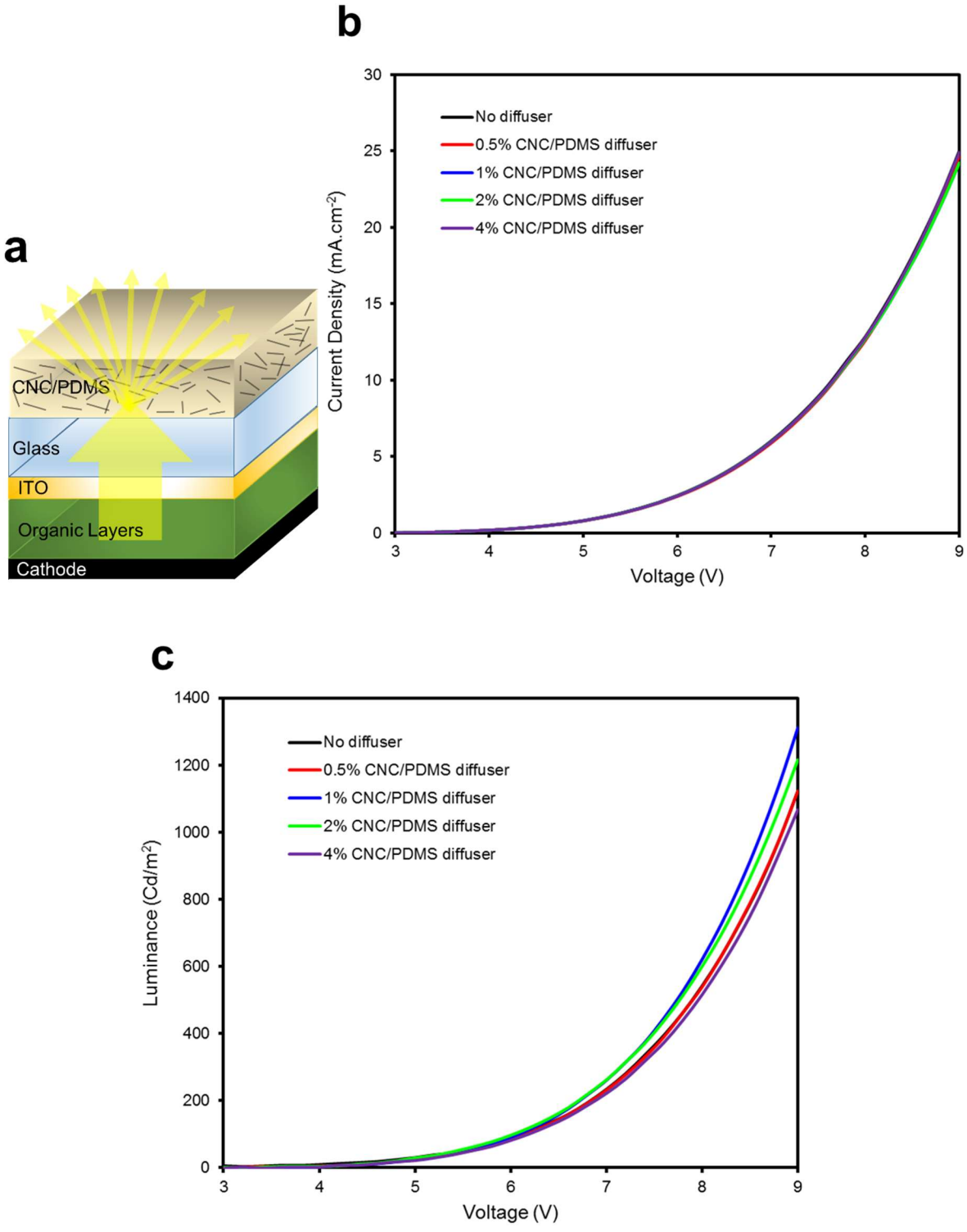

Figure 5-8: Light extraction enhancement in OLEDs using CNP hybrid optical diffusers. (a) Schematic of the OLED structure with attached CNP hybrid optical diffuser. (b) Current-voltage characteristics of the OLED under different conditions. (c) Luminance of the OLED as a function of bias voltage without diffuser and with diffusers having

different concentrations of CNC. Enhancements in the luminance of the OLED with attached optical diffuser are obvious from the figure. ***Reprinted with permission from [189]. Copyright (2017), Wiley-VCH***

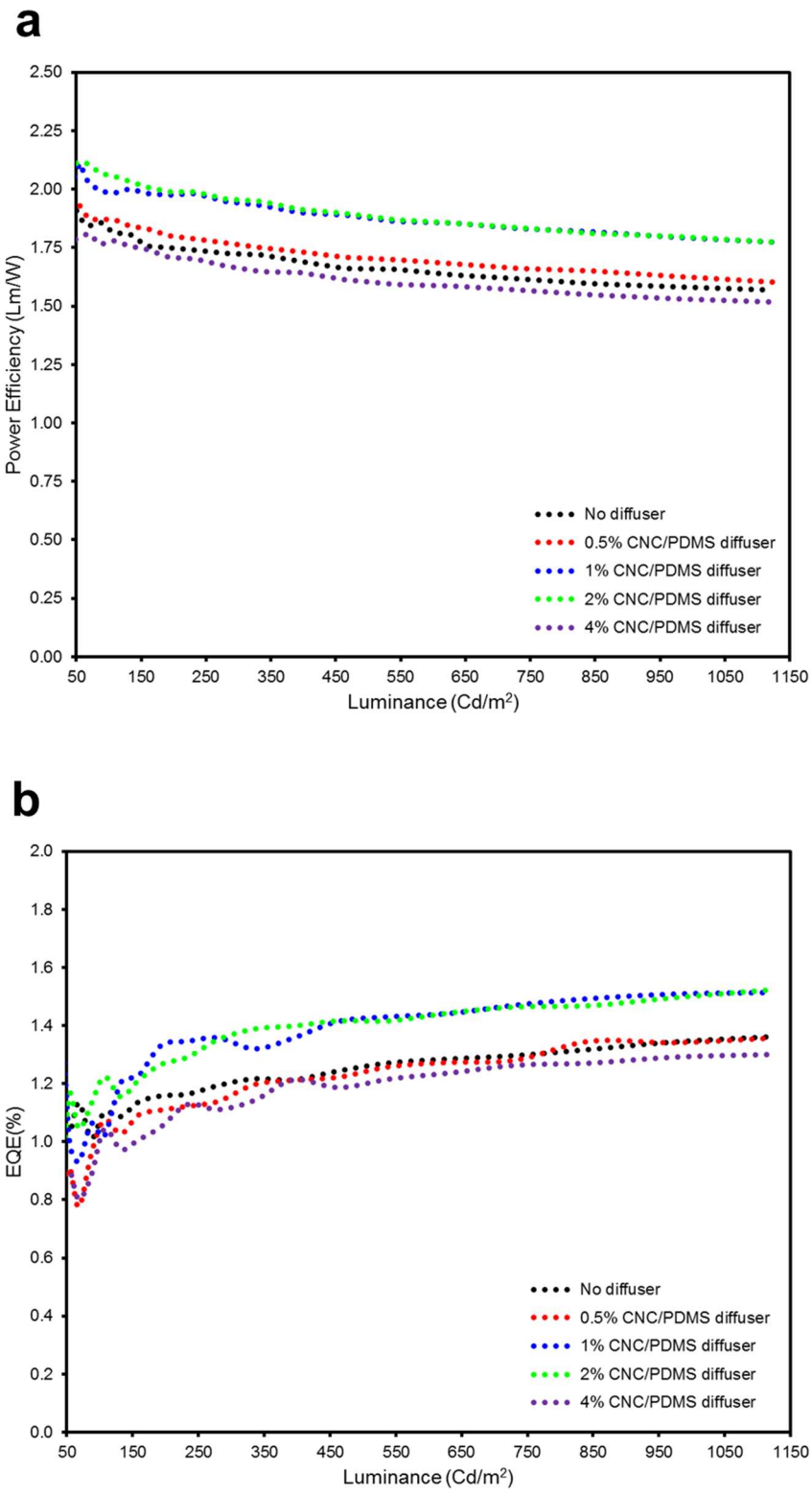

Figure 5-9: (a) Power efficiency and (b) External quantum efficiency of the OLED device without diffuser and with diffusers having different concentrations of CNC. The diffuser with 1% wt. CNC concentration has the highest enhancement in the efficiency of the device. ***Reprinted with permission from [189]. Copyright (2017), Wiley-VCH***

5.5. Conclusions

In this work, we reported on a novel volumetric optical diffuser based on cellulose nano-crystals (CNC) embedded in Polydimethylsiloxane (PDMS) or as we call it "CNP hybrid optical diffuser". By offering a very simple and low-cost fabrication process as well as compatibility with large-scale production using an earth-abundant material (cellulose) as filler, the proposed optical diffuser is an ideal choice for integration into optoelectronic devices for light management especially due to its insensitivity to physical damage at its surface and the lack of requirement for an index-matching layer between the diffuser and the optoelectronic device thanks to the unique surface properties, mechanical flexibility and optical transparency offered by PDMS as the bulk material.

We demonstrated that CNCs are an excellent candidate for filler material in a volumetric optical diffuser providing excellent capabilities for broadband light softening in visible and near-infrared range of light and highly efficient light diffusion at concentrations as low as 1 wt%. It was shown that at its optimized form, a CNP hybrid optical diffuser is capable of achieving super-high haze values (up to 85%) while maintaining a high degree of transparency (~85%) at the same time. While we only leveraged light management capabilities of CNP hybrid optical diffusers to demonstrate their potential for light absorption enhancement in thin-film silicon solar cells and light extraction improvement in organic LEDs, the proposed optical diffusers can be applicable to any other type of LED or solar cell devices without any change to the structure or fabrication process of the device by a simple lamination process.

6

Conclusion

6.1. Summary of accomplishments and contributions

The main objective of the thesis was to leverage nanotechnology to address light absorption and light extraction deficiencies in thin-film photovoltaic devices and light emitting diodes, respectively, using simple and low-cost solutions. This objective was accomplished using easily fabricable hierarchical nanostructures by taking advantage of theory, simulation and experimental design, fabrication and characterization.

By using 2D and 3D FDTD simulations, the potential of nanostructured ITO diffraction gratings was highlighted as an effective structure for light absorption enhancement in PbS CQD solar cells at near-infrared region where these types of solar cells typically demonstrate weak light absorption. Various ITO diffraction grating structures were investigated and compared to each other in terms of broadband light absorption enhancement and by providing compelling evidence it was hypothesized that guided-mode resonances excited by coupling of the incident diffracted light into the supported waveguide modes is the main reason behind the broadband light absorption enhancement in solar cells with ITO grating structures as compared to the reference planar solar cell without any gratings. Moreover, grating far-field projection analysis was proved

to be a powerful approach to predict guided-mode resonance wavelengths. Polarization-independent broadband light absorption enhancement of more than 40% was predicted for 2D ITO nano-branch gratings as the best-performing structure and the absorption enhancement was proved to be almost independent of possible fabrication flaws in grating structure.

In order to extend the application of nanostructured diffraction gratings for light management to any type of thin-film solar cells not just CQD solar cells, a novel type of diffraction grating referred to as "stretchable hexagonal diffraction grating" was introduced in this thesis and its potential as an optical diffuser for photon management in thin-film solar cells was explored. The easily fabricated grating structure was devised based on hexagonal arrays of Polystyrene nanospheres formed on an elastomer PDMS substrate. The proposed device was shown to be widely tunable in terms of the diffraction angles, the number of supported orders, and the energy distribution into higher diffracted orders, thanks to the flexibility of its structure. As an application example, the stretchable hexagonal grating was demonstrated both numerically and experimentally to be able to offer broadband tunable light absorption enhancement in colloidal quantum dot (CQD) thin-films. The novel optical diffuser proposed in this thesis is easily usable for any previously fabricated optoelectronic device, without the cumbersomeness of modifying the device's structure or fabrication process.

In addition, by employing comprehensive optoelectronic modeling and simulation, the presence of a strong efficiency loss mechanism, named as the "efficiency black hole", that can significantly hold back the improvements achieved by any light management strategy was demonstrated in CQD solar cells for the first time. It was argued that this efficiency black hole is the result of sole focus on enhancement of either light absorption or charge extraction capabilities of CQD solar cells. By using the performance prediction capabilities of the developed optoelectronic model it was inferred that, in order to get out of the efficiency black hole, incorporation of an effective light trapping strategy and a high quality CQD film at the same time is an essential necessity for CQD-

based photovoltaic devices and simultaneous optimization of optical (light path length), structural (CQD film thickness), and electronic (diffusion length) properties of the cell beyond current practical limits can lead to realization of very high efficiency CQD solar cells.

By taking advantage of light scattering media as a light management strategy for thin-film optoelectronic devices, a novel volumetric optical diffuser based on cellulose nano-crystals (CNCs) embedded in Polydimethylsiloxane (PDMS) called as "CNP hybrid optical diffuser" was reported in thesis. By offering a very simple and low-cost fabrication process as well as compatibility with large-scale production using an earth-abundant material (cellulose) as filler, the proposed optical diffuser is an ideal choice for integration into optoelectronic devices for light management especially due to its insensitivity to physical damage at its surface and the lack of requirement for an index-matching layer between the diffuser and the optoelectronic device thanks to the unique surface properties, mechanical flexibility and optical transparency offered by PDMS as the bulk material. It was demonstrated that CNCs are an excellent candidate for filler material in a volumetric optical diffuser providing excellent capabilities for broadband light softening in visible and near-infrared range of light and highly efficient light diffusion at very low concentrations. It was also shown that at its optimized form, a CNP hybrid optical diffuser can achieve super-high haze values while maintaining a high degree of transparency at the same time. Light management capabilities of CNP hybrid optical diffusers were leveraged to demonstrate their potential for light absorption enhancement in thin-film silicon solar cells and light extraction improvement in organic LEDs,

6.2. Future outlook

6.2.1. ITO nano-branch electrodes for organic solar cells

During the course of research about the application of ITO nano-branch structures for light management in colloidal quantum dot solar cells in this thesis it was found out that practical

integration of the ITO nano-branches with quantum dots is not possible due to the difficulties in formation of a continuous active layer using the common deposition methods used for colloidal quantum dots which have the tendency to leave large voids inside the active layer after deposition, disrupting the operation of the device. I expect however that other thin-film solar cell technologies such as organic solar cells may not necessarily suffer from the same problem. Organic materials might be a better candidate for integration with ITO nano-branch electrodes and I think it is worth to try to extend the idea to other thin-film solar cell technologies.

6.2.2. Tuning the structure of PS/PDMS hexagonal diffraction gratings for better tailored light management

In addition to physical flexibility, the stretchable hexagonal diffraction grating concept illustrated in this thesis offers lots of degrees of freedom in its structure design. A variety of different PS nanosphere sizes can be chosen for fabrication to achieve different periodicities, and even their size can be fine-tuned with nanometer accuracy by reactive ion etching (RIE) processes which provides endless possibilities for adjusting the diffractive properties of the device. Moreover, optimizing the mechanical properties of the PDMS substrate for smaller elasticity modulus is expected to enhance the device's diffusive capability due to the possibility of higher stretch application which can provide support for additional diffracted orders. Better engineering of the nanosphere self-assembly for larger area of perfectly patterned domains may also lead to performance enhancement for the proposed optical diffuser.

6.2.3. Stretchable hexagonal diffraction grating for efficiency enhancement in vertical multi-junction solar cells

Since the proposed stretchable hexagonal diffraction grating in this thesis is capable of spatial separation of different wavelengths of light, it could be an ideal candidate for integration into vertical multi-junction solar cells or as they are called edge-illumination solar cells [188]. Vertical

multi-junction solar cells include a number of edge-illuminated junctions attached together in parallel or series as is illustrated in figure 6-1. Normally, each junction receives the same light distribution (full solar spectrum) as all the other junctions but every junction is only capable of absorbing a specific part of solar spectrum based on the material that it is made of, which causes a massive loss of the incident energy. Our proposed diffraction grating can be used to decompose the incident light into different spatially separated wavelengths (colors) and thus each junction can only be exposed to the specific wavelength range for which it has maximum efficiency in light absorption. This idea has the potential to significantly reduce the light absorption loss in vertical multi-junction solar cells and I believe could be the subject of future research based on the hexagonal diffraction grating proposed in this thesis.

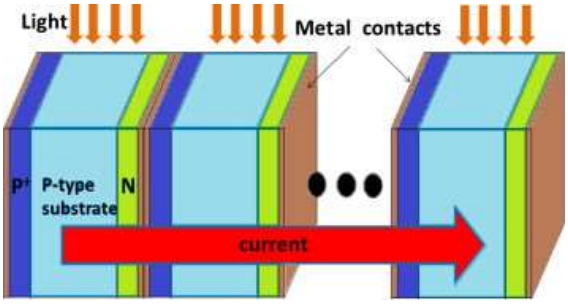

Figure 6-1: The schematic of a vertical multi-junction solar cell. ***Reprinted from [188], Copyright (2013), with permission from Elsevier.***

6.2.4. Improving the quality of quantum dot thin-films

As was concluded from extensive optoelectronic modeling and simulation reported in chapter 4, current diffusion length values for colloidal quantum dot thin-films are not ideal for significant effectiveness of light management strategies on efficiency enhancement of colloidal quantum dot solar cells. The developed model predicted that slight improvement in diffusion length of the quantum dot film can bring the cells out of the efficiency black hole. Better engineering of the current quantum dot synthesis processes might lead this prediction to come true and in that case the accuracy of the developed model can be further investigated in terms of any potential

mismatch between the predictions offered by the model for higher quality quantum dot films and the experimental results.

6.2.5. Application of CNP hybrid optical diffuser for other types of thin-film LEDs

Due to the fact that the proposed CNP hybrid optical diffusers in this thesis are not designed as an internal part of a LED device, they can be applicable to any other type of thin-film LEDs or solar cell devices for enhanced light management without any change to the structure or fabrication process of the device by a simple lamination process. Especially, in the case of quantum dot or perovskite based LEDs, due to the extremely high refractive values for the materials forming the device, light trapping is a major bottleneck for efficiency of these devices. As such, the same proposed CNP hybrid optical diffusers can be investigated for their effectiveness in light extraction enhancement in quantum dot or perovskite LEDs.

References

1. W. van Roosbroeck and W. Shockley, "Photon-radiative recombination of electrons and holes in germanium," *Phys. Rev.*, vol. 94, no. 6, pp. 1558-1560, June 15, 1954.

2. M. Nathan, W. Dumke, G. Burns, F. Dill Jr. and G. Lasher, "STIMULATED EMISSION OF RADIATION FROM GaAs p□n JUNCTIONS," *Appl. Phys. Lett.*, vol. 1, no. 3, pp. 62-64, November 1, 1962.

3. I. Adawi, "Theory of the surface photoelectric effect for one and two photons," *Phys. Rev.*, vol. 134, no. 3A, pp. A798, May 4, 1964.

4. G. Eda and M. Chhowalla, "Chemically derived graphene oxide: Towards large-area thin-film electronics and optoelectronics," *Adv. Mater.*, vol. 22, no. 22, pp. 2392-2415, June 11, 2010.

5. S.R. Forrest, "Active optoelectronics using thin-film organic semiconductors," *IEEE Journal of Selected Topics in Quantum Electronics*, vol. 6, no. 6, pp. 1072-1083, November 2000.

6. J. Jin, J. Lee, S. Jeong, S. Yang, J. Ko, H. Im, S. Baek, J. Lee and B. Bae, "High-performance hybrid plastic films: A robust electrode platform for thin-film optoelectronics," *Energy & Environmental Science*, vol. 6, no. 6, pp. 1811-1817 2013.

7. L. Luo, D. Bozyigit, V. Wood and M. Niederberger, "High-quality transparent electrodes spin-cast from preformed antimony-doped tin oxide nanocrystals for thin film optoelectronics," *Chem. Mater.*, vol. 25, no. 24, pp. 4901-4907, December 23, 2013.

8. S. Chénais and S. Forget, "Recent advances in solid-state organic lasers," *Polym. Int.*, vol. 61, no. 3, pp. 390-406, March 1, 2012.

9. J. Clark and G. Lanzani, "Organic photonics for communications," *Nat Photon*, vol. 4, no. 7, pp. 438-446, July 2010.

10. S.R. Forrest and M.E. Thompson, "Introduction:□ Organic electronics and optoelectronics," *Chem. Rev.*, vol. 107, no. 4, pp. 923-925, April 1, 2007.

11. S. Günes, H. Neugebauer and N.S. Sariciftci, "Conjugated polymer-based organic solar cells," *Chem. Rev.*, vol. 107, no. 4, pp. 1324-1338, April 1, 2007.

12. N. Thejo Kalyani and S.J. Dhoble, "Organic light emitting diodes: Energy saving lighting technology—A review," *Renewable and Sustainable Energy Reviews*, vol. 16, no. 5, pp. 2696-2723, June 2012.

13. P.V. Kamat, "Quantum dot solar cells. semiconductor nanocrystals as light harvesters," *J. Phys. Chem. C*, vol. 112, no. 48, pp. 18737-18753, December 4, 2008.

14. S.A. McDonald, G. Konstantatos, S. Zhang, P.W. Cyr, E.J.D. Klem, L. Levina and E.H. Sargent, "Solution-processed PbS quantum dot infrared photodetectors and photovoltaics," *Nat Mater*, vol. 4, no. 2, pp. 138-142, February 2005.

15. Y. Shirasaki, G.J. Supran, M.G. Bawendi and V. Bulović, "Emergence of colloidal quantum-dot light-emitting technologies," *Nat Photon*, vol. 7, no. 1, pp. 13-23, January 2013.

16. E.U. Rafailov, M.A. Cataluna and W. Sibbett, "Mode-locked quantum-dot lasers," *Nat Photon*, vol. 1, no. 7, pp. 395-401, July 2007.

17. G. Konstantatos, I. Howard, A. Fischer, S. Hoogland, J. Clifford, E. Klem, L. Levina and E.H. Sargent, "Ultrasensitive solution-cast quantum dot photodetectors," *Nature*, vol. 442, no. 7099, pp. 180-183, July 13, 2006.

18. H.S. Jung and N. Park, "Perovskite solar cells: From materials to devices," *Small*, vol. 11, no. 1, pp. 10-25, January 1, 2015.

19. S.D. Stranks and H.J. Snaith, "Metal-halide perovskites for photovoltaic and light-emitting devices," *Nat Nano*, vol. 10, no. 5, pp. 391-402, May 2015.

20. B.R. Sutherland and E.H. Sargent, "Perovskite photonic sources," *Nat Photon*, vol. 10, no. 5, pp. 295-302, May 2016.

21. Q. Zhang, S.T. Ha, X. Liu, T.C. Sum and Q. Xiong, "Room-temperature near-infrared high-Q perovskite whispering-gallery planar nanolasers," *Nano Lett.*, vol. 14, no. 10, pp. 5995-6001, October 8, 2014.

22. B.R. Sutherland, A.K. Johnston, A.H. Ip, J. Xu, V. Adinolfi, P. Kanjanaboos and E.H. Sargent, "Sensitive, fast, and stable perovskite photodetectors exploiting interface engineering," *ACS Photonics*, vol. 2, no. 8, pp. 1117-1123, August 19, 2015.

23. M. Graetzel, R.A.J. Janssen, D.B. Mitzi and E.H. Sargent, "Materials interface engineering for solution-processed photovoltaics," *Nature*, vol. 488, no. 7411, pp. 304-312, August 16, 2012.

24. E.H. Sargent, "Colloidal quantum dot solar cells," *Nat Photon*, vol. 6, no. 3, pp. 133-135, March 2012.

25. D.A.R. Barkhouse, R. Debnath, I.J. Kramer, D. Zhitomirsky, A.G. Pattantyus-Abraham, L. Levina, L. Etgar, M. Grätzel and E.H. Sargent, "Depleted bulk heterojunction colloidal quantum dot photovoltaics," *Adv. Mater.*, vol. 23, no. 28, pp. 3134-3138, July 26, 2011.

26. A.H. Ip, S.M. Thon, S. Hoogland, O. Voznyy, D. Zhitomirsky, R. Debnath, L. Levina, L.R. Rollny, G.H. Carey, A. Fischer, K.W. Kemp, I.J. Kramer, Z. Ning, A.J. Labelle, K.W. Chou, A. Amassian and E.H. Sargent, "Hybrid passivated colloidal quantum dot solids," *Nat Nano*, vol. 7, no. 9, pp. 577-582, September 2012.

27. S. Keuleyan, E. Lhuillier, V. Brajuskovic and P. Guyot-Sionnest, "Mid-infrared HgTe colloidal quantum dot photodetectors," *Nat Photon*, vol. 5, no. 8, pp. 489-493, August 2011.

28. J.M. Caruge, J.E. Halpert, V. Wood, V. Bulović and M.G. Bawendi, "Colloidal quantum-dot light-emitting diodes with metal-oxide charge transport layers," *Nat Photon*, vol. 2, no. 4, pp. 247-250, April 2008.

29. I. Moreels, Y. Justo, B. De Geyter, K. Haustraete, J.C. Martins and Z. Hens, "Size-tunable, bright, and stable PbS quantum dots: A surface chemistry study," *ACS Nano*, vol. 5, no. 3, pp. 2004-2012, March 22, 2011.

30. K. Saxena, V.K. Jain and D.S. Mehta, "A review on the light extraction techniques in organic electroluminescent devices," *Optical Materials*, vol. 32, no. 1, pp. 221-233, November 2009.

31. S.r. Forrest, D.d.c. Bradley and M.e. Thompson, "Measuring the efficiency of organic light-emitting devices," *Adv. Mater.*, vol. 15, no. 13, pp. 1043-1048, July 4, 2003.

32. G. Li, R. Zhu and Y. Yang, "Polymer solar cells," *Nat Photon*, vol. 6, no. 3, pp. 153-161, March 2012.

33. A. Hagfeldt, G. Boschloo, L. Sun, L. Kloo and H. Pettersson, "Dye-sensitized solar cells," *Chem. Rev.*, vol. 110, no. 11, pp. 6595-6663, November 10, 2010.

34. M. Liu, M.B. Johnston and H.J. Snaith, "Efficient planar heterojunction perovskite solar cells by vapour deposition," *Nature*, vol. 501, no. 7467, pp. 395-398, September 19, 2013.

35. D. Zhitomirsky, O. Voznyy, L. Levina, S. Hoogland, K.W. Kemp, A.H. Ip, S.M. Thon and E.H. Sargent, "Engineering colloidal quantum dot solids within and beyond the mobility-invariant regime," *Nature Communications*, vol. 5, pp. 3803, -05-06 2014.

36. M.L. Brongersma, Y. Cui and S. Fan, "Light management for photovoltaics using high-index nanostructures," *Nat Mater*, vol. 13, no. 5, pp. 451-460, May 2014.

37. H.A. Atwater and A. Polman, "Plasmonics for improved photovoltaic devices," *Nat Mater*, vol. 9, no. 3, pp. 205-213, March 2010.

38. G.I. Koleilat, I.J. Kramer, C.T.O. Wong, S.M. Thon, A.J. Labelle, S. Hoogland and E.H. Sargent, "Folded-light-path colloidal quantum dot solar cells," *Scientific Reports*, vol. 3, pp. 2166, /07/09 2013.

39. A.J. Labelle, S.M. Thon, S. Masala, M.M. Adachi, H. Dong, M. Farahani, A.H. Ip, A. Fratalocchi and E.H. Sargent, "Colloidal quantum dot solar cells exploiting hierarchical structuring," *Nano Lett.*, vol. 15, no. 2, pp. 1101-1108, February 11, 2015.

40. S. Kim, J.K. Kim, J. Gao, J.H. Song, H.J. An, T. You, T. Lee, J. Jeong, E. Lee, J. Jeong, M.C. Beard and S. Jeong, "Lead sulfide nanocrystal quantum dot solar cells with trenched ZnO fabricated via nanoimprinting," *ACS Appl. Mater. Interfaces*, vol. 5, no. 9, pp. 3803-3808, May 8, 2013.

41. M.M. Adachi, A.J. Labelle, S.M. Thon, X. Lan, S. Hoogland and E.H. Sargent, "Broadband solar absorption enhancement via periodic nanostructuring of electrodes," *Scientific Reports*, vol. 3, pp. 2928, /10/14 2013.

42. N.K. Patel, S. Cina and J.H. Burroughes, "High-efficiency organic light-emitting diodes," *IEEE Journal of Selected Topics in Quantum Electronics*, vol. 8, no. 2, pp. 346-361, March 2002.

43. C.M. Tsai, J.K. Sheu, P.T. Wang, W.C. Lai, S.C. Shei, S.J. Chang, C.H. Kuo, C.W. Kuo and Y.K. Su, "High efficiency and improved ESD characteristics of GaN-based LEDs with naturally textured surface grown by MOCVD," *IEEE Photonics Technology Letters*, vol. 18, no. 11, pp. 1213-1215, June 2006.

44. W. Li, R.A. Jones, S.C. Allen, J.C. Heikenfeld and A.J. Steckl, "Maximizing alq/sub 3/ OLED internal and external efficiencies: Charge balanced device structure and color conversion outcoupling lenses," *Journal of Display Technology*, vol. 2, no. 2, pp. 143-152, June 2006.

45. M.M. Lu, C.F. Madigan and J.C. Sturm, "Experiment and modeling of conversion of substrate-waveguided modes to surface-emitted light by substrate patterning," *MRS Online Proceedings Library Archive*, vol. 621, /01 2000.

46. Yu-Hung Cheng, Jia-Lin Wu, Chien-Hong Cheng, Kao-Chih Syao and Ming-Chang M. Lee, "Enhanced light outcoupling in a thin film by texturing meshed surfaces," *Appl. Phys. Lett.*, vol. 90, no. 9, pp. 091102, February 26, 2007.

47. A.I. Zhmakin, "Enhancement of light extraction from light emitting diodes," *Physics Reports*, vol. 498, no. 4–5, pp. 189-241, February 2011.

48. M. Lee and K. Kuo, "Microlens array on sapphire substrate prepared by FIB to enhance electroluminescence of GaN/sapphire blue LED," *Electrochem. Solid-State Lett.*, vol. 10, no. 1, pp. H22, 01/01/ 2007.

49. H. Lin, Y. Ho, J. Lee, K. Chen, J. Fang, S. Hsu, M. Wei, H. Lin, J. Tsai and T. Wu, "Patterned microlens array for efficiency improvement of small-pixelated organic light-emitting devices," *Opt. Express, OE*, vol. 16, no. 15, pp. 11044-11051, /07/21 2008.

50. J.M. Ziebarth, A.K. Saafir, S. Fan and M.D. McGehee, "Extracting light from polymer light-emitting diodes using stamped bragg gratings," *Adv. Funct. Mater.*, vol. 14, no. 5, pp. 451-456, May 1, 2004.

51. P. T. Worthing and W. L. Barnes, "Efficient coupling of surface plasmon polaritons to radiation using a bi-grating," *Appl. Phys. Lett.*, vol. 79, no. 19, pp. 3035-3037, October 30, 2001.

52. L. Sun, W. Zhu, M. Tang, B. Qian, T. Xiao, J. Yu and K. Guo, "Effect of inverted-pyramid shape on light extraction of organic light-emitting diodes," *Phys. Status Solidi A*, vol. 212, no. 3, pp. 646-650, March 1, 2015.

53. W. Zhu, X. Wu, W. Sun, L. Sun, K. Guo, M. Tang and P. Zhou, "A simple effective method to improve light out-coupling in organic light-emitting diodes by introducing pyramid-based texture structure," *Organic Electronics*, vol. 15, no. 6, pp. 1113-1119, June 2014.

54. W.H. Koo, W. Youn, P. Zhu, X. Li, N. Tansu and F. So, "Light extraction of organic light emitting diodes by defective hexagonal-close-packed array," *Adv. Funct. Mater.*, vol. 22, no. 16, pp. 3454-3459, August 21, 2012.

55. T. Baba, "Slow light in photonic crystals," *Nat Photon*, vol. 2, no. 8, pp. 465-473, August 2008.

56. M. Fujita, T. Ueno, T. Asano, S. Noda, H. Ohhata, T. Tsuji, H. Nakada and N. Shimoji, "Organic light-emitting diode with ITO/organic photonic crystal," *Electronics Letters*, vol. 39, no. 24, pp. 1750-1752, November 2003.

57. Kuniaki Ishihara, Masayuki Fujita, Ippei Matsubara, Takashi Asano, Susumu Noda, Hiroshi Ohata, Akira Hirasawa, Hiroshi Nakada and Noriyuki Shimoji, "Organic light-emitting diodes with photonic crystals on glass substrate fabricated by nanoimprint lithography," *Appl. Phys. Lett.*, vol. 90, no. 11, pp. 111114, March 12, 2007.

58. M. Kwon, J. Kim, B. Kim, I. Park, C. Cho, C.C. Byeon and S. Park, "Surface-plasmon-enhanced light-emitting diodes," *Adv. Mater.*, vol. 20, no. 7, pp. 1253-1257, April 4, 2008.

59. Dawn K. Gifford and Dennis G. Hall, "Emission through one of two metal electrodes of an organic light-emitting diode via surface-plasmon cross coupling," *Appl. Phys. Lett.*, vol. 81, no. 23, pp. 4315-4317, November 25, 2002.

60. S. Baek, G. Kang, D. Shin, K. Bae, Y.H. Kim and K. Kim, "Improvement of light extraction efficiency in flip-chip light emitting diodes on SiC substrate via transparent haze films with morphology-controlled collapsed alumina nanorods," *ACS Appl. Mater. Interfaces*, vol. 8, no. 1, pp. 135-141, January 13, 2016.

61. C. Chen, W. Lee, Y. Chen, C. Lu, H.Y. Lin and C. Wu, "Enhancing optical out-coupling of organic light-emitting devices with nanostructured composite electrodes consisting of indium tin oxide nanomesh and conducting polymer," *Adv. Mater.*, vol. 27, no. 33, pp. 4883-4888, September 1, 2015.

62. W. Ding, Y. Wang, H. Chen and S.Y. Chou, "Plasmonic nanocavity organic light-emitting diode with significantly enhanced light extraction, contrast, viewing angle, brightness, and low-glare," *Adv. Funct. Mater.*, vol. 24, no. 40, pp. 6329-6339, October 1, 2014.

63. Y.H. Kim, J. Lee, W.M. Kim, C. Fuchs, S. Hofmann, H. Chang, M.C. Gather, L. Müller-Meskamp and K. Leo, "We want our photons back: Simple nanostructures for white organic light-emitting diode outcoupling," *Adv. Funct. Mater.*, vol. 24, no. 17, pp. 2553-2559, May 1, 2014.

64. W.H. Koo, S.M. Jeong, F. Araoka, K. Ishikawa, S. Nishimura, T. Toyooka and H. Takezoe, "Light extraction from organic light-emitting diodes enhanced by spontaneously formed buckles," *Nat Photon*, vol. 4, no. 4, pp. 222-226, April 2010.

65. W.H. Koo, W. Youn, P. Zhu, X. Li, N. Tansu and F. So, "Light extraction of organic light emitting diodes by defective hexagonal-close-packed array," *Adv. Funct. Mater.*, vol. 22, no. 16, pp. 3454-3459, August 21, 2012.

66. K. Lee, J. Shin, J. Park, J. Lee, C.W. Joo, J. Lee, D. Cho, J.T. Lim, M. Oh, B. Ju and J. Moon, "A light scattering layer for internal light extraction of organic light-emitting diodes based on silver nanowires," *ACS Appl. Mater. Interfaces*, vol. 8, no. 27, pp. 17409-17415, July 13, 2016.

67. Y. Leem, O. Seo, Y. Jo, J. Heon Kim, J. Chun, B. Kim, D. Young Noh, W. Lim, Y. Kim and S. Park, "Titanium oxide nanotube arrays for high light extraction efficiency of GaN-based vertical light-emitting diodes," *Nanoscale*, vol. 8, no. 19, pp. 10138-10144 2016.

68. L. Li, J. Liang, S. Chou, X. Zhu, X. Niu and Q. Pei, "A solution processed flexible nanocomposite electrode with efficient light extraction for organic light emitting diodes," *Scientific Reports*, vol. 4, pp. 4307, /03/17 2014.

69. P. Mao, A.k. Mahapatra, J. Chen, M. Chen, G. Wang and M. Han, "Fabrication of polystyrene/ZnO micronano hierarchical structure applied for light extraction of light-emitting devices," *ACS Appl. Mater. Interfaces*, vol. 7, no. 34, pp. 19179-19188, September 2, 2015.

70. Y. Moon, D. Moon, J. Jang, J. Na, J. Song, M. Seo, S. Kim, D. Bae, E.H. Park, Y. Park, S. Kim and E. Yoon, "Microstructured air cavities as high-index contrast substrates with strong diffraction for light-emitting diodes," *Nano Lett.*, vol. 16, no. 5, pp. 3301-3308, May 11, 2016.

71. B. Pyo, C. Woong Joo, H. Suk Kim, B. Kwon, J. Lee, J. Lee and M. Chul Suh, "A nanoporous polymer film as a diffuser as well as a light extraction component for top emitting organic light emitting diodes with a strong microcavity structure," *Nanoscale*, vol. 8, no. 16, pp. 8575-8582 2016.

72. Y. Qu, M. Slootsky and S.R. Forrest, "Enhanced light extraction from organic light-emitting devices using a sub-anode grid," *Nat Photon*, vol. 9, no. 11, pp. 758-763, November 2015.

73. L. Xu, Q. Ou, Y. Li, Y. Zhang, X. Zhao, H. Xiang, J. Chen, L. Zhou, S. Lee and J. Tang, "Microcavity-free broadband light outcoupling enhancement in flexible organic light-emitting diodes with nanostructured transparent Metal–Dielectric composite electrodes," *ACS Nano*, vol. 10, no. 1, pp. 1625-1632, January 26, 2016.

74. X. Yang, K. Dev, J. Wang, E. Mutlugun, C. Dang, Y. Zhao, S. Liu, Y. Tang, S.T. Tan, X.W. Sun and H.V. Demir, "Light extraction efficiency enhancement of colloidal quantum dot light-emitting diodes using large-scale nanopillar arrays," *Adv. Funct. Mater.*, vol. 24, no. 38, pp. 5977-5984, October 1, 2014.

75. W. Youn, J. Lee, M. Xu, R. Singh and F. So, "Corrugated sapphire substrates for organic light-emitting diode light extraction," *ACS Appl. Mater. Interfaces*, vol. 7, no. 17, pp. 8974-8978, May 6, 2015.

76. J. Kim, J. Lee, C. Moon, S. Kim and J. Kim, "Highly enhanced light extraction from surface plasmonic loss minimized organic light-emitting diodes," *Adv. Mater.*, vol. 25, no. 26, pp. 3571-3577, July 12, 2013.

77. Shen-Yu Hsu, Ming-Chang Lee, Kuang-Li Lee and Pei-Kuen Wei, "Extraction enhancement in organic light emitting devices by using metallic nanowire arrays," *Appl. Phys. Lett.*, vol. 92, no. 1, pp. 013303, January 4, 2008.

78. Changjun Min, Jennifer Li, Georgios Veronis, Jung-Yong Lee, Shanhui Fan and Peter Peumans, "Enhancement of optical absorption in thin-film organic solar cells through the excitation of plasmonic modes in metallic gratings," *Appl. Phys. Lett.*, vol. 96, no. 13, pp. 133302, March 29, 2010.

79. I. Ding, J. Zhu, W. Cai, S. Moon, N. Cai, P. Wang, S.M. Zakeeruddin, M. Grätzel, M.L. Brongersma, Y. Cui and M.D. McGehee, "Plasmonic dye-sensitized solar cells," *Adv. Energy Mater.*, vol. 1, no. 1, pp. 52-57, January 1, 2011.

80. A. Raman, Z. Yu and S. Fan, "Dielectric nanostructures for broadband light trapping in organic solar cells," *Opt. Express, OE*, vol. 19, no. 20, pp. 19015-19026, /09/26 2011.

81. Yu. A. Akimov, W. S. Koh, S. Y. Sian and S. Ren, "Nanoparticle-enhanced thin film solar cells: Metallic or dielectric nanoparticles?" *Appl. Phys. Lett.*, vol. 96, no. 7, pp. 073111, February 15, 2010.

82. A.G. Pattantyus-Abraham, I.J. Kramer, A.R. Barkhouse, X. Wang, G. Konstantatos, R. Debnath, L. Levina, I. Raabe, M.K. Nazeeruddin, M. Grätzel and E.H. Sargent, "Depleted-heterojunction colloidal quantum dot solar cells," *ACS Nano*, vol. 4, no. 6, pp. 3374-3380, June 22, 2010.

83. S.M. Mahpeykar, Q. Xiong and X. Wang, "Resonance-induced absorption enhancement in colloidal quantum dot solar cells using nanostructured electrodes," *Opt. Express, OE*, vol. 22, no. 106, pp. A1588, /10/20 2014.

84. Anonymous *SOPRA refractive index database* [Online]. available: http://www.sopra-sa.com.

85. E. Palik, *Handbook of Optical Constants of Solids*, Academic Press, 1998.

86. R.A. Synowicki, "Spectroscopic ellipsometry characterization of indium tin oxide film microstructure and optical constants," *Thin Solid Films*, vol. 313–314, pp. 394-397, February 13, 1998.

87. X. Wang, G.I. Koleilat, J. Tang, H. Liu, I.J. Kramer, R. Debnath, L. Brzozowski, D.A.R. Barkhouse, L. Levina, S. Hoogland and E.H. Sargent, "Tandem colloidal quantum dot solar cells employing a graded recombination layer," *Nat Photon*, vol. 5, no. 8, pp. 480-484, August 2011.

88. Anonymous *Reference Solar Spectral Irradiance: ASTM G-173* [Online]. available: http://rredc.nrel.gov/solar/spectra/am1.5/ASTMG173/ASTMG173.html.

89. Arquer, F Pelayo García de, F.J. Beck and G. Konstantatos, "Absorption enhancement in solution processed metal-semiconductor nanocomposites," *Opt. Express, OE*, vol. 19, no. 21, pp. 21038-21049, /10/10 2011.

90. Anonymous *Grating projections* [Online]. available: http://docs.lumerical.com/en/solvers_grating_projections.html.

91. A. Abass, K.Q. Le, A. Alù, M. Burgelman and B. Maes, "Dual-interface gratings for broadband absorption enhancement in thin-film solar cells," *Phys. Rev. B*, vol. 85, no. 11, pp. 115449, March 30, 2012.

92. A.L. Beaudry, R.T. Tucker, J.M. LaForge, M.T. Taschuk and M.J. Brett, "Indium tin oxide nanowhisker morphology control by vapour–liquid–solid glancing angle deposition," *Nanotechnology*, vol. 23, no. 10, pp. 105608 2012.

93. A.L. Beaudry, J.M. LaForge, R.T. Tucker, P. Li, M.T. Taschuk and M.J. Brett, "Flux engineering for indium tin oxide nanotree crystal alignment and height-dependent branch orientation," *Crystal Growth & Design*, vol. 13, no. 1, pp. 212-219, January 2, 2013.

94. A.L. Beaudry, J.M. LaForge, R.T. Tucker, J.B. Sorge, N.L. Adamski, P. Li, M.T. Taschuk and M.J. Brett, "Directed branch growth in aligned nanowire arrays," *Nano Lett.*, vol. 14, no. 4, pp. 1797-1803, April 9, 2014.

95. G. Kim, "A PMMA composite as an optical diffuser in a liquid crystal display backlighting unit (BLU)," *European Polymer Journal*, vol. 41, no. 8, pp. 1729-1737, August 2005.

96. H.P. Kuo, M.Y. Chuang and C.C. Lin, "Design correlations for the optical performance of the particle-diffusing bottom diffusers in the LCD backlight unit," *Powder Technology*, vol. 192, no. 1, pp. 116-121, May 15, 2009.

97. L. Mingyan, W. Daming, Z. Yajun and Z. Jian, "Optimization and design of LCD diffuser plate with micro-semisphere structure," *Procedia Engineering*, vol. 16, pp. 306-311, January 1, 2011.

98. S.G. Lee, D.Y. Lee, H.S. Lim, D.H. Lee, S. Lee and K. Cho, "Switchable transparency and wetting of elastomeric smart windows," *Adv. Mater.*, vol. 22, no. 44, pp. 5013-5017, November 24, 2010.

99. J. Parra-Barranco, M. Oliva-Ramirez, L. Gonzalez-Garcia, M. Alcaire, M. Macias-Montero, A. Borras, F. Frutos, A.R. Gonzalez-Elipe and A. Barranco, "Bending induced self-organized switchable gratings on polymeric substrates," *ACS Appl. Mater. Interfaces*, vol. 6, no. 15, pp. 11924-11931, August 13, 2014.

100. Z. Fang, H. Zhu, Y. Yuan, D. Ha, S. Zhu, C. Preston, Q. Chen, Y. Li, X. Han, S. Lee, G. Chen, T. Li, J. Munday, J. Huang and L. Hu, "Novel nanostructured paper with ultrahigh transparency and ultrahigh haze for solar cells," *Nano Lett.*, vol. 14, no. 2, pp. 765-773, February 12, 2014.

101. W. Bin and W. Qing-Kang, "High sensitivity transmission-type SPR sensor by using Metallic–Dielectric mixed gratings," *Chinese Phys. Lett.*, vol. 25, no. 5, pp. 1668 2008.

102. X. Zhang, Y. Huang, X. Ren, H. Huang and Q. Wang, "Flat-top steep-edge photodetector with cascaded grating structure," *Appl. Opt., AO*, vol. 48, no. 35, pp. 6760-6764, /12/10 2009.

103. X. Duan, Y. Huang, X. Ren, Y. Shang, X. Fan and F. Hu, "High-efficiency InGaAs/InP photodetector incorporating SOI-based concentric circular subwavelength gratings," *IEEE Photonics Technology Letters*, vol. 24, no. 10, pp. 863-865, May 2012.

104. C. Chen, W. Lee, Y. Chen, C. Lu, H.Y. Lin and C. Wu, "Enhancing optical out-coupling of organic light-emitting devices with nanostructured composite electrodes consisting of indium tin oxide nanomesh and conducting polymer," *Adv. Mater.*, vol. 27, no. 33, pp. 4883-4888, September 1, 2015.

105. X. Yang, K. Dev, J. Wang, E. Mutlugun, C. Dang, Y. Zhao, S. Liu, Y. Tang, S.T. Tan, X.W. Sun and H.V. Demir, "Light extraction efficiency enhancement of colloidal quantum dot light-

emitting diodes using large-scale nanopillar arrays," *Adv. Funct. Mater.*, vol. 24, no. 38, pp. 5977-5984, October 1, 2014.

106. L. Zhou, X. Dong, Y. Zhou, W. Su, X. Chen, Y. Zhu and S. Shen, "Multiscale Micro–Nano nested structures: Engineered surface morphology for efficient light escaping in organic light-emitting diodes," *ACS Appl. Mater. Interfaces*, vol. 7, no. 48, pp. 26989-26998, December 9, 2015.

107. J. Hu, Y. Zhou and X. Sheng, "Hydrothermal synthesis of ZnO@polysiloxane microspheres and their application in preparing optical diffusers," *RSC Adv.*, vol. 5, no. 22, pp. 17064-17069, /02/05 2015.

108. J. Hu, Y. Zhou and X. Sheng, "Optical diffusers with enhanced properties based on novel polysiloxane@CeO2@PMMA fillers," *J. Mater. Chem. C*, vol. 3, no. 10, pp. 2223-2230, /02/26 2015.

109. W. Suthabanditpong, M. Tani, C. Takai, M. Fuji, R. Buntem and T. Shirai, "Facile fabrication of light diffuser films based on hollow silica nanoparticles as fillers," *Advanced Powder Technology*, vol. 27, no. 2, pp. 454-460, March 2016.

110. T. Huang, J. Ciou, P. Huang, K. Hsieh and S. Yang, "Fast fabrication of integrated surface-relief and particle-diffusing plastic diffuser by use of a hybrid extrusion roller embossing process," *Opt. Express, OE*, vol. 16, no. 1, pp. 440-447, /01/07 2008.

111. S. Liu and Y. Huang, "Manufacture of dual-side surface-relief diffusers with various cross angles using ultrasonic embossing technique," *Opt. Express, OE*, vol. 17, no. 20, pp. 18083-18092, /09/28 2009.

112. P. Gutruf, E. Zeller, S. Walia, S. Sriram and M. Bhaskaran, "Mechanically tunable high refractive-index contrast TiO2–PDMS gratings," *Advanced Optical Materials*, vol. 3, no. 11, pp. 1565-1569, November 1, 2015.

113. T. Ohzono, K. Suzuki, T. Yamaguchi and N. Fukuda, "Tunable optical diffuser based on deformable wrinkles," *Advanced Optical Materials*, vol. 1, no. 5, pp. 374-380, May 1, 2013.

114. A. Ryabchun, M. Wegener, Y. Gritsai and O. Sakhno, "Novel effective approach for the fabrication of PDMS-based elastic volume gratings," *Advanced Optical Materials*, vol. 4, no. 1, pp. 169-176, January 1, 2016.

115. L.T. Su, S.K. Karuturi, J. Luo, L. Liu, X. Liu, J. Guo, T.C. Sum, R. Deng, H.J. Fan, X. Liu and A.I.Y. Tok, "Photon upconversion in hetero-nanostructured photoanodes for enhanced near-infrared light harvesting," *Adv. Mater.*, vol. 25, no. 11, pp. 1603-1607, March 20, 2013.

116. P. Tseng, M. Tsai, P. Yu and H. Kuo, "Antireflection and light trapping of subwavelength surface structures formed by colloidal lithography on thin film solar cells," *Prog. Photovolt: Res. Appl.*, vol. 20, no. 2, pp. 135-142, March 1, 2012.

117. B. Wu, T.Z. Oo, X. Li, X. Liu, X. Wu, E.K.L. Yeow, H.J. Fan, N. Mathews and T.C. Sum, "Efficiency enhancement in bulk-heterojunction solar cells integrated with large-area ag nanotriangle arrays," *J. Phys. Chem. C*, vol. 116, no. 28, pp. 14820-14825, July 19, 2012.

118. S. Yang, S.G. Jang, D. Choi, S. Kim and H.K. Yu, "Nanomachining by colloidal lithography," *Small*, vol. 2, no. 4, pp. 458-475, April 1, 2006.

119. N. Lauinger, M. Pinnow and E. Görnitz, "Phase grating from ordered polymer lattices for optica image preprocessing," *Journal of Biological Physics*, vol. 23, no. 2, pp. 73-88, /06/01 1997.

120. Z. Qi, N. Pei-Gen, M. Qing-Bo, C. Bing-Ying and Z. Dao-Zhong, "Tow-dimensional micro-grating formed by polystyrene spheres," *Chinese Phys. Lett.*, vol. 20, no. 8, pp. 1290 2003.

121. A.-. Fehrembach, O. Gauthier-Lafaye, K.C.S. Yu, A. Monmayrant, S. Bonnefont, E. Daran, P. Arguel, F. Lozes-Dupuy and A. Sentenac, "Measurement and modeling of 2D hexagonal resonant-grating filter performance," *J. Opt. Soc. Am. A, JOSAA*, vol. 27, no. 7, pp. 1535-1540, /07/01 2010.

122. K. Iwata, F. Kusunoki, K. Moriwaki, H. Fukuda and T. Tomii, "Three-dimensional profiling using the fourier transform method with a hexagonal grating projection," *Appl. Opt., AO*, vol. 47, no. 12, pp. 2103-2108, /04/20 2008.

123. Matthew J. Lockyear, Alastair P. Hibbins and J. Roy Sambles, "Low angular-dispersion microwave absorption of a metal dual-period nondiffracting hexagonal grating," *Appl. Phys. Lett.*, vol. 86, no. 18, pp. 184103, April 26, 2005.

124. P. Xi, C. Zhou, E. Dai and L. Liu, "Generation of near-field hexagonal array illumination with a phase grating," *Opt. Lett., OL*, vol. 27, no. 4, pp. 228-230, /02/15 2002.

125. B. Wang, T. Gao and P. W Leu, "Broadband light absorption enhancement in ultrathin film crystalline silicon solar cells with high index of refraction nanosphere arrays," *Nano Energy*, vol. 19, pp. 471-475, January 2016.

126. X. Yan, J. Yao, G. Lu, X. Li, J. Zhang, K. Han and B. Yang, "Fabrication of non-close-packed arrays of colloidal spheres by soft lithography," *J. Am. Chem. Soc.*, vol. 127, no. 21, pp. 7688-7689, June 1, 2005.

127. Z. Zhao, Y. Cai, W. Liao and P.S. Cremer, "Stepwise molding, etching, and imprinting to form libraries of nanopatterned substrates," *Langmuir*, vol. 29, no. 22, pp. 6737-6745, June 4, 2013.

128. J. Yu, C. Geng, L. Zheng, Z. Ma, T. Tan, X. Wang, Q. Yan and D. Shen, "Preparation of high-quality colloidal mask for nanosphere lithography by a combination of air/water interface self-assembly and solvent vapor annealing," *Langmuir*, vol. 28, no. 34, pp. 12681-12689, August 28, 2012.

129. D.K. Cai, A. Neyer, R. Kuckuk and H.M. Heise, "Estimation of absorption loss in siloxane-based materials implemented as passive optical interconnects," in , March 2007, pp. 1-3.

130. N. Sultanova, S. Kasarova and I. Nikolov, "Dispersion properties of optical polymers," *Acta Phys. Pol. A*, vol. 116, no. 4, pp. 585-587, OCT 2009.

131. A.H. Ip, S.M. Thon, S. Hoogland, O. Voznyy, D. Zhitomirsky, R. Debnath, L. Levina, L.R. Rollny, G.H. Carey, A. Fischer, K.W. Kemp, I.J. Kramer, Z. Ning, A.J. Labelle, K.W. Chou, A. Amassian and E.H. Sargent, "Hybrid passivated colloidal quantum dot solids," *Nat Nano*, vol. 7, no. 9, pp. 577-582, September 2012.

132. S.M. Mahpeykar, Q. Xiong, J. Wei, L. Meng, B.K. Russell, P. Hermansen, A.V. Singhal and X. Wang, "Stretchable hexagonal diffraction gratings as optical diffusers for in situ tunable broadband photon management," *Advanced Optical Materials*, vol. 4, no. 7, pp. 1106-1114, July 1, 2016.

133. A. Oskooi, P.A. Favuzzi, Y. Tanaka, H. Shigeta, Y. Kawakami and S. Noda, "Partially disordered photonic-crystal thin films for enhanced and robust photovoltaics," *Appl. Phys. Lett.*, vol. 100, no. 18, pp. 181110, APR 30 2012.

134. C. Brückner, T. Käsebier, B. Pradarutti, S. Riehemann, G. Notni, E. Kley and A. Tünnermann, "Broadband antireflective structures applied to high resistive float zone silicon in the THz spectral range," *Opt. Express, OE*, vol. 17, no. 5, pp. 3063-3077, /03/02 2009.

135. J. Grandidier, D.M. Callahan, J.N. Munday and H.A. Atwater, "Light absorption enhancement in thin-film solar cells using whispering gallery modes in dielectric nanospheres," *Adv. Mater.*, vol. 23, no. 10, pp. 1272-1276, March 11, 2011.

136. I.D. Johnston, D.K. McCluskey, C.K.L. Tan and M.C. Tracey, "Mechanical characterization of bulk sylgard 184 for microfluidics and microengineering," *J. Micromech. Microeng.*, vol. 24, no. 3, pp. 035017 2014.

137. X. Meng and D. Qiu, "Gas-flow-induced reorientation to centimeter-sized two-dimensional colloidal single crystal of polystyrene particle," *Langmuir*, vol. 30, no. 11, pp. 3019-3023, March 25, 2014.

138. P. Gao, J. He, S. Zhou, X. Yang, S. Li, J. Sheng, D. Wang, T. Yu, J. Ye and Y. Cui, "Large-area nanosphere self-assembly by a micro-propulsive injection method for high throughput periodic surface nanotexturing," *Nano Lett.*, vol. 15, no. 7, pp. 4591-4598, July 8, 2015.

139. M.A. Green, A. Ho-Baillie and H.J. Snaith, "The emergence of perovskite solar cells," *Nat Photon*, vol. 8, no. 7, pp. 506-514, July 2014.

140. O.E. Semonin, J.M. Luther, S. Choi, H. Chen, J. Gao, A.J. Nozik and M.C. Beard, "Peak external photocurrent quantum efficiency exceeding 100% via MEG in a quantum dot solar cell," *Science*, vol. 334, no. 6062, pp. 1530-1533, Dec 16, 2011.

141. C.M. Chuang, P.R. Brown, V. Bulović and M.G. Bawendi, "Improved performance and stability in quantum dot solar cells through band alignment engineering," *Nat Mater*, vol. 13, no. 8, pp. 796-801, August 2014.

142. Z. Ning, O. Voznyy, J. Pan, S. Hoogland, V. Adinolfi, J. Xu, M. Li, A.R. Kirmani, J. Sun, J. Minor, K.W. Kemp, H. Dong, L. Rollny, A. Labelle, G. Carey, B. Sutherland, I. Hill, A. Amassian, H. Liu, J. Tang, O.M. Bakr and E.H. Sargent, "Air-stable n-type colloidal quantum dot solids," *Nat Mater*, vol. 13, no. 8, pp. 822-828, August 2014.

143. S.M. Mahpeykar and X. Wang, "Optoelectronic engineering of colloidal quantum-dot solar cells beyond the efficiency black hole: a modeling approach," in , 2017, pp. 10.

144. G.F. Burkhard, E.T. Hoke and M.D. McGehee, "Accounting for interference, scattering, and electrode absorption to make accurate internal quantum efficiency measurements in organic and other thin solar cells," *Adv. Mater.*, vol. 22, no. 30, pp. 3293-3297, August 10, 2010.

145. G. Kim, B. Walker, H. Kim, J.Y. Kim, E.H. Sargent, J. Park and J.Y. Kim, "Inverted colloidal quantum dot solar cells," *Adv. Mater.*, vol. 26, no. 20, pp. 3321-3327, May 1, 2014.

146. J.E. Cotter, "Optical intensity of light in layers of silicon with rear diffuse reflectors," *Journal of Applied Physics*, vol. 84, pp. 618-624, July 1, 1998.

147. T. Quast, R. Bellmann, B. Winter, J. Gatzke and I. V. Hertel, "Excited-state photoemission with combined laser/synchrotron pulse excitation from C60 chemisorbed on ni(110)," *Journal of Applied Physics*, vol. 83, no. 3, pp. 1642-1648, February 1, 1998.

148. M. G. Helander, M. T. Greiner, Z. B. Wang, W. M. Tang and Z. H. Lu, "Work function of fluorine doped tin oxide," *Journal of Vacuum Science & Technology A: Vacuum, Surfaces, and Films*, vol. 29, no. 1, pp. 011019, January 1, 2011.

149. J. Tang, H. Liu, D. Zhitomirsky, S. Hoogland, X. Wang, M. Furukawa, L. Levina and E.H. Sargent, "Quantum junction solar cells," *Nano Lett.*, vol. 12, no. 9, pp. 4889-4894, September 12, 2012.

150. J.P. Clifford, K.W. Johnston, L. Levina and E.H. Sargent, "Schottky barriers to colloidal quantum dot films," *Appl. Phys. Lett.*, vol. 91, no. 25, pp. 253117, DEC 17 2007.

151. W. Martienssen, *Springer handbook of condensed matter and materials data*. Berlin [u.a.], Springer, 2005.

152. W. Setyawan, R.M. Gaume, S. Lam, R.S. Feigelson and S. Curtarolo, "High-throughput combinatorial database of electronic band structures for inorganic scintillator materials," *ACS Comb. Sci.*, vol. 13, no. 4, pp. 382-390, July 11, 2011.

153. J. Yan, P. Gorai, B. Ortiz, S. Miller, S. A. Barnett, T. Mason, V. Stevanović and E. S. Toberer, "Material descriptors for predicting thermoelectric performance," *Energy & Environmental Science*, vol. 8, no. 3, pp. 983-994 2015.

154. R. Debnath, M.T. Greiner, I.J. Kramer, A. Fischer, J. Tang, D.A.R. Barkhouse, X. Wang, L. Levina, Z. Lu and E.H. Sargent, "Depleted-heterojunction colloidal quantum dot photovoltaics employing low-cost electrical contacts," *Appl. Phys. Lett.*, vol. 97, no. 2, pp. 023109, JUL 12 2010.

155. G.H. Kim, W.J. Kim, S.M. Kim and J.G. Son, "Analysis of thermo-physical and optical properties of a diffuser using PET/PC/PBT copolymer in LCD backlight units," *Displays*, vol. 26, no. 1, pp. 37-43, January 2005.

156. H.P. Kuo, M.Y. Chuang and C.C. Lin, "Design correlations for the optical performance of the particle-diffusing bottom diffusers in the LCD backlight unit," *Powder Technology*, vol. 192, no. 1, pp. 116-121, May 15, 2009.

157. L. Mingyan, W. Daming, Z. Yajun and Z. Jian, "Optimization and design of LCD diffuser plate with micro-semisphere structure," *Procedia Engineering*, vol. 16, pp. 306-311, January 1, 2011.

158. T. Huang, J. Ciou, P. Huang, K. Hsieh and S. Yang, "Fast fabrication of integrated surface-relief and particle-diffusing plastic diffuser by use of a hybrid extrusion roller embossing process," *Opt. Express, OE*, vol. 16, no. 1, pp. 440-447, /01/07 2008.

159. S. Liu and Y. Huang, "Manufacture of dual-side surface-relief diffusers with various cross angles using ultrasonic embossing technique," *Opt. Express, OE*, vol. 17, no. 20, pp. 18083-18092, /09/28 2009.

160. J. Wang, S. Lien, J. Ho, T. Shih, C. Chen, C. Chen and W. Whang, "Optical diffusers based on silicone emulsions," *Optical Materials*, vol. 32, no. 2, pp. 374-377, December 2009.

161. J. Hu, Y. Zhou and X. Sheng, "Hydrothermal synthesis of ZnO@polysiloxane microspheres and their application in preparing optical diffusers," *RSC Advances*, vol. 5, no. 22, pp. 17064-17069 2015.

162. J. Hu, Y. Zhou and X. Sheng, "Optical diffusers with enhanced properties based on novel polysiloxane@CeO 2 @PMMA fillers," *Journal of Materials Chemistry C*, vol. 3, no. 10, pp. 2223-2230 2015.

163. J. Hu, Y. Zhou, M. Wang, M. Yang and G. Yan, "Optical diffusers based on the novel fillers of polysiloxane@boehmite core–shell microspheres," *Materials Letters*, vol. 165, pp. 107-110, February 15, 2016.

164. K.M. Knowles, H. Butt, A. Batal, A. Sabouri and C.J. Anthony, "Light scattering and optical diffusion from willemite spherulites," *Optical Materials*, vol. 52, pp. 163-172, February 2016.

165. W. Suthabanditpong, M. Tani, C. Takai, M. Fuji, R. Buntem and T. Shirai, "Facile fabrication of light diffuser films based on hollow silica nanoparticles as fillers," *Advanced Powder Technology*, vol. 27, no. 2, pp. 454-460, March 2016.

166. W. Suthabanditpong, C. Takai, M. Fuji, R. Buntem and T. Shirai, "Improved optical properties of silica/UV-cured polymer composite films made of hollow silica nanoparticles with a hierarchical structure for light diffuser film applications," *Physical Chemistry Chemical Physics*, vol. 18, no. 24, pp. 16293-16301 2016.

167. S. Ahn and G. Kim, "An electrosprayed coating process for fabricating hemispherical PMMA droplets for an optical diffuser," *Appl. Phys. A*, vol. 97, no. 1, pp. 125-131, /10/01 2009.

168. S. Song, Y. Sun, Y. Lin and B. You, "A facile fabrication of light diffusing film with LDP/polyacrylates composites coating for anti-glare LED application," *Applied Surface Science*, vol. 273, pp. 652-660, May 15, 2013.

169. J. Hu, Y. Zhou and T. Zhang, "The novel optical diffusers based on the fillers of boehmite hollow microspheres," *Materials Letters*, vol. 136, pp. 114-117, December 1, 2014.

170. X. Sun, N. Li, J. Hang, L. Jin, L. Shi, Z. Cheng and D. Shang, "Nano-silica reinforced hybrid light-diffusing films with enhanced mechanical and thermal properties," *Optica Applicata*, vol. Vol. 45, no. nr 3 2015.

171. K. Shin, H. Kim, J. Cho, S.J. Moon, J.W. Kim and K. Suh, "Fabrication of monodisperse polymer/silica hybrid microparticles for improving light diffusion properties," *Macromol. Res.*, vol. 20, no. 4, pp. 385-390, /04/01 2012.

172. J. George and S.N. Sabapathi, "Cellulose nanocrystals: Synthesis, functional properties, and applications," *Nanotechnology, Science and Applications*, vol. 8, pp. 45 2015. /pmcc/articles/PMC4639556/?report=abstract.

173. D. Klemm, F. Kramer, S. Moritz, T. Lindström, M. Ankerfors, D. Gray and A. Dorris, "Nanocelluloses: A new family of nature-based materials," *Angew. Chem. Int. Ed.*, vol. 50, no. 24, pp. 5438-5466, June 6, 2011.

174. L. Meng, S. Milad Mahpeykar, Q. Xiong, B. Ahvazi and X. Wang, "Strain sensors on water-soluble cellulose nanofibril paper by polydimethylsiloxane (PDMS) stencil lithography," *RSC Advances*, vol. 6, no. 88, pp. 85427-85433 2016.

175. M. Nogi, M. Karakawa, N. Komoda, H. Yagyu and T.T. Nge, "Transparent conductive nanofiber paper for foldable solar cells," *Sci Rep*, vol. 5, -11-26 2015.

176. E. Najafabadi, Y.H. Zhou, K.A. Knauer, C. Fuentes-Hernandez and B. Kippelen, "Efficient organic light-emitting diodes fabricated on cellulose nanocrystal substrates," *Appl. Phys. Lett.*, vol. 105, no. 6, pp. 063305, AUG 11 2014.

177. C. Wang, C. Fuentes-Hernandez, J. Liu, A. Dindar, S. Choi, J.P. Youngblood, R.J. Moon and B. Kippelen, "Stable low-voltage operation top-gate organic field-effect transistors on cellulose nanocrystal substrates," *ACS Appl. Mater. Interfaces*, vol. 7, no. 8, pp. 4804-4808, March 4, 2015.

178. H. Zhu, S. Parvinian, C. Preston, O. Vaaland, Z. Ruan and L. Hu, "Transparent nanopaper with tailored optical properties," *Nanoscale*, vol. 5, no. 9, pp. 3787-3792 2013.

179. W. Wu, N.G. Tassi, H. Zhu, Z. Fang and L. Hu, "Nanocellulose-based translucent diffuser for optoelectronic device applications with dramatic improvement of light coupling," *ACS Appl. Mater. Interfaces*, vol. 7, no. 48, pp. 26860-26864, December 9, 2015.

180. A.J. Svagan, A. Musyanovych, M. Kappl, M. Bernhardt, G. Glasser, C. Wohnhaas, L.A. Berglund, J. Risbo and K. Landfester, "Cellulose nanofiber/nanocrystal reinforced capsules: A fast and facile approach toward assembly of liquid-core capsules with high mechanical stability," *Biomacromolecules*, vol. 15, no. 5, pp. 1852, May 12, 2014.

181. Y. Boluk and C. Danumah, "Analysis of cellulose nanocrystal rod lengths by dynamic light scattering and electron microscopy," *J Nanopart Res*, vol. 16, no. 1, pp. 2174, /01/01 2014.

182. W.Y. Hamad and T.Q. Hu, "Structure–process–yield interrelations in nanocrystalline cellulose extraction," *Can. J. Chem. Eng.*, vol. 88, no. 3, pp. 392-402, June 1, 2010.

183. Y. Chen, D. Ma, H. Sun, J. Chen, Q. Guo, Q. Wang and Y. Zhao, "Organic semiconductor heterojunctions: Electrode-independent charge injectors for high-performance organic light-emitting diodes," *Light Sci Appl*, vol. 5, no. 3, pp. e16042, March 11, 2016.

184. H. Yano, J. Sugiyama, A.N. Nakagaito, M. Nogi, T. Matsuura, M. Hikita and K. Handa, "Optically transparent composites reinforced with networks of bacterial nanofibers," *Adv. Mater.*, vol. 17, no. 2, pp. 153-155, January 31, 2005.

185. S. Lee, H. Shin, S. Yoon, D. Kee Yi, J. Choi and U. Paik, "Refractive index engineering of transparent ZrO 2 –polydimethylsiloxane nanocomposites," *Journal of Materials Chemistry*, vol. 18, no. 15, pp. 1751-1755 2008.

186. S. Guo, S. Zhou, H. Li and B. You, "Light diffusing films fabricated by strawberry-like PMMA/SiO2 composite microspheres for LED application," *Journal of Colloid and Interface Science*, vol. 448, pp. 123-129, June 15, 2015.

187. R. Meerheim, M. Furno, S. Hofmann, B. Luessem and K. Leo, "Quantification of energy loss mechanisms in organic light-emitting diodes," *Appl. Phys. Lett.*, vol. 97, no. 25, pp. 253305, DEC 20 2010.

188. Y. Xing, P. Han, S. Wang, Y. Fan, P. Liang, Z. Ye, X. Li, S. Hu, S. Lou, C. Zhao and Y. Mi, "Performance analysis of vertical multi-junction solar cell with front surface diffusion for high concentration," *Solar Energy*, vol. 94, pp. 8-18, August 2013.

189. S. M. Mahpeykar, Y. Zhao, X. Li., Z. Yang, Q. Xu, Z. Lu, E. H. Sargent and X. Wang "Cellulose nanocrystal:polymer hybrid optical diffusers for index-matching-free light management in optoelectronic devices," *Advanced Optical Materials* 1700430, August 2017 (Early view)

Appendix A

Finite-difference time-domain (FDTD) basic theory

The FDTD method is based on discretizing the Maxwell's equation in time and space using central difference approximations. The theory can be simply explained by considering a basic one-dimensional problem and free space as the electromagnetic propagation medium. As such, the Maxwell's equations can be written as:

$$\frac{\partial E}{\partial t} = \frac{\nabla \times H}{\varepsilon_o} \tag{A-1}$$

$$\frac{\partial H}{\partial t} = \frac{\nabla \times E}{-\mu_o} \tag{A-2}$$

Which can be converted to the following form in one-dimensional case for a plane wave propagating in the z direction:

$$\frac{\partial E_x}{\partial t} = \frac{\partial H_y}{-\varepsilon_o \partial z} \tag{A-3}$$

$$\frac{\partial H_y}{\partial t} = \frac{\partial E_x}{-\mu_o \partial z} \tag{A-4}$$

As illustrated in figure A-1, the area of interest can be divided into cells forming a mesh grid and Ex and Hy are shifted in space by half a cell and in time by half a time step while considering a central difference approximation of the derivatives in the above equations. In this case, equations A-3 and A-4 can be written as:

$$\frac{E_x^{n+\frac{1}{2}}(k) - E_x^{n-\frac{1}{2}}(k)}{\Delta t} = \frac{H_y^n(k+\frac{1}{2}) - H_y^n(k-\frac{1}{2})}{-\varepsilon_o \Delta z} \tag{A-5}$$

$$\frac{H_y^{n+1}(k+\frac{1}{2}) - H_y^n(k+\frac{1}{2})}{\Delta t} = \frac{E_x^{n+\frac{1}{2}}(k+1) - E_x^{n+\frac{1}{2}}(k)}{-\mu_o \Delta z} \tag{A-6}$$

Based on the above equations, the derivative of the electric field at the time nΔt can be expressed as a central difference using electric field values at times (n+1/2) Δt and (n-1/2) Δt. Also, the derivative of the magnetic field at point kΔx can be determined as a central difference using magnetic field values at points (k+1/2) Δx and (k-1/2) Δx. This algorithm which is referred to as the leap-frog scheme will calculate all the magnetic fields first and then all the electric field values are calculated. E and H fields are shifted in space by half of the space discretization (Δx).

The explicit equations directly used by FDTD can be derived from equations A-5 and A-6:

$$E_x^{n+\frac{1}{2}}(k) = E_x^{n-\frac{1}{2}}(k) + \frac{\Delta t}{\Delta z\sqrt{\mu_o \varepsilon_o}}\left(H_y^n\left(k-\frac{1}{2}\right) - H_y^n\left(k+\frac{1}{2}\right)\right) \quad \text{(A-7)}$$

$$H_y^{n+1}(k+\frac{1}{2}) = H_y^n(k+\frac{1}{2}) + \frac{\Delta t}{\Delta z\sqrt{\mu_o \varepsilon_o}}(E_x^{n+\frac{1}{2}}(k) - E_x^{n+\frac{1}{2}}(k+1)) \quad \text{(A-8)}$$

This means that during the calculations, E and H values are offset by half a cell and half a time step. Based on these equations, any FDTD program can go through the following procedure for fields calculations:

1) Determine the size of the domain for which calculation is needed.
2) Define the time step and spatial resolution necessary for calculations
3) Perform a cycle to calculate fields for a certain number of time steps. This cycle computes various E-field values according to equation A-7 for all cells of the domain based on the excitation signal at the source location. H-field values will be computed based on equation A-8.

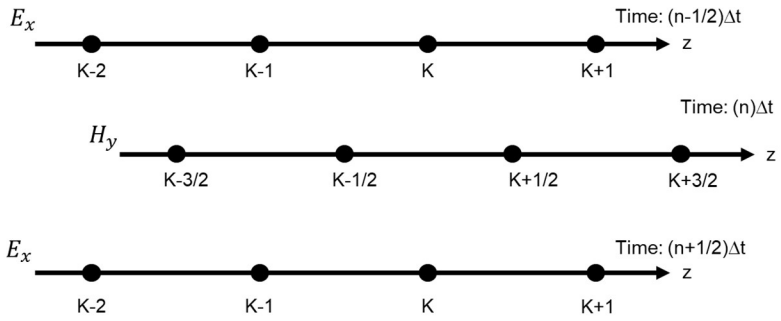

Figure A-1: The schematic of a one-dimensional FDTD scheme for updating EM fields in space and time

It can be shown that FDTD can approximate the solution to many of the electromagnetic problems with a high degree of accuracy. For example, figure A-2 shows the transmission (T) and reflection (R) from the three layer stack of dielectric materials (a dielectric material with refractive index of 2.5 sandwiched between two layers with the index of 1.5, with all layers having the thickness of 2.5 μm) as a function of incident light angle for the wavelength of 1 μm calculated by both FDTD and transfer matrix methods. The results reveal a very close agreement between the two approaches.

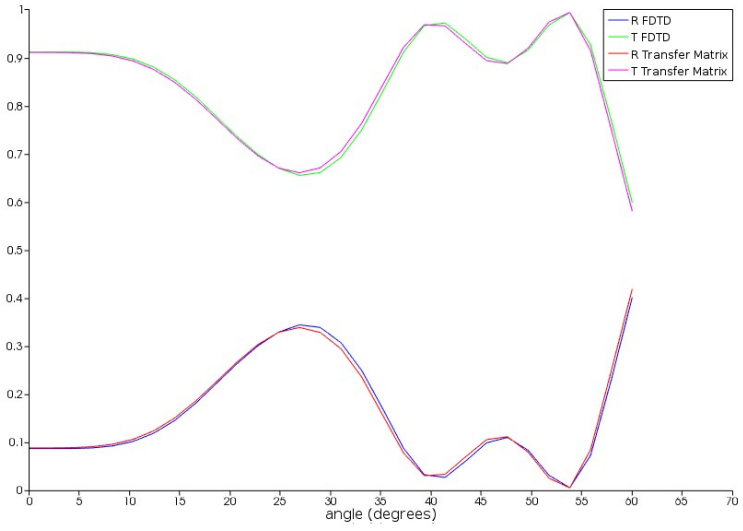

Figure A-2: Transmission (T) and reflection (R) from the three layer stack of dielectric materials as a function of incident light angle calculated by both FDTD and transfer matrix methods

Appendix B

Summary of input data for simulations

B.1. Optical constants of the materials

Table B-1: References of the optical constants for materials used for simulations

	PbS	ZnO/TiO_2	Au	ITO	Glass	PS	PDMS
Optical Constants (n,k)	Fig. B-1	[84]	[85]	[86]	[85]	[130]	[129]

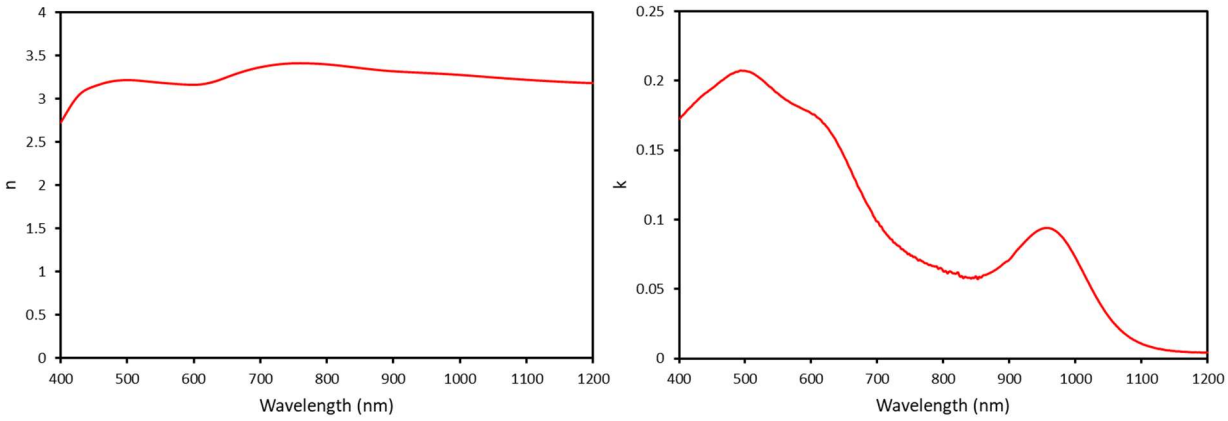

Figure B-1: Plot of the optical constants of PbS quantum dots used for simulations

B.2. Electrical simulation parameters

Table B-2: Summary of the parameters used for electrical simulations and their references

	PbS	ZnO/TiO_2	Au	ITO
Work Function (eV)	4.6 [35]	5.7 [35]	5.1[147]	4.4 [148]
Thickness (nm)	300	150	100	200
E_g (eV)	1.3 [35]	3.2 [35]	-	-
$\mu_{e,h}$ ($cm^2/V.s$)	0.01 [35]	0.05 [35]	-	-
$\tau_{e,h}$ (s)	$1e^{-7}$ [35]	$1e^{-5}$ [149]	-	-
Doping (cm^{-3})	$1e^{16}$ [35]	$1e^{18}$ [35]	-	-
ε_r	20 [150]	85 [151]	-	-
m^*_e/m_0	0.2 [152]	0.943 [153]	-	-

m^*_h/m_o	0.27 [152]	1.805 [153]	-	-

B.3. MATLAB codes for transfer matrix simulations

```
% Copyright 2010 George F. Burkhard, Eric T. Hoke, Stanford University
%     This program is free software: you can redistribute it and/or modify
%     it under the terms of the GNU General Public License as published by
%     the Free Software Foundation, either version 3 of the License, or
%     (at your option) any later version.
%
%     This program is distributed in the hope that it will be useful,
%     but WITHOUT ANY WARRANTY; without even the implied warranty of
%     MERCHANTABILITY or FITNESS FOR A PARTICULAR PURPOSE.  See the
%     GNU General Public License for more details.
%
%     You should have received a copy of the GNU General Public License
%     along with this program.  If not, see <http://www.gnu.org/licenses/>.
% This program calculates the field profile, exciton generation profile
% and generated current from the wavelength dependent complex indicies of
% refraction in devices using the transfer matrix method. It assumes the light source
% light source is in an n=1 environment (air) and that the first layer is
% a thick superstrate, so that incoherent reflection from the air/1st layer
% interface is taken into account before the coherent interference is
% calculated in the remaining layers. If there is no thick superstrate,
% input 'Air' as the first layer so that the incoherent reflection calculates
% to 0.
% The program
% also returns the calculated short circuit current for the device in
% mA/cm^2 if the device had an IQE of 100%.
% The procedure was adapted from J. Appl. Phys Vol 86, No. 1 (1999) p.487
% and JAP 93 No. 7 p. 3693.
% George Burkhard and Eric Hoke February 5, 2010
% When citing this work, please refer to:
%
% G. F. Burkhard, E. T. Hoke, M. D. McGehee, Adv. Mater., 22, 3293.
% Accounting for Interference, Scattering, and Electrode Absorption to Make
% Accurate Internal Quantum Efficiency Measurements in Organic and Other
% Thin Solar Cells
% Modifications:
% 3/3/11 Parastic absorption (parasitic_abs) is calculated and made
% accessable outside of script.
% 3/5/15 Improved precision of fundamental constants
function TransferMatrix
%------------BEGIN USER INPUT PARAMETERS SPECITIFCATION---------------
%
lambda=400:1200; % Wavelengths over which field patterns are calculated
stepsize = 1;   % The electric field is calculated at a latice of points (nm)
                % in the device cross section seperated by this distance
xx=230;%Generation profile width (nm)
zz=50;  %Generation profile width (nm)  minimum 3 nm
% plotWavelengths specifies which wavelengths to plot when plotting E-field
% intensity distributions (figure 1). Specify values by adding wavelength
% values to the array. Values must be within the range of calculated
% wavelenths (ie. must be an element of the lambda array). All wavelengths
% are in nanometers.
plotWavelengths = [400 800 1200];
% Specify Layers in device (an arbitrary number of layers is permitted) and
% thicknesses.
%
% Change these arrays to change the order or number of layers and/or
% thickness of layers. List the layers in the order that they appear in the
% device starting with the side the light is incident on.  THE NAMES OF THE
% LAYERS MUST CORRESPOND TO THE NAMES OF THE MATERIALS IN THE INDEX OF
```

```
% REFRACTION LIBRARY FILE, 'Index_of_Refraction_library.xls'. The first
% layer must be the transparent substrate (glass) or 'Air' if the active
% layers are on the reflective electrode (rather than transparent electrode) side
% of the device.  The layer thicknesses are in nanometers.
layers = {'glass' 'ITO' 'ZnO' 'PbS' 'Au'}; % Names of layers of materials starting from side
light is incident from
thicknesses = [0 200 150 300 100];  % thickness of each corresponding layer in nm (thickness of
the first layer is irrelivant)
% Set plotGeneration to 'true' if you want to plot generation rate as a
% function of position in the device and output the calculated short circuit current
% under AM1.5G illumination (assuming 100% internal quantum efficiency)
plotGeneration = true;
activeLayer = 4; % index of material layer where photocurrent is generated
%
%------------END USER INPUT PARAMETERS SPECIFICATION-------------------
% Load in index of refraction for each material
n = zeros(size(layers,2),size(lambda,2));
for index = 1:size(layers,2)
    n(index,:) = LoadRefrIndex(layers{index},lambda);
end
t = thicknesses;
% Constants
h = 6.62606957e-34;     % Js Planck's constant
c = 2.99792458e8;   % m/s speed of light
q = 1.60217657e-19; % C electric charge
% Calculate Incoherent power transmission through substrate
% See Griffiths "Intro to Electrodynamics 3rd Ed. Eq. 9.86 & 9.87
T_glass=abs(4*1*n(1,:)./(1+n(1,:)).^2);
R_glass=abs((1-n(1,:))./(1+n(1,:))).^2;
% Calculate transfer matrices, and field at each wavelength and position
t(1)=0;
t_cumsum=cumsum(t);
x_pos=(stepsize/2):stepsize:sum(t); %positions to evaluate field
%x_mat specifies what layer number the corresponding point in x_pos is in:
x_mat= sum(repmat(x_pos,length(t),1)>repmat(t_cumsum',1,length(x_pos)),1)+1;
R=lambda*0;
E=zeros(length(x_pos),length(lambda));
for l = 1:length(lambda)
    % Calculate transfer matrices for incoherent reflection and transmission at the first
interface
    S=I_mat(n(1,l),n(2,l));
    for matindex=2:(length(t)-1)
        S=S*L_mat(n(matindex,l),t(matindex),lambda(l))*I_mat(n(matindex,l),n(matindex+1,l));
    end
    R(l)=abs(S(2,1)/S(1,1))^2; %JAP Vol 86 p.487 Eq 9 Power Reflection from layers other than
substrate
    T(l)=abs(2/(1+n(1,l)))/sqrt(1-R_glass(l)*R(l)); %Transmission of field through glass
substrate Griffiths 9.85 + multiple reflection geometric series
    % Calculate all other transfer matrices
    for material = 2:length(t)
        xi=2*pi*n(material,l)/lambda(l);
        dj=t(material);
        x_indices=find(x_mat == material); %indices of points which are in the material layer
considered
        x=x_pos(x_indices)-t_cumsum(material-1); %distance from interface with previous layer
        % Calculate S matrices (JAP Vol 86 p.487 Eq 12 and 13)
        S_prime=I_mat(n(1,l),n(2,l));
        for matindex=3:material
            S_prime=S_prime*L_mat(n(matindex-1,l),t(matindex-1),lambda(l))*I_mat(n(matindex-
1,l),n(matindex,l));
        end
        S_doubleprime=eye(2);
        for matindex=material:(length(t)-1)

S_doubleprime=S_doubleprime*I_mat(n(matindex,l),n(matindex+1,l))*L_mat(n(matindex+1,l),t(matindex
+1),lambda(l));
        end
        % Normalized Field profile (JAP Vol 86 p.487 Eq 22)
```

```
        E(x_indices,l)=T(l)*(S_doubleprime(1,1)*exp(-1i*xi*(dj-
x))+S_doubleprime(2,1)*exp(1i*xi*(dj-x))) ./(S_prime(1,1)*S_doubleprime(1,1)*exp(-
1i*xi*dj)+S_prime(1,2)*S_doubleprime(2,1)*exp(1i*xi*dj));
    end
end
% Overall Reflection from device with incoherent reflections at first
% interface (typically air-glass)
Reflection=R_glass+T_glass.^2.*R./(1-R_glass.*R);
% Plots electric field intensity |E|^2 vs position in device for
% wavelengths specified in the initial array, plotWavelengths.
close all
figure(1)
plotString = '';
legendString = cell(1,size(plotWavelengths,2));
for index=1:size(plotWavelengths,2)
    plotString = strcat(plotString, ['x_pos,abs(E(:,', num2str(find(lambda ==
plotWavelengths(index))), ').^2),']);
    legendString{index} = [num2str(plotWavelengths(index)), ' nm'];
end
eval(['plot(', plotString, '''LineWidth'',2)'])
axislimit1=axis;
% Draws vertical lines at each material boundary in the stack and labels
% each layer
for matindex=2:length(t)
    line([sum(t(1:matindex)) sum(t(1:matindex))],[0 axislimit1(4)]);
    text((t_cumsum(matindex)+t_cumsum(matindex-
1))/2,0,layers{matindex},'HorizontalAlignment','center','VerticalAlignment','bottom')
end
title('E-field instensity in device');
xlabel('Position in Device (nm)');
ylabel('Normalized Electric field intensity |E|^2');
legend(legendString);
% Absorption coefficient in cm^-1 (JAP Vol 86 p.487 Eq 23)
a=zeros(length(t),length(lambda));
for matindex=2:length(t)
     a(matindex,:)=4*pi*imag(n(matindex,:))./(lambda*1e-7);
end
% Plots normalized intensity absorbed /cm3-nm at each position and
% wavelength as well as the total reflection expected from the device
% (useful for comparing with experimentally measured reflection spectrum)
figure(2)
Absorption=zeros(length(t),length(lambda));
plotString = '';
for matindex=2:length(t)
    Pos=find(x_mat == matindex);
    AbsRate=repmat(a(matindex,:).*real(n(matindex,:)),length(Pos),1).*(abs(E(Pos,:)).^2);
    Absorption(matindex,:)=sum(AbsRate,1)*stepsize*1e-7;
    plotString = strcat(plotString, ['lambda,Absorption(', num2str(matindex), ',:),']);
end
eval(['plot(', plotString, 'lambda,Reflection,''LineWidth'',2)'])
title('Fraction of Light absorbed or reflected');
xlabel('Wavelength (nm)');
ylabel('Light Intensity Fraction');
legend(layers{2:size(layers,2)}, 'Reflectance');
% Plots generation rate as a function of position in the device and
% calculates Jsc
if plotGeneration == true
    % Load in 1sun AM 1.5 solar spectrum in mW/cm2nm
    AM15_data=xlsread('AM15.xls');
    AM15=interp1(AM15_data(:,1), AM15_data(:,2), lambda, 'linear', 'extrap');
    figure(3)
    % Energy dissipation mW/cm3-nm at each position and wavelength (JAP Vol
    % 86 p.487 Eq 22)
    ActivePos=find(x_mat == activeLayer);

Q=repmat(a(activeLayer,:).*real(n(activeLayer,:)).*AM15,length(ActivePos),1).*(abs(E(ActivePos,:)
).^2);
    % Exciton generation rate per second-cm3-nm at each position and wavelength
    Gxl=(Q*1e-3).*repmat(lambda*1e-9,length(ActivePos),1)/(h*c);
    if length(lambda)==1
```

```
        lambdastep= 1;
    else
        lambdastep=(max(lambda)-min(lambda))/(length(lambda)-1);
    end
    Gx=sum(Gxl,2)*lambdastep; % Exciton generation rate as a function of position/(sec-cm^3)
    Gx=flipud(Gx);
    plot(x_pos(ActivePos),flipud(Gx),'LineWidth',2)
    axislimit3=axis;
    axis([axislimit1(1:2) axislimit3(3:4)])
    % inserts vertical lines at material boundaries
    for matindex=2:length(t)
        line([sum(t(1:matindex)) sum(t(1:matindex))],[0 axislimit3(4)]);
        text((t_cumsum(matindex)+t_cumsum(matindex-
1))/2,0,layers{matindex},'HorizontalAlignment','center','VerticalAlignment','bottom')
    end
    title('Generation Rate in Device')
    xlabel('Position in Device (nm)');
    ylabel('Generation rate /(sec-cm^3)');
    % outputs predicted Jsc under AM1.5 illumination assuming 100% internal
    % quantum efficiency at all wavelengths
    Jsc=sum(Gx)*stepsize*1e-7*q*1e3 %in mA/cm^2
    % Calculate parasitic absorption
    parasitic_abs=(1-Reflection-Absorption(activeLayer,:))';
    % sends absorption, reflection, and wavelength data to the workspace
    assignin('base','absorption',Absorption');
    assignin('base','reflection',Reflection');
    assignin('base','parasitic_abs',parasitic_abs);
    assignin('base','lambda',lambda');
    G=zeros(xx,thicknesses(activeLayer)/stepsize,zz);
    for inx=1:xx
        for inx1=1:zz
        G(inx,:,inx1)=Gx(:,1);
        end
    end
    assignin('base','G',G);
    assignin('base','Gx',Gx);
    x=1:1:xx;
    y=1:1:(thicknesses(activeLayer)/stepsize);
    z=1:1:zz;
    x=((x.')-(xx/2)).*(10^(-9));
    y=((y.')-((thicknesses(activeLayer)/stepsize)/2)).*(10^(-9));
    z=((z.')-(zz/2)).*(10^(-9));
    G=G.*(10^6); % save G in 1/sec-m^3 for Lumerical DEVICE
    save('Gen.mat','x','y','z','G')
end
%------------------- Helper Functions -----------------------------------
% Function I_mat
% This function calculates the transfer matrix, I, for reflection and
% transmission at an interface between materials with complex dielectric
% constant n1 and n2.
function I = I_mat(n1,n2)
r=(n1-n2)/(n1+n2);
t=2*n1/(n1+n2);
I=[1 r; r 1]/t;
% Function L_mat
% This function calculates the propagation matrix, L, through a material of
% complex dielectric constant n and thickness d for the wavelength lambda.
function L = L_mat(n,d,lambda)
xi=2*pi*n/lambda;
L=[exp(-1i*xi*d) 0; 0 exp(1i*xi*d)];
% Function LoadRefrIndex
% This function returns the complex index of refraction spectra, ntotal, for the
% material called 'name' for each wavelength value in the wavelength vector
% 'wavelengths'.  The material must be present in the index of refraction
% library 'Index_of_Refraction_library.xls'.  The program uses linear
% interpolation/extrapolation to determine the index of refraction for
% wavelengths not listed in the library.
function ntotal = LoadRefrIndex(name,wavelengths)
%Data in IndRefr, Column names in IndRefr_names
[IndRefr,IndRefr_names]=xlsread('Index_of_Refraction_library.xls');
```

```
% Load index of refraction data in spread sheet, will crash if misspelled
file_wavelengths=IndRefr(:,strmatch('Wavelength',IndRefr_names));
n=IndRefr(:,strmatch(strcat(name,'_n'),IndRefr_names));
k=IndRefr(:,strmatch(strcat(name,'_k'),IndRefr_names));
% Interpolate/Extrapolate data linearly to desired wavelengths
n_interp=interp1(file_wavelengths, n, wavelengths, 'linear', 'extrap');
k_interp=interp1(file_wavelengths, k, wavelengths, 'linear', 'extrap');
%Return interpolated complex index of refraction data
ntotal = n_interp+1i*k_interp;
```